2-27-2024

# On the use of gauge functions to obtain convergent power series solutions to nonlinear ODEs

Nastaran Naghshineh
nxncad@rit.edu

# On the use of gauge functions to obtain convergent power series solutions to nonlinear ODEs

by

Nastaran Naghshineh

A Dissertation Submitted in Partial Fulfillment of the Requirements

for a PhD Degree in Mathematical Modeling

School of Mathematics and Statistics, College of Science

Rochester Institute of Technology

Rochester, New York

February 27, 2024

# Committee Approval:

R·I·T
College of
SCIENCE

---

Steven J. Weinstein, PhD Date

Kate Gleason College of Engineering

School of Mathematics and Statistics

Thesis Advisor

---

Mohamed A. Samaha, PhD Date

RIT-Dubai, Dept. of Mechanical and Industrial Engineering

School of Mathematics and Statistics

Thesis Co-Advisor

---

Nathaniel S. Barlow, PhD Date

School of Mathematics and Statistics

Committee Member

Kathleen Lamkin-Kennard, PhD Date

Kate Gleason College of Engineering

Committee Chair

David A. Kofke, PhD Date

University at Buffalo, School of Engineering and Applied Sciences

Committee Member

Nathan Cahill, D.Phil. Date

School of Mathematics and Statistics

Director of Mathematical Modeling Program

# Dedication

*This dissertation is dedicated to the loves of my life, Majid, and to our son, Yousuf Liam, who I cannot wait to hold in my arms in a few months.*

# Acknowledgement

First and foremost, I would like to thank my primary advisor, Dr. Steven Weinstein, for his commitment, flexibility, patience, guidance, understanding, and support. Steve has helped me through all the challenges I faced during my PhD journey. With his support, I have grown academically, professionally, and personally in all aspects of my life. Thanks very much for believing in me, seeing my potential, and always encouraging me to move forward, Steve! You are indeed my true inspiration and source of confidence. Thank you for teaching me how to pursue my goals patiently! I could not be who I am today–professionally and personally–without your support. I would also like to thank my co-advisor in Dubai, Dr. Mohamed Samaha, for his support and guidance throughout my PhD dissertation.

My committee member, Dr. Nathaniel Barlow, has been much more than a committee member! He has guided me through every single step of complicated mathematics, analysis of my dissertation, and in publishing my papers. Thank you for your advice and guidance, and for always answering my questions with patience and care, Nate! Additionally, I would like to thank my other committee members, Dr. David Kofke and Dr. Kathleen Lamkin-Kennard, for the time they spent reading my thesis and for their valuable feedback. Further thanks go to Dr. Kofke for providing an internship opportunity, where I was exposed to a new and exciting field of mathematics.

I also thank members of School of Mathematics and Statistics for providing guidance and administrative support during my PhD dissertation. Special thanks go to the PhD Program Director of Mathematical Modeling, Dr. Nathan Cahill, and the Mathematical Modeling Program Assistant, Kathleen Koch.

I am forever grateful to my husband, Majid, for sharing every single step of my PhD journey by giving me his unconditional love and encouragement, for working extra hard to ensure I have

peace of mind. Thank you, Majid, for giving me the courage to begin this long and challenging journey! I am the happiest with you!

Last but not least, I would like to thank my parents, Jalal and Fatemeh, and my siblings, Mohammad and Negin, for their love, support, and help throughout the years.

## Abstract

*This dissertation examines the power series solutions—and their analytic continuation via gauge transformations—of three classical nonlinear ordinary differential equations arising in fluid mechanics that are mathematically related by their large-distance asymptotic behaviors in semi-infinite domains. The first problem examines the influence of surface tension and gravitational forces to form a static air–liquid interface that intersects a flat wall at a given contact angle and limits to a flat pool away from the wall. The second problem considers the related configuration of an axisymmetric air–liquid interface formed when the flat wall is replaced with a right circular cylinder. In both problems, we show that although power series solutions for the interface shapes are readily obtainable, the series diverge due to the influence of convergence-limiting singularities. In both cases, these singularities are mapped to new locations through transformations that are motivated by long-distance asymptotic behaviors of the solution. Convergent power series solutions to both problems are thus obtained. The third problem considers the Sakiadis boundary layer induced by a rapidly moving wall in a semi-infinite fluid domain, for which no exact analytic solution has been put forward in prior literature. For this problem, we follow the approach of the previous problems, and derive a convergent power series solution for both Newtonian and Ostwald-de Waele power law non-Newtonian fluids. Overall, this dissertation demonstrates that asymptotic behaviors, in conjunction with gauge function choices, can lead to exact convergent power series solutions to problems in mathematical physics.*

# Contents

# I. Introduction

The primary objective of the thesis is to examine and enhance the ability of power series solutions to solve nonlinear ordinary differential equations (ODEs). This work is motivated by a growing body of literature in which such methods have been used to solve problems in disparate areas of mathematical physics [1–7]. It is within this context that we study the convergent power series solutions to three classical nonlinear ODEs in fluid mechanics [1]. In the first problem, we consider a configuration where an air–liquid interface with surface tension rises above a static pool of liquid, referred to here as the "Flat Wall Problem". The second related problem is the "Cylindrical Wall Problem", where the shape of an axisymmetric interface is determined along a right cylindrical wall immersed in a static pool of liquid. In the final problem, we extend the previously studied flow field associated with the Sakiadis boundary layer for a Newtonian fluid (referred to here as the "Newtonian Sakiadis Problem") to Ostwald-de Waele power law fluids (referred to here as the "Non-Newtonian Sakiadis Problem").

In all the three problems, exact solutions are obtained for interface shapes and flow fields in the form of convergent power series solutions written to incorporate asymptotic behaviors and judiciously chosen gauge functions. In the current context, a gauge function is defined as follows. For a given function expressed as $f(x) = \sum_{n=0}^{\infty} a_n x^n$ where $a_n$ are constants, a gauge function, $g(x)$, is defined so that $f(x)$ may be rewritten as $f(x) = \sum_{n=0}^{\infty} A_n \left(g(x)\right)^n$. This is equivalent to the Taylor expansion of composite function $f(g(x))$ in powers of $g$, or equivalent to a variable transformation $u = g(x)$ where $f(u)$ is the resulting function. When a transformed series—such as that using a gauge function transformation—has a region of convergence, which extends beyond that of the

[1] These three problems have been completed in collaboration with W. Cade Reinberger, PhD student at RIT Mathematical Modeling program. Hence, portions of this document may appear in Reinberge's dissertation in the future.

original series, this is referred to as an analytic *continuation* of the original series [8].

In the Flat Wall Problem, the shape of a static meniscus forming along a flat wall in an infinite horizontal pool is well-studied [9, 10]. For this problem, there exists an exact solution—expressed as distance from the wall as function of interface height [9]. Here, we provide an alternative explicit solution as interface height vs. distance from the wall. The problem choice is judicious as the prior exact solution enables conclusions to be drawn efficiently—and these conclusions can be applied to the other problems considered in this thesis. We show that the asymptotic behaviour follows an exponential form and there exists a singularity whose effect limits convergence of the standard power series solution. An exponential variable transformation is used that effectively moves the singularity responsible for the radius of convergence, which is the distance between the expansion point and the closest singularity, further from the expansion point. This transformation allows for the new series to converge over the entire physical domain, and is thus an effective analytic continuation of the original series, whose region of convergence was restricted to only a portion of the physical domain. This work has been published in February 2023 by *IMA Journal of Applied Mathematics* [11].

In the Cylindrical Wall Problem, we examine the height of a static liquid interface that forms on the outside of a solid vertical cylinder in an unbounded stagnant pool exposed to air. Gravitational and surface tension forces form the interface shape as characterized by the Bond number. Here, we provide a convergent power series solution for interface shapes that rise above or fall below the horizontal pool as a function of contact angle and Bond number. We find that the power series solution expressed in terms of the radial distance from the wall is divergent, and thus rewrite the divergent series as a new power series expressed as powers of an Euler transformed variable (i.e., the Euler transform is a particular type of a gauge function described herein); this series is modified to match the large distance asymptotic behavior of the meniscus. The Euler transformation is a type of analytic continuation, as it maps non-physical singularities to locations

that do not restrict series convergence in the physical domain, while the asymptotic modification increases the rate of convergence of the series overall. We demonstrate that when the divergent series coefficients are used to implement the Euler transformation, finite precision errors are incurred, even for a relatively small number of terms. To avoid such errors, the independent variable in the governing differential equation is changed to that of the Euler transform, and the power series is developed directly without using the divergent series. The resulting power series solution is validated by comparison with a numerical solution of the interface shape and the matched asymptotic solution for the height of the interface along the cylinder developed by Lo [12] for small Bond numbers. The convergent power series expansion has the ability to exceed the accuracy of the matched asymptotic solution for any Bond number given enough terms, and the recursive nature of the solution makes it straightforward to implement. This work has been published in January 2024 by *IMA Journal of Applied Mathematics* [13].

The Non-Newtonian Sakiadis Problem is an important flow field in configurations where thin liquid films are coated onto moving substrates [14], and is an essential component of hydrodynamic assist in high speed curtain coating [15]. To date, the Newtonian Sakiadis Problem has been examined by our research group, and a conjectured exact analytical solution has been obtained [11]. In practice, however, many coated fluids are non-Newtonian, as they often contain dispersions and polymeric materials—these impart a flow dependence to viscosity, which incorporates the ability of the fluid to resist deformation. It is well known in the coating literature that such characteristics can have a drastic impact on the ability to coat thin liquid films uniformly [14]. In this thesis, we extend the approach used to solve the Newtonian Sakiadis Problem to obtain an analytical solution of the Sakiadis boundary layer for non-Newtonian Ostwald-de Waele power law fluids. Contrary to prior literature, the asymptotic behavior in this problem dictates that a solution only exists in a limited range of physical parameters, which is a direct consequence of mathematical limitations of the power law model itself. The utility of the power series solution is that it can

be solved on the entire semi-infinite domain and—in contrast to a numerical solution—does not require a finite domain length approximation and subsequent domain length refinement. This work has been published in April 2023 by *Physics of Fluids* [16].

This thesis is organized as follows. For each problem, we study the governing equation, boundary conditions, a divergent power series expansion about the wall location, an asymptotic expansion away from the wall, a convergent power series solution motivated by the asymptotic expansion, and comparison with the numerical solution and/or other existing solutions. The Flat Wall Problem is considered in Chapter II, the Cylindrical Wall Problem in Chapter III, and the Non-Newtonian Sakiadis Problem in Chapter IV. We provide some overarching conclusions drawn from the three problems considered in Chapter V. In Appendix A, formulas used to manipulate nonlinear series are provided. Appendix B provides details related to the Cylindrical Wall Problem; this includes formulas related to Euler transformation, a small interface slope asymptotic solution, and the first and second order matched asymptotic solutions developed by Lo [12]. Appendix C provides details related to the Non-Newtonian Sakiadis Problem; this includes the shooting algorithm used to solve the problem numerically (used to compare with the power series solution), relevant numerically determined constants used to generate the solution, and the algorithm used to predict the same constants via the convergent power series solution itself.

# II. The meniscus formed on a flat wall

Portions of this chapter are taken directly from a manuscript published in *IMA Journal of Applied Mathematics* [11]. Some notation and verbiage have been changed to enhance the readability of the thesis document as a whole.

## II.1 Problem statement and formulation

We examine the well-studied problem of the shape of a static meniscus rising above an infinite horizontal pool [9, 10], referred to henceforth as the Flat Wall Problem. The pool of liquid with density, $\rho$, is subjected to gravity, $g$, and is in contact with air of negligible density. A flat wall is placed vertically in the pool, and the liquid intersects the wall with a contact angle $\theta$ (measured through the liquid) as shown in Figure 5b; for purposes of this study, we assume that $\theta$ lies between 0 and $\pi/2$. The location of the air–liquid interface, with surface tension $\sigma$, is parameterized as $y = h(x)$ where $x$ is the horizontal distance from the wall, and $y = 0$ is the undisturbed location of the interface as $x \to \infty$. For this configuration, the Young–Laplace equation couples with the hydrostatic field to yield the following dimensionless equation and boundary conditions [9, 10]:

$$\bar{h} = \frac{\frac{d^2\bar{h}}{d\bar{x}^2}}{\left[1 + \left(\frac{d\bar{h}}{d\bar{x}}\right)^2\right]^{3/2}}, \tag{II.1a}$$

$$\frac{d\bar{h}}{d\bar{x}} = -\cot\theta, \text{ at } \bar{x} = 0, \tag{II.1b}$$

$$\bar{h} \to 0, \text{ as } \bar{x} \to \infty. \tag{II.1c}$$

In the rest of the analysis, we switch notation where primes denote the derivatives of $\bar{h}$ with respect to $\bar{x}$, and the over-bars denote dimensionless variables defined as

$$\bar{h} = \frac{h}{\mathcal{L}} \quad , \quad \bar{x} = \frac{x}{\mathcal{L}} \quad , \quad \mathcal{L} = \sqrt{\frac{\sigma}{\rho g}}. \tag{II.2}$$

In (II.2), the characteristic length scale $\mathcal{L}$ is the well-known capillary length. Multiplying both sides of (II.1a) by $\bar{h}'$, integrating, and applying the boundary conditions (II.1b) and (II.1c), we obtain

$$\bar{h}' = -\left[\frac{1}{\left(1-\frac{1}{2}\bar{h}^2\right)^2} - 1\right]^{1/2} , \tag{II.3a}$$

with the constraint

$$\bar{h} = \sqrt{2(1-\sin\theta)} \ , \ \text{at } \bar{x} = 0, \tag{II.3b}$$

where (II.3b) represents the height of the interface at the wall as function of the contact angle, $\theta \in [0, \pi/2]$. Note that (II.3b) is obtained by substituting the slope boundary condition (II.1b) into the ODE (II.3a) at $\bar{x} = 0$. Moreover, note that, in (II.3a), $\bar{h}' \to -\infty$ as $\bar{h} \to \sqrt{2}$.

The exact inverse solution $\bar{x}(\bar{h})$ of (II.3) is obtainable via variable separation and integration [9] and is given as

$$\bar{x} = \cosh^{-1}\frac{2}{\bar{h}} - \cosh^{-1}\sqrt{\frac{2}{1-\sin\theta}} + \sqrt{2+2\sin\theta} - \sqrt{4-\bar{h}^2} \ . \tag{II.4}$$

In what follows, we obtain an analytic solution for $\bar{h}(\bar{x})$ directly via series expansion. As motivated in our introductory Chapter I, our intention in doing so is not to replace the solution (II.4) in usage; rather is to examine how the choice of a gauge function affects series convergence. This will also enable us to obtain a power series solution to the more complex Non-Newtonian Sakiadis Problem in Chapter IV. The exact solution (II.4) is used in what follows to assess the accuracy of the series solutions provided in Sections II.2 and II.3.

## II.2 A divergent power series solution

The standard power series solution of (II.3) is found by assuming

$$\bar{h} = \sum_{n=0}^{\infty} a_n \bar{x}^n \quad , \quad |\bar{x}| < |\bar{x}_s(\theta)| \ , \tag{II.5a}$$

which is readily differentiated term-by-term to compute $h'$. Substituting (II.5a) into (II.3), using Cauchy's product rule [17] (see Appendix A.2) to evaluate $\bar{h}^2$, and applying JCP Miller's for-

mula [18] (see Appendix A.1) for raising a series to a power, we obtain the following recursions for the coefficients:

$$a_{n+1} = \frac{-2}{n+1} d_n, \quad n \geq 0, \tag{II.5b}$$

$$d_{n>0} = \frac{1}{n\widetilde{c}_0} \sum_{j=1}^{n} \left( \frac{3}{2} j - n \right) \widetilde{c}_j d_{n-j} \ , \ d_0 = \widetilde{c}_0^{\frac{1}{2}}, \tag{II.5c}$$

$$\widetilde{c}_{n>0} = c_{n>0} \ , \ \widetilde{c}_0 = c_0 - \frac{1}{4} \ , \ c_{n>0} = \frac{1}{n\widetilde{b}_0} \sum_{j=1}^{n} (-j-n) \widetilde{b}_j c_{n-j} \ , \ c_0 = (\widetilde{b}_0)^{-2}, \tag{II.5d}$$

$$\widetilde{b}_{n>0} = b_{n>0} \ , \ \widetilde{b}_0 = b_0 - 2 \ , \ b_n = \sum_{j=0}^{n} a_j a_{n-j}, \tag{II.5e}$$

with

$$a_0 = \sqrt{2(1-\sin\theta)}. \tag{II.5f}$$

In (II.5a), the series is stated to converge within the region $|\bar{x}| < |\bar{x}_s(\theta)|$ with $\bar{x}_s(\theta)$ being the as-of-yet undetermined closest singularity to $\bar{x} = 0$. Here, we conjecture that $\bar{x}_s(\theta)$ is the value that satisfies $\bar{h}(\bar{x}_s) = \sqrt{2}$ for a given $\theta$ in the exact solution (II.4), causing $\bar{h}' \to -\infty$ in (II.3a). Thus, $\bar{x}_s(\theta)$ is known exactly in closed-form from the substitution of $\bar{h} = \sqrt{2}$ into (II.4) as

$$\bar{x}_s(\theta) = \cosh^{-1}\sqrt{2} - \cosh^{-1}\sqrt{\frac{2}{1-\sin\theta}} + \sqrt{2+2\sin\theta} - \sqrt{2}\,, \tag{II.6}$$

where we note that $\bar{x}_s \leq 0$ for $\theta \in [0, \pi/2]$ and, in fact, $\bar{x}_s = 0$ when $\theta = 0$ (setting the radius of convergence to be 0). We support the conjecture that $\bar{x}_s$ is the closest singularity to $\bar{x} = 0$ (for all $\theta$) in what follows.

Figure 1 shows $N$-term truncations of series (II.5) (dashed curves), compared with the exact solution (II.4) (•'s) for $\theta = \pi/4$. The series (II.5) and numerical results agree for small $\bar{x}$ but ultimately diverge at a finite radius of convergence (indicated by a solid vertical line in the figure) and given by $|\bar{x}_s(\pi/4)| \approx 0.30$ from (II.6). Figure 2 provides a numerical implementation of the ratio test in the form of a Domb Sykes plot [19], where it is seen that the radius of convergence approaches 0.30 as $n \to \infty$ ($1/n \to 0$ in the figure), in agreement with (II.6) for $\theta = \pi/4$. Although

only shown in this section for $\theta = \pi/4$, all permissible $\theta$ values lead to similarly divergent series, limited by a radius of convergence of $|\bar{x}_s(\theta)|$, calculated in accordance with (II.6)—this confirms the conjecture stated above. In Section II.3, we utilize a gauge function transformation to overcome this convergence barrier for all contact angles.

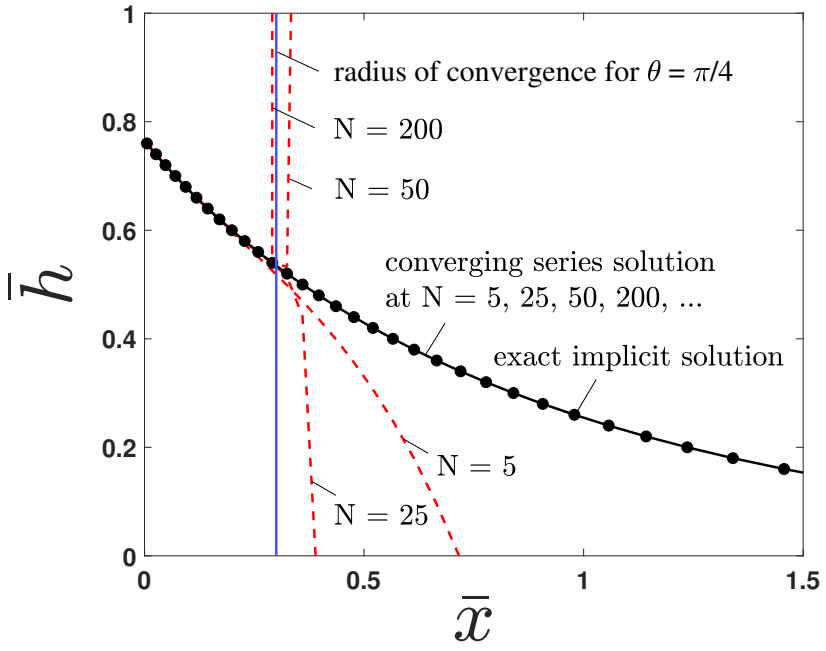


**Figure 1:** The solution to (II.3) is shown for a contact angle of $\theta = \pi/4$. The $N$-term truncations of the divergent series (II.5) (dashed curves) and the convergent resummation (II.15) (solid curves) are compared against the exact solution (II.4) (•'s). The solid vertical line shows the radius of convergence, $|\bar{x}_s(\pi/4)| \approx 0.30$, computed from (II.6).

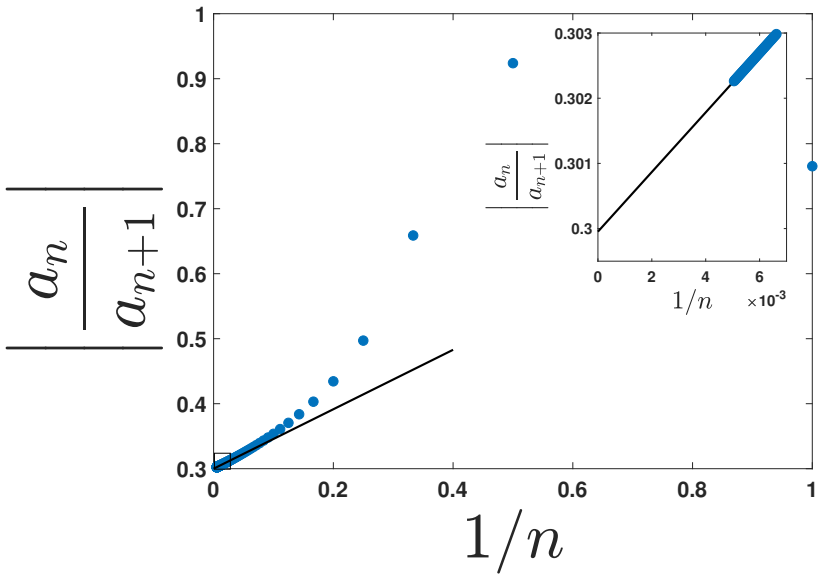


**Figure 2:** Domb-Sykes plot for (II.5) with $\theta = \pi/4$, indicating (via the numerical ratio-test) a radius of convergence of $|\bar{x}_s(\pi/4)| \approx 0.30$, which is consistent with what is observed in figure 1.

## II.3 A convergent power series solution

Despite its divergence beyond some positive $\bar{x}$-value, the power series solution (II.5) does provide the correct interface shape close to the wall. To overcome this divergence, we first examine the behavior of the solution away from the wall to deduce its behavior. To this end, the method of dominant balance [20] is employed. To meet the constraint (II.1c), it is assumed that

$$\bar{h}(\bar{x}) \ll 1, \tag{II.7a}$$

and this also assures that its derivatives are small in the limit. To lowest order, then, the governing equation (II.1a) is approximated as:

$$\bar{h}'' \sim \bar{h} \text{ as } \bar{x} \to \infty. \tag{II.7b}$$

The asymptotic solution to (II.7b) is

$$\bar{h} \sim C_0 e^{-\bar{x}} \text{ as } \bar{x} \to \infty, \tag{II.7c}$$

where $C_0$ is an arbitrary constant. To obtain the next correction, we assume the following expansion

$$\bar{h} \sim C_0 e^{-\bar{x}} + D(\bar{x}) \text{ as } \bar{x} \to \infty, \tag{II.7d}$$

where

$$D(\bar{x}) \ll C_0 e^{-\bar{x}} \text{ as } \bar{x} \to \infty. \tag{II.7e}$$

Equation (II.7d) is substituted into (II.1a), subdominant terms are neglected, and the resulting linear equation is solved in accordance with the asymptotic relation (II.7e) to obtain:

$$D(\bar{x}) \sim \frac{3}{16} C_0^3 e^{-3\bar{x}} \text{ as } \bar{x} \to \infty. \tag{II.7f}$$

The same process is repeated to generate higher order correction to (II.7d). We obtain:

$$\bar{h} \sim C_0 e^{-\bar{x}} + \frac{3}{16} C_0^3 e^{-3\bar{x}} + \frac{25}{256} C_0^5 e^{-5\bar{x}} + O(e^{-7x}) \text{ as } \bar{x} \to \infty. \tag{II.8}$$

The pattern of exponentials is thus evident in equation (II.8).

The asymptotic solution (II.8) motivates us to transform (II.3) to reflect the exponential pattern of (II.8). This is achieved by transformations in both the independent and dependent variables, given respectively as

$$U(\bar{x}) = e^{-2\bar{x}}, \tag{II.9a}$$

$$H\left(U(\bar{x})\right) = \bar{h}(\bar{x}) e^{\bar{x}}. \tag{II.9b}$$

Substituting (II.9) into (II.3) leads to the transformed ODE:

$$\left[H + 2UH'\right]\left[UH^2 - 2\right] = -H\sqrt{4 - UH^2}\,, \tag{II.10}$$

with transformed boundary condition

$$H(1) = \sqrt{2(1 - \sin\theta)}\,, \tag{II.11}$$

where $H'$ denotes the derivative with respect to $U$. Although an exact explicit solution to (II.10) cannot be found as $H(U)$, an exact implicit solution in $H$ and $U$ can be found by separating variables, integrating (II.10), and applying (II.11) to arrive at

$$\sqrt{2+2\sin\theta} - \sqrt{4-UH^2} = \ln \frac{H\left[1+\sqrt{1+\sin\theta}\right]}{\sqrt{1-\sin\theta}\left[2+\sqrt{4-UH^2}\right]} \ . \tag{II.12}$$

Equation (II.12) is used to extract the condition

$$H(0) = \frac{4\sqrt{1-\sin\theta}\ e^{-2+\sqrt{2+2\sin\theta}}}{\sqrt{1+\sin\theta}+\sqrt{2}} \ , \tag{II.13}$$

which implies $H(0) = C_0$ in the asymptotic solution (II.8). This is needed for the series solution that follows.

Using the same procedure as in Section II.2 (using Cauchy's product rule [17] and JCP Miller's formula [18], provided in Appendixes A.2 and A.1, respectively), the power series solution of (II.10) (with condition (II.13)) is given by

$$H = \sum_{n=0}^{\infty} A_n U^n, \tag{II.14}$$

where,

$$A_{n>0} = \frac{-\sum_{j=0}^{n-1} A_j[(1+2j)\mathcal{C}_{n-j} + \mathcal{D}_{n-j}]}{\mathcal{D}_0 + \mathcal{C}_0(1+2n)} \ , \tag{II.15a}$$

$$\mathcal{D}_{n>0} = \frac{1}{n\widetilde{\mathcal{B}}_0}\sum_{j=1}^{n}(\frac{3}{2}j-n)\widetilde{\mathcal{B}}_j\mathcal{D}_{n-j} \ \ , \ \ \mathcal{D}_0 = \widetilde{\mathcal{B}}_0^{\frac{1}{2}} \ \ , \ \ \mathcal{C}_{n>0} = \mathcal{B}_{n-1} \ \ , \ \ \mathcal{C}_0 = -2 \ , \tag{II.15b}$$

$$\widetilde{\mathcal{B}}_{n>0} = -\mathcal{B}_{n-1} \ \ , \ \ \widetilde{\mathcal{B}}_0 = 4 \ \ , \ \ \mathcal{B}_n = \sum_{j=0}^{n} A_j A_{n-j} \ , \tag{II.15c}$$

with

$$A_0 = \frac{4\sqrt{1-\sin\theta}\ e^{-2+\sqrt{2+2\sin\theta}}}{\sqrt{1+\sin\theta}+\sqrt{2}} \ . \tag{II.15d}$$

Transforming back to $\bar{h}(\bar{x})$ space via (II.9), our expansion about $\bar{x} = \infty$ (i.e., $U = 0$) is

$$\bar{h} = e^{-\bar{x}} \sum_{n=0}^{\infty} A_n \left(e^{-2\bar{x}}\right)^n, \tag{II.15e}$$

which, by construction, is consistent with the asymptotic ordering (II.8) as $\bar{x} \to \infty$, and shows explicitly the exponential gauge function $e^{-2\bar{x}}$.

Figure 1 shows $N$-term truncations of (II.15) (solid curve) compared with both the exact solution (II.4) (•'s) and divergent series (II.5) (dashed curves). The difference between the convergent series solution (II.15) and the exact solution (II.4) is not discernible on the scale of the figure for any $N$ shown, and it is noteworthy to mention that the radius of convergence of the original series (II.5) has been exceeded.

We now provide an explanation of why the series (II.15) converges to the exact solution (II.4) of the ODE (II.3) describing a meniscus at a flat wall. The answer lies in the mapping provided by the gauge function (II.9a), as shown in Figure 3 where the complex $\bar{x}$ and $U$ planes are compared. In the $\bar{x}$ plane of Figure 3, circles of convergence for (II.5) centered around $\bar{x}$=0 are drawn for various $\theta$ values, based on the conjectured closest singularity (to $\bar{x}$ = 0), $\bar{x}_s(\theta)$, using (II.6). For $\theta = 0$, no circle is drawn, since $\bar{x}_s(\theta)$ (which sets the radius) is zero. Note, that these circles of convergence each intersect the positive real line. In particular, for $\theta = \pi/4$, this intersection occurs at the same location as the radius of convergence of series (II.5) shown in Figure 1 by a solid vertical line; this correspondence holds for all other values of $\theta$, as expected from Taylor's theorem. In the $U$ plane of Figure 3, the circle of convergence for (II.15) is drawn, centered at $U = 0$ and with mapped radius of $|e^{-2\bar{x}_s}|$; note that this circle now extends to the boundary of the physical domain for $\theta = 0$ and extends beyond it for $\theta > 0$, which explains why (II.15) converges over the entire physical domain for all values of $\theta$. The circles of convergence in Figure 3 are, of course, still *conjectured* because, in constructing the mapping in Figure 3, we are assuming that the singularity $\bar{x}_s(\theta)$ (given by (II.6)) is the closest singularity to $\bar{x} = 0$ and that no other singularities map to $U$ singularities closer to $U = 0$. In addition to the evidence given in Section II.2, further evidence that supports this conjecture is provided in the Domb-Sykes [19] plots in Figure 4, where the radius of convergence deduced from the numerical ratio-test is consistent with the locations of the mapped singularities in Figure 3. It is worth noting that knowledge of these singularities is not required to implement the exponential gauge function transformation (II.9) that leads to a convergent series solution.

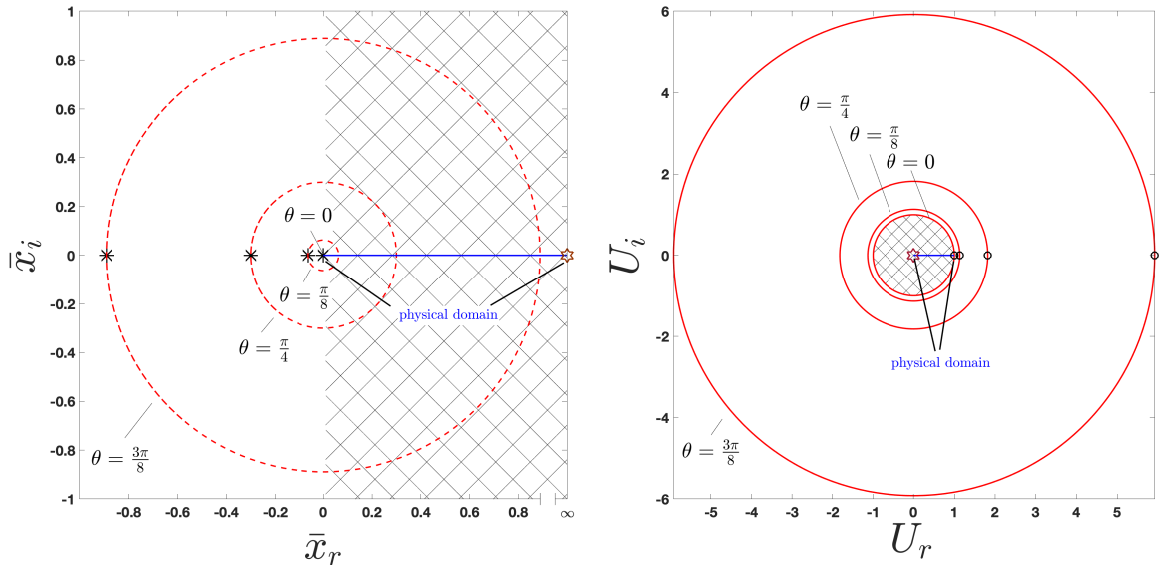


**Figure 3:** The effect of the gauge function transformation (II.9a) on the singularities $\bar{x}_s$ given by (II.6) for various $\theta$ values, showing their placement on the negative real $\bar{x}$ line ($*$'s, left) and their image on the positive real $U$ line ($\circ$'s, right). The dashed circles shown in the $\bar{x}$ plane deliniate the regions of convergence of series (II.5) for various indicated $\theta$ values. The circles shown in the $U$ plane delineate the regions of convergence of (II.15) for the same $\theta$ values.

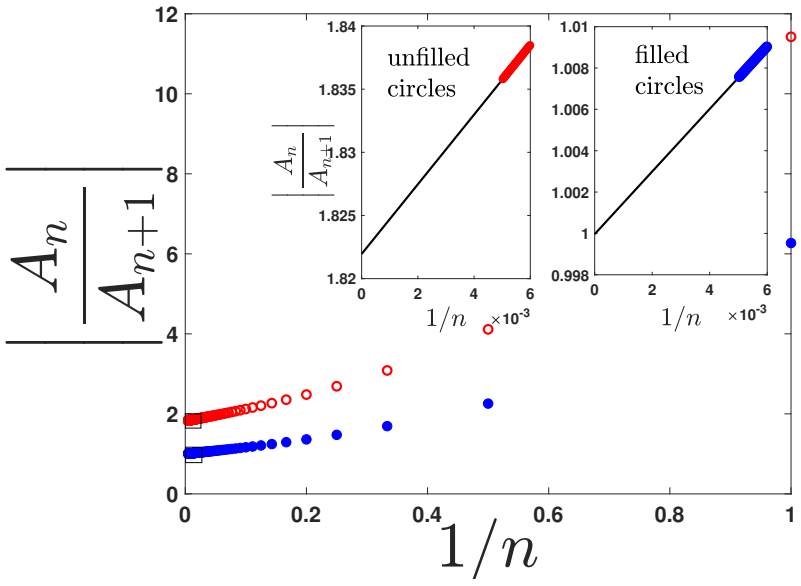


**Figure 4:** Domb-Sykes plot for (II.15), for $\theta = \pi/4$ (upper curve, $\circ$'s) and $\theta = 0$ (lower curve, $\bullet$'s), indicating (via the numerical ratio-test) radii of convergence consistent with Figure 3.

## II.4 Convergent power series solution results

The absolute error (absolute value of the difference) between (II.15) and the exact solution (II.4) is shown in Figure 5a, which indicates convergence (as $N$ increases) for a continuum of angles $\theta$, as prescribed in Figure 5b. Figure 5 is generated for the smallest possible contact angle ($\theta = 0$) and thus, by virtue of (II.3) being an autonomous ODE, contains interface shapes for all contact angles as shifted semi-infinite domains; this is indicated in the figure. The maximum error occurs at the wall and is shown versus $N$ for $\theta = 0$ in Figure 6.

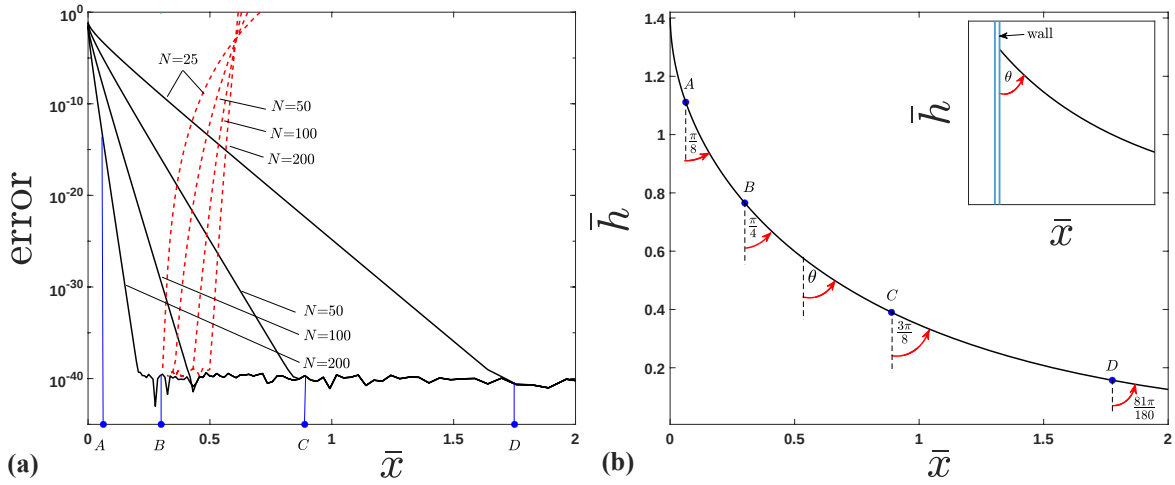


**Figure 5:** (a) Absolute error (absolute value of the difference) between $N$-term truncations of series (II.15) and the exact solution to (II.3) given by (II.4) for $\theta = 0$ (solid lines). Labeled vertical lines show the wall at various contact angles specified in the adjacent figure. For $\theta = \pi/4$, the wall is at point $B$ and the error between the divergent series (II.5) and the exact solution (II.4) is shown by the dashed lines. (b) "Master" solution to (II.3) at $\theta = 0$, illustrating the $\theta$ values at points $A$, $B$, $C$, and $D$ for potential wall locations in (a).

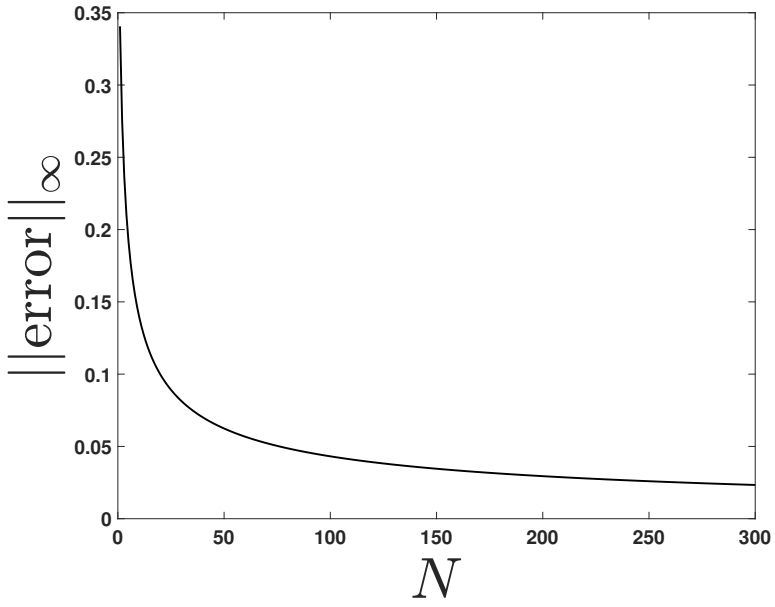


**Figure 6:** Maximum absolute error (maximum of the absolute value of the difference) between $N$-terms truncations of (II.15) and the exact solution (II.4) (occurring at $\bar{x} = 0$ and $\theta = 0$), plotted versus $N$.

## II.5 Summary: The Flat Wall Problem

In this problem, we provided a convergent power series solution to the problem of a meniscus at a flat wall, by means of transforming the original ODE in terms of variable substitutions (an exponential gauge function in this problem) that are motivated by the asymptotic expansion about $\bar{x} \to \infty$. The transformation/gauge function mapped the dominant convergence-limiting singularities out of the physical domain; also, convergence-limiting singularities do not need to be known *a priori* but their locations are deduced nonetheless. The exponential gauge function used in this work handled singularities in such a way to achieve the demonstrably convergent series solutions. Our results indicate that asymptotic behaviors can be useful to motivate gauge functions to overcome power series divergence. We will utilize this knowledge in the examination of the

Cylindrical Wall Problem and Sakiadis boundary layer roblem of Chapters III and IV. Note that for consistency in the remaining sections of this dissertation, we use $a_n$ and $A_n$ (with different accent marks) to denote the coefficients of the diverging and converging series solutions, respectively. Moreover, we use $U$ (in the Flat Wall, Cylindrical Wall, and Newtonian Sakiadis Problems) or $U-1$ (in the Newtonian and Non-Newtonian Sakiadis Problems) to denote the gauge function used to recast a diverging power series as a converging power series solution.

# III. The meniscus formed on the outside of a circular cylinder immersed in a static liquid pool: effective implementation of the Euler transformation

Portions of this chapter are taken directly from a manuscript published in *IMA Journal of Applied Mathematics* [13]. Some notation and verbiage have been changed from that submission to enhance the readability of the thesis document as a whole.

## III.1 Problem statement and formulation

The shape of a static interface (meniscus) formed on the outside of a vertical cylinder that is partially submerged in an infinite horizontal pool has been studied since the early 1900s. This problem was first examined in the literature by Ferguson [21] who obtained solutions for cylinders having large radii. Since then, the problem has been solved numerically for wire coating and other various applications [22, 23]. James [24] and later Lo [12] used the method of matched asymptotic expansions [25] to predict explicit expressions for the height of the meniscus along the cylindrical wall in the limit of small Bond number, $B$, as defined in (III.1d) below. More recent extensions of this configuration are found in coating of optical fiber sensors and microfluids [26, 27] in liquid pools of finite extent.

The problem examined here is configured as follows. An infinite horizontal pool of liquid with density, $\rho$, is subject to gravity, $g$, and is in contact with air of negligible density. A cylindrical

wall of radius, $R$, is placed vertically in the pool and the liquid intersects the wall with a contact angle, $\theta \in (0, \pi)$ (measured through the liquid). The air–liquid interface has surface tension, $\sigma$, and its height above (or below) the static pool, located at $z = 0$, is parameterized as $z = H(r)$ where $r$ is the radial distance from the axis of symmetry of the cylinder. For this configuration, the Young–Laplace equation couples with the hydrostatic pressure field to yield the following dimensionless equation and boundary conditions for $\bar{r} \in [1, \infty)$:

$$\frac{d}{d\bar{r}}\left[\frac{\bar{r}\frac{d\bar{H}}{d\bar{r}}}{\left[1+(\frac{d\bar{H}}{d\bar{r}})^2\right]^{1/2}}\right] - B\bar{r}\bar{H} = 0, \tag{III.1a}$$

$$\frac{d\bar{H}}{d\bar{r}} = -\cot\theta \text{ at } \bar{r} = 1, \tag{III.1b}$$

$$\bar{H} \to 0 \text{ as } \bar{r} \to \infty, \tag{III.1c}$$

where

$$\bar{r} = \frac{r}{R}\ ,\ \bar{H} = \frac{H}{R}\ ,\ B = \frac{\rho g R^2}{\sigma}. \tag{III.1d}$$

In (III.1d), the overbars denote dimensionless variables, and $B$ is the Bond number, which provides a ratio of characteristic scales for gravitational stress, $\rho g R$, and surface tension stress, $\sigma/R$, that compete to deform the interface.

The nonlinear system (III.1), may be solved approximately on a finite domain by shooting, collocation, or other numerical methods. The intention of this work is to provide, for the first time, an analytical solution for the interface shape governed by (III.1) over the entire semi-infinite domain, which is expressed here as a power series. Although the standard power series solution to (III.1) diverges (as shown in Section III.2), we combine two resummation techniques to overcome this difficulty and to construct a single convergent expansion. In Section II.3, we constructed a convergent series solution for the Flat Wall Problem by judiciously choosing an independent variable (which becomes the gauge function in a power series expansion) motivated by its asymptotic behavior at large distances from the wall [11]. In this work, we employ a

similar approach to construct a convergent series solution that is asymptotically consistent at both ends of the domain. We combine this asymptotic consistency with the well-known Euler transformation [25] to arrive at our convergent power series solution. The relatively simple structure of this problem enables us to examine the efficacy of asymptotically consistent power series resummation methods for solving nonlinear ODEs introduced by Barlow et al. [1].

We validate our power series solution by comparing its results with a numerical solution, as well as the $B \to 0$ matched asymptotic solution for the height of the meniscus at the cylinder developed by Lo [12]. As a general note here, asymptotic series are often divergent and are thus limited by optimal truncation constraints. Additionally, the effort to determine higher order corrections can be significant [25]. On the other hand, asymptotic methods are particularly efficient at describing limiting regimes with just a few terms and are a staple of fluid mechanics and other disciplines. The advantage of the power series method used here is that no overlap region is required as in matched asymptotics, and, by virtue of being a convergent power series series, our solution may be refined to within machine precision.

As stated above, the Euler transformation is embedded in our power series result. It is known that when the coefficients of the original divergent power series are used to construct the Euler coefficients, finite precision errors inherent to the original series coefficients become magnified [28]—this restricts solution accuracy beyond a certain number of series terms. However, we show in this dissertation that the computational issue may be circumvented by transforming the radial variable in the system (III.1) to the Euler transform variable and obtaining the power series solution to the transformed system directly; this is equivalent to specifying the Euler transformed variable as the gauge function. This result is important as this deficiency in the Euler transformation has been observed in other problems of mathematical physics (see, for example, [29]).

## III.2 A divergent power series solution

We now consider the solution of (III.1) via power series. To begin, we make the transformation

$$\tilde{r} = \bar{r} - 1, \tag{III.2a}$$

such that $\tilde{r} = 0$ corresponds to the location where the meniscus meets cylinder wall, and write $\bar{H}(\bar{r}) = \bar{H}(\tilde{r}+1) = \bar{h}(\tilde{r})$ in equation system (III.1) to obtain

$$(\tilde{r}+1)\bar{h}'' = B(\tilde{r}+1)\bar{h}\left[(\bar{h}')^2+1\right]^{3/2} - (\bar{h}')^3 - \bar{h}', \tag{III.2b}$$

$$\bar{h}' = -\cot\theta \text{ at } \tilde{r} = 0, \tag{III.2c}$$

$$\bar{h} \to 0 \text{ as } \tilde{r} \to \infty. \tag{III.2d}$$

In (III.2), note that we have utilized primes to denote derivatives of $\bar{h}$ with respect to $\tilde{r}$, and $\tilde{r} \in [0, \infty)$.

The standard power series solution of (III.2) is found by first assuming the form

$$\bar{h}(\tilde{r}) = \sum_{n=0}^{\infty} a_n \, \tilde{r}^n \quad , \quad |\tilde{r}| < \tilde{r}_s(B,\theta), \tag{III.3a}$$

where $\tilde{r}_s(B,\theta)$ is the as-of-yet undetermined radius of convergence as function of $B$ and $\theta$. Equation (III.3a) is then substituted into (III.2b) and—after applying JCP Miller's formula and Cauchy's product rule (see Appendixes A.1 and A.2)—terms of like powers are equated to obtain

$$a_{n+2} = \frac{Bf_n - c_n - (n+1)a_{n+1} - n(n+1)a_{n+1}}{(n+1)(n+2)}, \tag{III.3b}$$

$$f_{n>0} = e_{n-1} + e_n \ , \ f_0 = e_0 \ , \ c_n = \sum_{j=0}^{n}(n-j+1)b_j a_{n-j+1}, \tag{III.3c}$$

$$e_n = \sum_{j=0}^{n}(a_j)(d_{n-j}) \ , \ d_0 = \tilde{b}_0^{3/2} \ , \ d_{n>0} = \frac{1}{n\tilde{b}_0}\sum_{j=1}^{n}\left(\frac{5}{2}j - n\right)\tilde{b}_j d_{n-j}, \tag{III.3d}$$

$$\tilde{b}_0 = 1 + b_0 \ , \ \tilde{b}_{n>0} = b_{n>0} \ , \ b_n = \sum_{j=0}^{n}(j+1)(n-j+1)a_{j+1}a_{n-j+1}, \tag{III.3e}$$

with

$$a_0 = \bar{h}(0), \text{ and } a_1 = -\cot(\theta). \tag{III.3f}$$

Note that in (III.3f), the value of $a_0$ is not specified.

At this point, we use the value of $a_0$ generated by a numerical solution to examine the behavior of the power series solution; in Section III.5 to follow, an algorithm to predict $a_0$ using the power series itself is provided. The numerical solution used here is a Chebyshev spectral method (the Chebfun package) [30] that implements piecewise polynomial interpolation to solve the nonlinear differential equation as a boundary value problem on a *finite* domain length $\mathcal{L}$; the length $\mathcal{L}$ is chosen so that doubling its size affects the finite domain solution below an infinity norm (taken between the $\mathcal{L}$ and $2\mathcal{L}$ solutions) of $O(10^{-13})$. In Figure 7, the dashed curves show the $N$-term truncation of series (III.3) for $B = 0.1$ and $\theta = \pi/4$. The power series solution (III.3) agrees with the numerical solution of (III.2) for small $\tilde{r}$ but ultimately diverges at a finite radius of convergence (indicated as a solid vertical line in Figure 7); the radius of convergence $\tilde{r}_s \approx 0.26$, which is predicted using the Domb-Sykes plot in Figure 8 (the limit as $n \to \infty$ provides the radius of convergence); the Domb-Sykes plot itself is the numerical implementation of the ratio test [25]. Similarly divergent results are obtained for other values of $\theta$ and $B$.

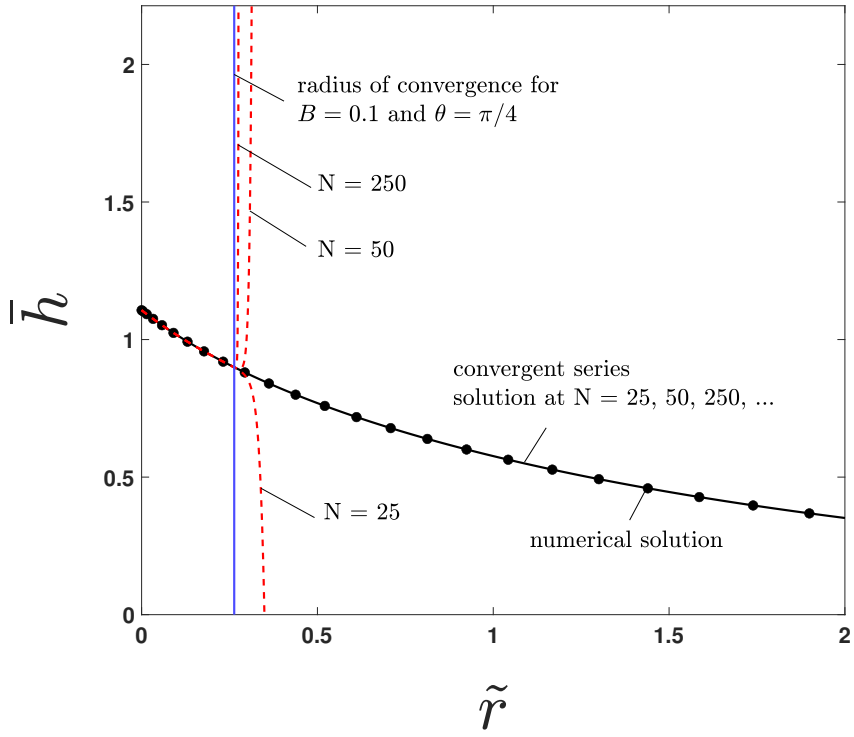


**Figure 7:** The solution to (III.2) is shown for Bond number $B = 0.1$ and a contact angle of $\theta = \pi/4$. The $N$-term truncations of the divergent series solution (III.3) (dashed curves) and the convergent series solution (III.8) (solid curve) are compared against the numerical solution with $\mathcal{L} = 60$ (•'s). The solid vertical line shows the radius of convergence, $\tilde{r}_s \approx 0.26$, computed from the Domb-Sykes plot.

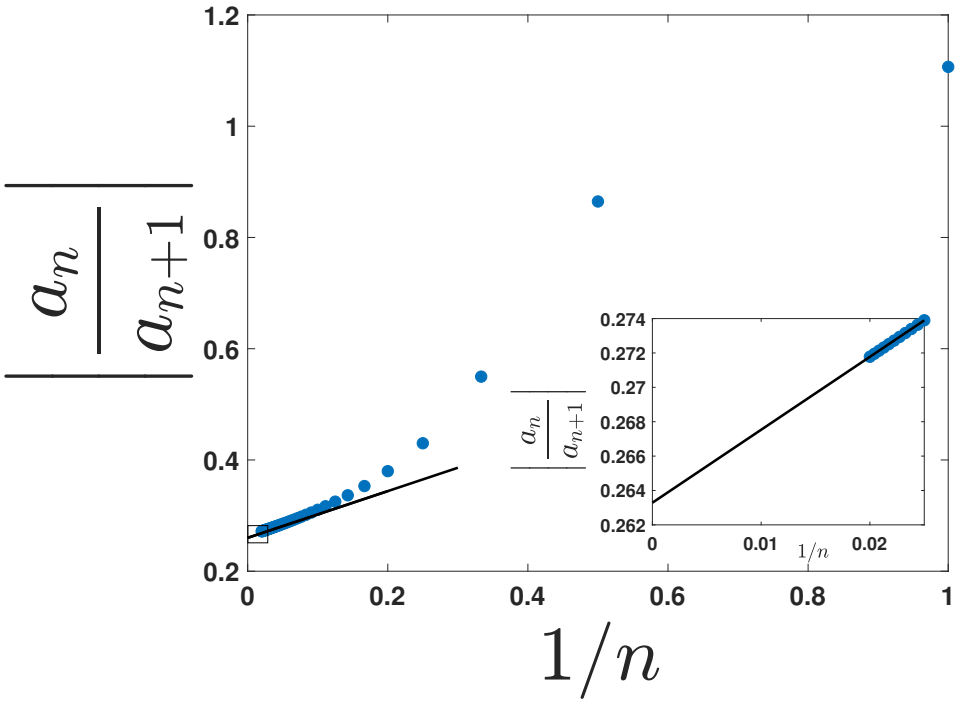


**Figure 8:** Domb-Sykes plot for (III.3) with $B = 0.1$ and $\theta = \pi/4$ for $N = 50$, indicating (via the ratio-test) a radius of convergence of $\tilde{r}_s \approx 0.26$. This is consistent with the divergent series behavior of (III.3) observed in Figure 7.

## III.3 A convergent power series solution

### III.3.1 Euler transformation

Our goal is to recast the divergent series (III.3) as another power series that converges uniformly over the entire semi-infinite domain. As in the Flat Wall Problem of Chapter II, this requires a variable transformation that maps the convergence-limiting singularity to a new location to increase the radius of convergence. To do so, we note that the coefficients of the divergent series expansion (III.3) alternate in sign. This indicates (by a corollary to Pringsheim's theorem) that the singularity responsible for divergence lies along the negative real axis [31]. As such, it is likely that application of the Euler transformation will induce convergence.

The Euler transformation is defined as

$$\bar{h}(\tilde{r}) = G(U(\tilde{r})), \tag{III.4a}$$

with

$$U = \frac{\tilde{r}}{\tilde{r} + S}, \tag{III.4b}$$

where $S > 0$ is a parameter corresponding to the approximation of the radius of convergence of the diverging series (III.3). Given a power series in $\tilde{r}$ with a negative real convergence-limiting singularity located at $\tilde{r} = -\tilde{r}_s$, a power series in $U$,

$$G = \sum_{n=0}^{\infty} \hat{A}_n U^n, \tag{III.5}$$

converges pointwise in $U$ for any positive real $S$ with $S < 2\tilde{r}_s$ (see Appendix B.2). The Euler transformation (III.4) maps the domain of the new expansion variable to be between $U = 0$ and $U = 1$, and maps the singularity such that the transformed disc of convergence contains the entire physical domain, thus creating a convergent series. As shown in Appendix B.1, the power series coefficients of the transformed function $G$ about $U = 0$ can be written explicitly in terms of the original Taylor coefficients $a_n$ in (III.3) about $\tilde{r} = 0$ as

$$\hat{A}_{n>0} = \sum_{m=1}^{n} \binom{n-1}{m-1} a_m S^m, \ \hat{A}_0 = a_0. \tag{III.6}$$

The above relation is attractive in that it may be applied to any divergent alternating series with a finite radius of convergence, whether it originates as a solution to an ODE or not. Thus, for purposes of generality, the Euler summation is often presented using an identity equivalent to (III.6) [32]. However, the implementation of Euler summation via (III.6) is computationally unstable to finite precision errors [28]. This is shown in Figure 9, where coefficients computed using (III.6) deviate from their true value beyond some finite $n$ value (here $n \approx 50$). This error originates through the recurrence relation in (III.3) for the divergent series coefficients, since it incorporates the sums and differences of expressions involving exponentially growing series

coefficients (see Figure 9). Since these coefficients are used in (III.6) to compute $\hat{A}_n$, the Euler summation coefficients incur this error.

To avoid finite precision error in computing the Euler transformation (III.4), we have found that one must avoid using the original diverging series coefficients. This is accomplished by applying the variable transformation (III.4) directly to the original ODE (III.2b) to obtain an ODE for $G(U)$. The Taylor coefficients $\hat{A}_n$ are then found as the coefficients to the power series solution in $U$ to the transformed ODE. Upon applying the Euler transformation (III.4), the ODE (III.2) becomes

$$G'' = \frac{2}{1-U}G' + \frac{((1-U)^4 G'^2 + S^2)^{3/2} BG}{(1-U)^4} - \frac{(1-U)^3 G'^3}{S(US+1-U)} - \frac{SG'}{(1-U)(US+1-U)}, \quad \text{(III.7a)}$$

$$G' = -S\cot\theta \text{ at } U = 0, \quad \text{(III.7b)}$$

$$G \to 0 \text{ as } U \to 1. \quad \text{(III.7c)}$$

In (III.7), the primes denote derivatives of $G$ with respect to $U$, and $U \in [0,1)$. We next assume a solution to (III.7a) of the form

$$G(U) = \sum_{n=0}^{\infty} \hat{A}_n U^n \ , \ |U| < U_s(B,\theta). \quad \text{(III.8a)}$$

Using JCP Miller's formula (A.1) and Cauchy's product rule (A.2), a recurrence can be obtained (see Appendix B.4) for the Taylor coefficients $\hat{A}_n$ as

$$\hat{A}_{n+2} = \frac{S^2}{(n+1)(n+2)} \sum_{k=0}^{n} \binom{k+3}{3} w_{n-k}, \quad \text{(III.8b)}$$

where

$$w_n = f_n + \sum_{k=0}^{n} (q_k - t_k - u_k) r_{n-k} \ , \ f_n = \frac{2}{S^2} \sum_{k=0}^{n} (-1)^k \binom{3}{k} (n-k+1) \hat{A}_{n-k+1}, \quad \text{(III.8c)}$$

$$q_n = B \sum_{k=0}^{n} \ell_k p_{n-k} \ , \ \bar{\ell}_n = S + (1-S)\delta_{n,0} \ , \ \ell_n = \sum_{k=0}^{n} \bar{\ell}_k \hat{A}_{n-k} \quad \text{(III.8d)}$$

$$u_n = \frac{1}{S} \sum_{k=0}^{n} (-1)^k \binom{2}{k} (n-k+1) \hat{A}_{n-k+1} \quad \text{(III.8e)}$$

$$d_n = \sum_{k=0}^{n} u_k u_{n-k} \ , \ \ t_n = \sum_{k=0}^{n} d_k u_{n-k} \ , \ \ \bar{d}_n = d_n + \delta_{n,0} \tag{III.8f}$$

$$r_n = (1-S)^n - (1-S)^{n-1}(1-\delta_{n,0}), \tag{III.8g}$$

$$p_{n>0} = \frac{1}{n\bar{d}_0} \sum_{k=1}^{n} \left( \frac{5}{2}k - n \right) \bar{d}_k p_{n-k} \ , \ \ p_0 = \bar{d}_0^{3/2}, \tag{III.8h}$$

with

$$\hat{A}_0 = \bar{h}(\tilde{r}=0), \text{ and } \ \hat{A}_1 = \cot(\theta), \tag{III.8i}$$

where the Kronecker notation is used such that $\delta_{n,0}$ is 0 when $n \neq 0$ and 1 when $n = 0$. According to equation (III.8a) and the Euler transformation (III.4), the interface shape can be written in terms of physical domain coordinates as

$$\bar{h}(\tilde{r}) = \sum_{n=0}^{\infty} \hat{A}_n \left( \frac{\tilde{r}}{\tilde{r}+S} \right)^n . \tag{III.8j}$$

The result (III.8) is the desired uniformly convergent representation of the solution via the Euler transformation, where clearly $\left(\frac{\tilde{r}}{\tilde{r}+S}\right)$ is the gauge function. Returning to Figure 9, a comparison is provided between the coefficients computed by transforming divergent coefficients according to (III.6) and those directly from the transformed differential equation according to (III.8). We observe that for $n < 50$, coefficients obtained are identical. However, for larger $n$ values, we see that the coefficients calculated from (III.6) begin to grow due to aforementioned finite precision error, and deviate from those obtained by (III.8). We note here that the solution (III.8) converges slowly, and that is evidenced by the slow decline in the magnitude of $\hat{A}_n$ as $n$ increases in Figure 9.

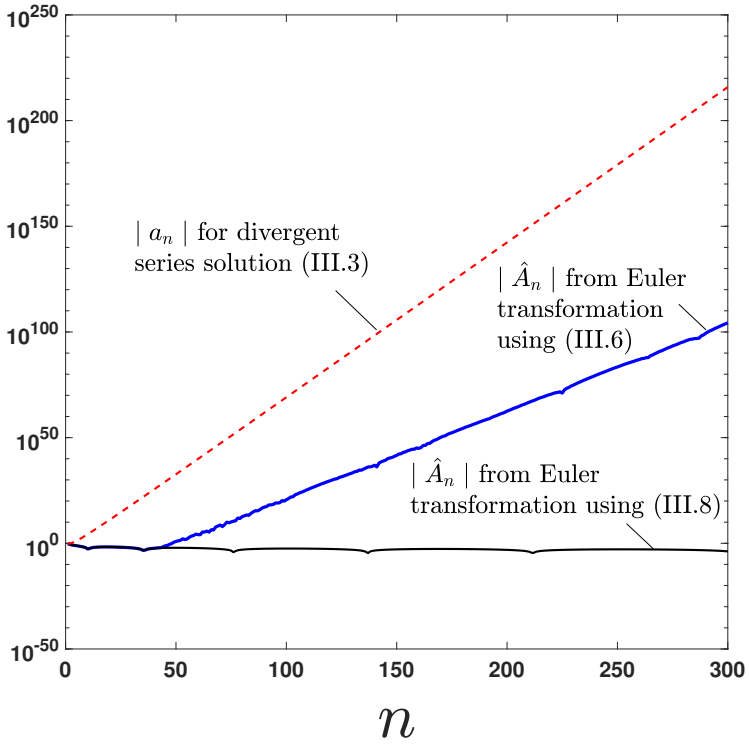


**Figure 9:** Coefficients of the divergent series solution $a_n$ in (III.3) (dashed curve), Eulerized transformed coefficients $\hat{A}_n$ in (III.6) (solid curve), and convergent series solution $\hat{A}_n$ in (III.8) (solid curve), plotted vs. $n$, for $\theta = \pi/4$ and $B = 0.1$ with $S = (2-\sqrt{2})/2$ calculated using (III.12). All coefficients are computed in double precision.

### III.3.2 Prefactor inclusion

Convergence of the power series solution (III.8) may be improved by incorporating the asymptotic behavior of the solution for $\bar{h}(\tilde{r})$ as $\tilde{r} \to \infty$. We note that the power series solution (III.3) implicitly matches the correct asymptotic behavior as $\tilde{r} \to 0$, and thus efficiently represents the solution near the cylinder wall. To guide the form of a convergent resummation of (III.3), the asymptotic behavior of $\bar{h}$ as $\tilde{r} \to \infty$ is first determined. The height constraint (III.2d) necessarily implies that $\bar{h}' \to 0$ as $\tilde{r} \to \infty$. Thus, using the method of dominant balance [20] on (III.2b) we neglect terms

that are quadratic or higher in $\bar{h}'$ and obtain

$$(\tilde{r}+1)^2\bar{h}'' + (\tilde{r}+1)\bar{h}' - B(\tilde{r}+1)^2\bar{h} = 0 \text{ as } \tilde{r} \to \infty. \tag{III.9}$$

The solution of (III.9) is expressed in terms of the modified Bessel function (of the second kind) of zeroth order as

$$\bar{h}(\tilde{r}) \sim D\ K_0\left(\sqrt{B}(\tilde{r}+1)\right) \text{ as } \tilde{r} \to \infty, \tag{III.10}$$

where $D$ is an undetermined constant that can only be found through consideration of finite $\tilde{r}$ behavior. For $\theta$ near $\pi/2$, note that the asymptotic result (III.10) is an excellent approximation for $\bar{h}$ for all $\tilde{r}$, and the boundary condition (III.2c) may be applied to determine $D$ (see Appendix B.3). For smaller angles, the power series (III.8) may be improved by combining the modified Bessel function (III.10) with the Euler transformation (III.4b) as

$$\bar{h}(\tilde{r}) = K_0\left(\sqrt{B}(\tilde{r}+1)\right) \sum_{n=0}^{\infty} \bar{A}_n\ U^n. \tag{III.11a}$$

In (III.11a), $U$ is the Euler transformation defined in (III.4b), and the estimate for the radius of convergence, $S$, is determined in what follows. Note that as $\tilde{r} \to \infty$, the series in (III.11a) approaches a constant, preserving the asymptotic Bessel function behavior (III.10) in this limit.

To solve for the Euler coefficients, $\bar{A}_n$, in (III.11a), we use Cauchy's product rule (see Appendix A.2), and the formula for the Taylor coefficients of $K_0(\sqrt{B}(\tilde{r}+1))^{-1}$ in an expansion about $U = 0$, relating $r$ and $U$ through (III.4b). This is done using the defining ODE for the modified Bessel function, and applying the same techniques used to compute the coefficients $\hat{A}_n$ in Appendix B.4; details are provided in Appendix B.5 to obtain the coefficients

$$\bar{A}_n = \sum_{k=0}^{n} \zeta_k \hat{A}_{n-k}, \tag{III.11b}$$

where

$$\zeta_n = \frac{-1}{\bar{\zeta}_0} \sum_{k=1}^{n} \bar{\zeta}_k \zeta_{n-k}\ \ ,\ \ \zeta_0 = \bar{\zeta}_0^{-1}\ \ ,\ \ \bar{\zeta}_0 = K_0(\sqrt{B})\ \ ,\ \ \bar{\zeta}_1 = -S\sqrt{B}K_1(\sqrt{B}), \tag{III.11c}$$

$$\bar{\zeta}_{n+2} = \frac{1}{(n+1)(n+2)} \left[ \sum_{k=0}^{n} \left\{ (k+1)\bar{\zeta}_{k+1}(2-\rho_{n-k}) + BS^2 \binom{k+3}{3} \bar{\zeta}_{n-k} \right\} \right] \tag{III.11d}$$

$$\rho_n = 1 - (1-S)^{n+1}. \tag{III.11e}$$

In writing (III.11a), we use the fact that the Bessel function prefactor does not introduce new singularities that impact convergence, since the actual function that is Euler-transformed and then subsequently expanded in a power series is $[\bar{h}(\tilde{r})][K_0(\sqrt{B}(\tilde{r}+1))^{-1}]$. It is well known [33] that the zeros of $K_0$ occur in the left-half plane, which means any value of $S$ that successfully Euler sums $\bar{h}$ must also do so for the function $[\bar{h}(\tilde{r})][K_0(\sqrt{B}(\tilde{r}+1))^{-1}]$.

To utilize (III.8), the estimate for the radius of convergence, $S$, is needed (recall that Appendix B.2 indicates that S does not need to be exact). Note that the Domb-Sykes plot could be used to establish its value exactly for given parameter values $\theta$ and $B$. However, to simplify implementation, a systematic estimate may be obtained by considering the asymptotic limits of small and large Bond numbers. When the Bond number is small ($B \to 0$), both sides of (III.2b) can be integrated once, and is thus reduced to a 1$^{\text{st}}$-order ordinary differential equation as

$$\bar{h}' = \frac{-\cos\theta}{\sqrt{(\tilde{r}+1)^2 - \cos^2\theta}},$$

which has a singularity at the location where the denominator is zero and the slope is infinite. The singularity lies on the negative $\tilde{r}$ axis, whose precise location depends on $\theta$. The location of infinite slope imposes a radius of convergence on the physical domain from the closest root to the $\tilde{r} = 0$ location, and the radius of convergence imparted is given by

$$\tilde{r}_s|_{B\to 0} = |1 - |\cos\theta|| \quad , \quad B \ll 1. \tag{III.12}$$

To find $\tilde{r}_s$ of (III.3) as $B \to \infty$, one can interpret the problem dimensionally as that of a cylinder with a large radius in a fluid with fixed physical properties. In such a limit, the cylinder surface may be viewed as flat over a large portion of the domain. The meniscus of a flat wall satisfies an autonomous ODE and has an analytical solution [9]. The convergence-limiting singularity

corresponds to the location where the slope of the interface solution is infinite even if outside the physical domain. That singularity is imparted because all flat wall interface solution lie along the same master curve that is translated to meet conditions at the wall. This location is given by (II.6) provided in Section II.2 [11] and is rewritten below in terms of current notation and non-dimensionalized variables as

$$\tilde{r}_s|_{B\to\infty} = \frac{\left|\cosh^{-1}\sqrt{2} - \cosh^{-1}\sqrt{\frac{2}{1-\sin\theta}} + \sqrt{2+2\sin\theta} - \sqrt{2}\right|}{\sqrt{B}}, \quad B \gg 1. \tag{III.13}$$

We have surveyed the parameter ranges $\theta \in (0, \pi)$ and $B \in [0.001, 100]$, and find that the ratio of $\tilde{r}_s$ found numerically (using a numerical $a_0$ to initiate the recursion in (III.3)) to the estimated $\tilde{r}_s$ found using (III.12) and (III.13) always lies between 0 and 2 when chosen judiciously as follows—this satisfies the constraints for a convergent Euler summation (see Appendix B.2). We have found that the maximum error in the radius of convergence in using either (III.12) or (III.13) is obtained when the radii predictions are equal. Setting (III.12) equal to (III.13) leads to a master curve to solve for a critical value of $B$, denoted by $B_{crit}$, as a function of contact angle $\theta$ as

$$B_{crit} = \left[\frac{\cosh^{-1}\sqrt{2} - \cosh^{-1}\sqrt{\frac{2}{1-\sin\theta}} + \sqrt{2+2\sin\theta} - \sqrt{2}}{1 - |\cos\theta|}\right]^2, \tag{III.14}$$

which is plotted in Figure 10. In this figure, errors in the radius of convergence (compared with the numerical solution) become smaller as one moves away from the plotted curve. We can use this fact, then, to determine the estimate for the radius of convergence, $S$, in the Euler transformation (III.4) which is used in the convergent series solutions (III.8) and (III.11). Consistent with the derivation, (III.13) is used to determine $S$ for $B > B_{crit}$, and (III.12) is used to predict $S$ for $B < B_{crit}$. For any combination of $B$ and $\theta$ values that fall along the solid line in Figure 10, $\tilde{r}_s$ (i.e., $S$) obtained from (III.12) and (III.13) are identical, but (III.12) is preferred for simplicity. In the results and figures that follow, we use (III.12) and (III.13) along with Figure 10 to obtain $S$ analytically.

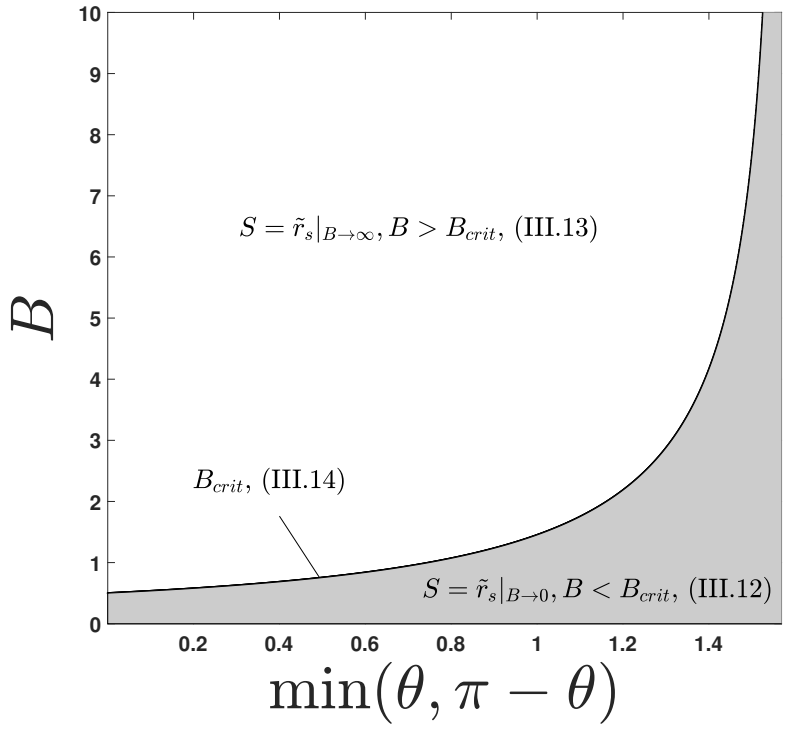


**Figure 10:** Determination of $S$ using the relationship given by (III.14). For any combination of $B$ and $\theta$ values above or below the solid line, we choose (III.13) or (III.12), respectively, to calculate the corresponding radius of convergence, $\tilde{r}_s$, for its use in (III.8) and (III.11). For any combination of $B$ and $\theta$ values on the solid line, $B_{crit}$ from (III.14), one may choose to use either of the equations. The plot is not needed for $\theta = \pi/2$ because the solution is horizontal for all Bond numbers.

## III.4 Convergent power series solution results

In this section, we examine the performance of the series (III.11) by direct comparison with numerical results. We begin by noting that the system (III.1) has a reflection property that the solutions for $\theta < \pi/2$ are identical in shape to those for that $\theta > \pi/2$ provided $\mid \theta - \pi/2 \mid$ are the same. The only difference is that the solutions are mirror images, so solutions rising above the horizontal pool as $r \to \infty$ for $\theta < \pi/2$ fall below that same horizontal height. Thus, it suffices to

only consider solutions for $\theta < \pi/2$ in what follows. Figure 11a shows the absolute error (the absolute difference) between $N$-term truncations of the convergent series solution (III.11) and the numerical solution for $B = 0.1$ and $\theta = \pi/4$. The value of $\bar{h}(\tilde{r} = 0)$ from the numerical solution is used as the value of $a_0$ in constructing Figure 11a (as well as Figures 12a and 13a in this section). Thus, the lowest absolute error (the absolute value of the difference between the convergent series solution (III.11) and the numerical solution) in Figure 11a is observed at the wall. Note that the indicated errors are continually reduced for all $\tilde{r}$ as $N$ is increased beyond those values shown in the figures, but the trends indicated are maintained. Thus, desired accuracy can be achieved with sufficiently large $N$.

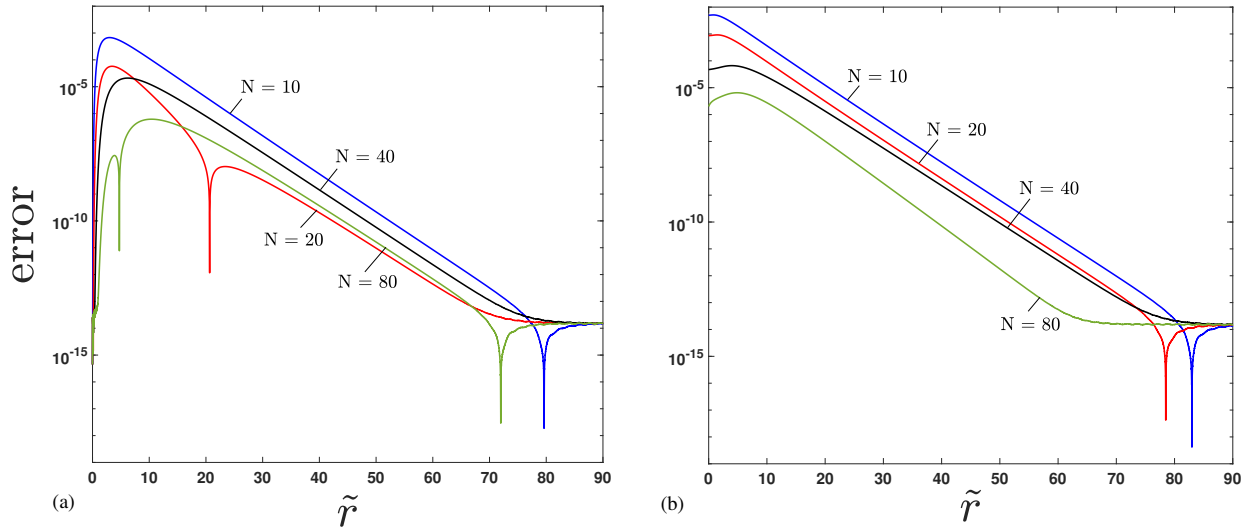


**Figure 11:** Absolute error (the absolute value of the difference) between $N$-term truncations of the convergent series solution (III.11) and the numerical solution with a domain length $\mathcal{L} = 240$ for $B = 0.1$ and $\theta = \pi/4$ plotted versus $\tilde{r}$ using (a) $a_0 = \bar{h}(\tilde{r} = 0)$ generated by the numerical solution, and (b) the predicted value of $a_0$ using the power series itself following the algorithm in Section III.5.

Figure 12a shows the maximum absolute error (maximum of the absolute value of the difference

over $\tilde{r} \in [0, \mathcal{L}]$) between the power series representation (III.11) and the numerical solution for $B = 0.1$ and various $\theta$ values, while Figure 13a shows the same for $\theta = \pi/4$ and various $B$ values. We observe that the error between the numerical and series solution decreases as contact angles approach $\pi/2$ for the same number of terms. Similarly, for the same number of terms the power series solution (III.11) becomes more accurate as the Bond number increases. Again, increased accuracy may be obtained with increasing $N$ beyond those shown in the figures. Moreover, we note that the series takes more terms to converge as $\theta \to 0$, and less terms as $\theta \to \pi/2$, for all Bond numbers.

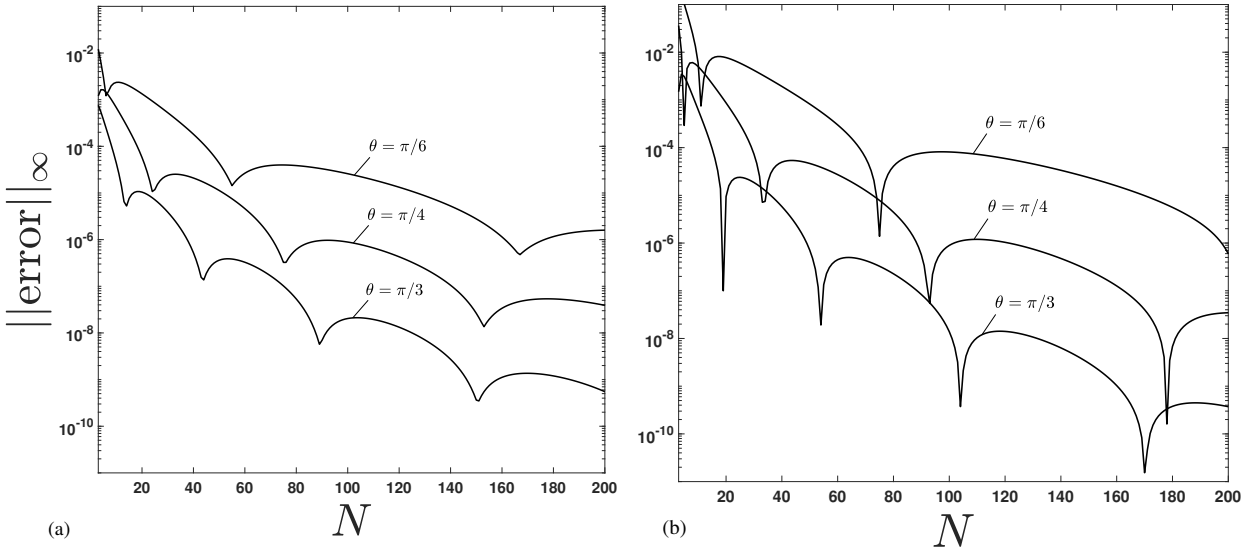


**Figure 12:** Maximum absolute error (maximum of the absolute value of the difference) taken over $\tilde{r} \in [0, \mathcal{L}]$ between $N$-term truncations (shown by •'s) of the convergent resummation (III.11) and the numerical solution for $B = 0.1$ and $\theta = \pi/6$ (with $\mathcal{L} = 240$), $\pi/4$ (with $\mathcal{L} = 240$), and $\pi/3$ (with $\mathcal{L} = 240$), plotted versus $N$, using (a) $a_0 = \bar{h}(\tilde{r} = 0)$ generated from the numerical solution, and (b) the predicted value of $a_0$ using the power series itself following the algorithm in Section III.5.

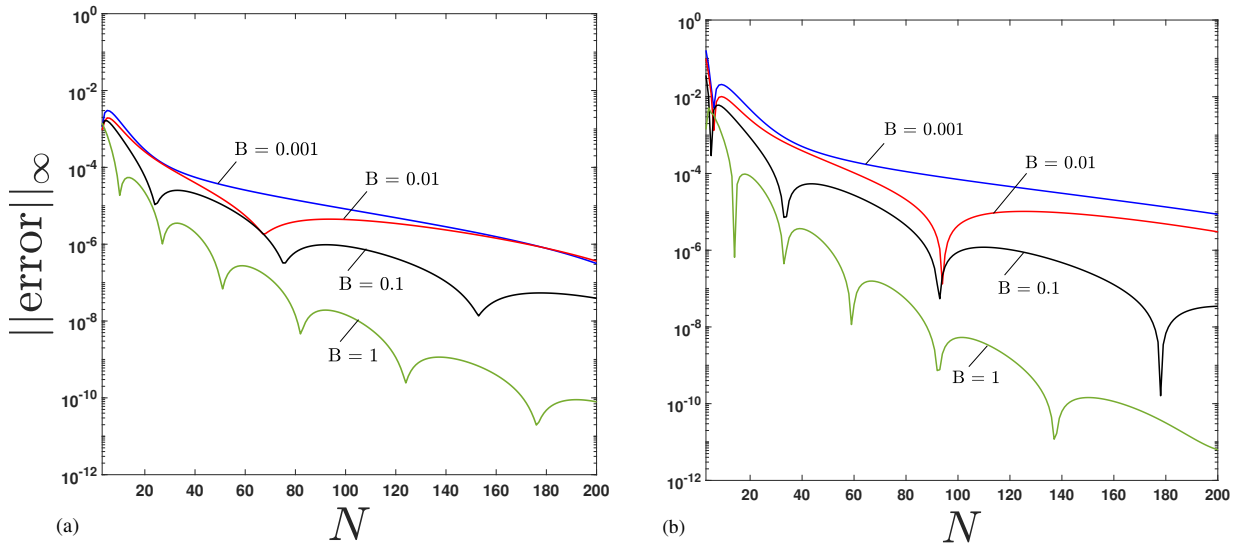


**Figure 13:** Maximum absolute error taken $\tilde{r} \in [0, \mathcal{L}]$ between $N$-term truncations (shown by •'s) of the convergent resummation (III.11) and the numerical solution for $B = 1$ (with $\mathcal{L} = 60$), 0.1 (with $\mathcal{L} = 60$), 0.01 (with $\mathcal{L} = 480$), and 0.001 (with $L = 960$), and $\theta = \pi/4$, plotted versus $N$, using (a) $a_0 = \bar{h}(\tilde{r} = 0)$ generated by the numerical solution, and (b) the predicted value of $a_0$ using the power series itself following the algorithm in Section III.5.

## III.5 Prediction of the meniscus height at the cylinder wall

Up to this point in the problem, all discussed power series results have utilized the numerically predicted value of the height at the wall as an input. We now provide the methodology to determine the height of the wall, $a_0 = \bar{h}(\tilde{r} = 0)$, using the power series itself, which precludes the need for numerical inputs altogether. The recurrence for the coefficients provides data about the structure of the solution as a function of the chosen value of $a_0$. While there are many conditions we impose on the coefficients of (III.11) to yield an equation for $a_0$, the simplest is to set the last $\bar{A}_n$ coefficient to zero. This approach has been used previously in [1]. The rationale for this

choice is based on the fact that, in a convergent series, the last coefficient, $\bar{A}_N$, must approach zero as $N \to \infty$; thus the assumption that $\bar{A}_N = 0$ is self consistent in this limit. From a purely mathematical perspective, setting $\bar{A}_N = 0$ provides one equation in one unknown $a_0$ that enables a solution. We can compute the $n$-th coefficient $\bar{A}_n(a_0)$ as a function of the chosen value of $a_0$. Since the underlying recurrence is analytical, we can differentiate it to compute derivatives with respect to $a_0$ as well. As such, we can use Newton's iteration to obtain the desired result by choosing $a_0$ to enforce the condition $\bar{A}_N = 0$.

The Newton's iteration takes the form

$$a_{0,j+1} = a_{0,j} - \frac{\bar{A}_N(a_{0,j})}{\bar{A}'_N(a_{0,j})}, \tag{III.15a}$$

where $\bar{A}'_N(a_{0,j})$ is the derivative of $\bar{A}_N$ with respect to $a_0$. To utilize (III.15a), we differentiate the coefficients in (III.11) with respect to $a_0$, and obtain

$$\bar{A}'_n = \sum_{k=0}^{n} \zeta_k \hat{A}'_{n-k}, \tag{III.15b}$$

$$\hat{A}'_{n+2} = \frac{S^2}{(n+1)(n+2)} \sum_{k=0}^{n} \binom{k+3}{3} w'_{n-k}, \tag{III.15c}$$

$$w'_n = f'_n + \sum_{k=0}^{n} r_{n-k} \left(q'_k - t'_k - u'_k\right) \quad , \quad f'_n = \frac{2}{S^2} \sum_{k=0}^{n} (-1)^k \binom{3}{k} (n-k+1) \hat{A}'_{n-k+1}, \tag{III.15d}$$

$$q'_n = B \sum_{k=0}^{n} \left\{\ell'_k p_{n-k} + \ell_k p'_{n-k}\right\} \quad , \quad \ell'_n = \sum_{k=0}^{n} \bar{\ell}_k \hat{A}'_{n-k}, \tag{III.15e}$$

$$u'_n = \frac{1}{S} \sum_{k=0}^{n} (-1)^k \binom{2}{k} (n-k+1) \hat{A}'_{n-k+1}, \tag{III.15f}$$

$$d'_n = \sum_{k=0}^{n} \left\{u'_k u_{n-k} + u_k u'_{n-k}\right\} \quad , \quad t'_n = \sum_{k=0}^{n} \left\{d'_k u_{n-k} + d_k u'_{n-k}\right\} \quad , \quad \bar{d}'_n = d'_n, \tag{III.15g}$$

$$p'_n = \frac{1}{n\bar{d}_0} \sum_{k=1}^{n} \left\{ \left(\frac{5}{2}k - n\right) \left(\bar{d}'_k p_{n-k} + \bar{d}_k p'_{n-k}\right) \right\} - \frac{1}{n\bar{d}_0^2} \bar{d}'_0 \sum_{k=1}^{n} \left(\frac{5}{2}k - n\right) \bar{d}_k p_{n-k}, \tag{III.15h}$$

$$p'_0 = \frac{3}{2} \bar{d}_0^{1/2} \bar{d}'_0, \tag{III.15i}$$

with

$$\hat{A}'_0 = 1, \text{ and } \hat{A}'_1 = 0. \tag{III.15j}$$

Using an arbitrary initial guess, (III.15) is used to predict $a_0$, which approaches the correct value as $N \to \infty$, as evidenced by the error plots in Figures 11b, 12b, and 13b.

Apart from comparing directly with numerical results, our predictions of the height of the interface at the wall ($\bar{h} = a_0$) and resulting interface shape agree well with an analytical expression derived for small interfacial slopes (see Appendix B.3) over the whole radial domain. This occurs when $\theta$ is near $\pi/2$. Under such circumstances, the constant $D$ in (III.10) can be determined based on constraints at the wall. According to (III.11), this means that $\bar{A}_0 = D$ for small slopes. If one utilizes the algorithm (III.15) to determine the constant $A_0$ by setting $A_1 = 0$, we obtain the same value of the constant $D$ obtained the small slope approximation. This provides additional insight into how the series (III.11) with the modified Bessel prefactor accelerates convergence. For small slopes at the wall, one term in the expansion provides an excellent prediction of the interface shape, while higher order terms in $U$ contribute only incremental improvement. Far from the wall, the same comment applies—as the small slope approximation (III.10) is always valid, the Bessel function prefactor in (III.11) assures that only a few terms in the expansion in $U$ (or equivalently $\tilde{r}$) are needed to capture the solution behavior.

## III.6 Performance of power series and matched asymptotic solutions

In this section, we compare predictions of the height of the interface at the wall, $a_0$, from the power series solution (III.11) using the algorithm of Section III.5, with those of the matched asymptotic solution by Lo [12] in the limit $B \to 0$. Figure 14 compares the solutions generated by the $N$-term truncation of the convergent power series solution (III.11), the first order matched asymptotic solution of Lo [12], and the second order matched asymptotic solution of Lo [12] (see (B.58) and (B.59) in Appendix B.6, respectively), with the numerical solution for $B = 100$, 10, 1, 0.1, 0.01, and 0.001 and $\theta = \pi/4$, at the wall of the cylinder ($\tilde{r} = 0$).

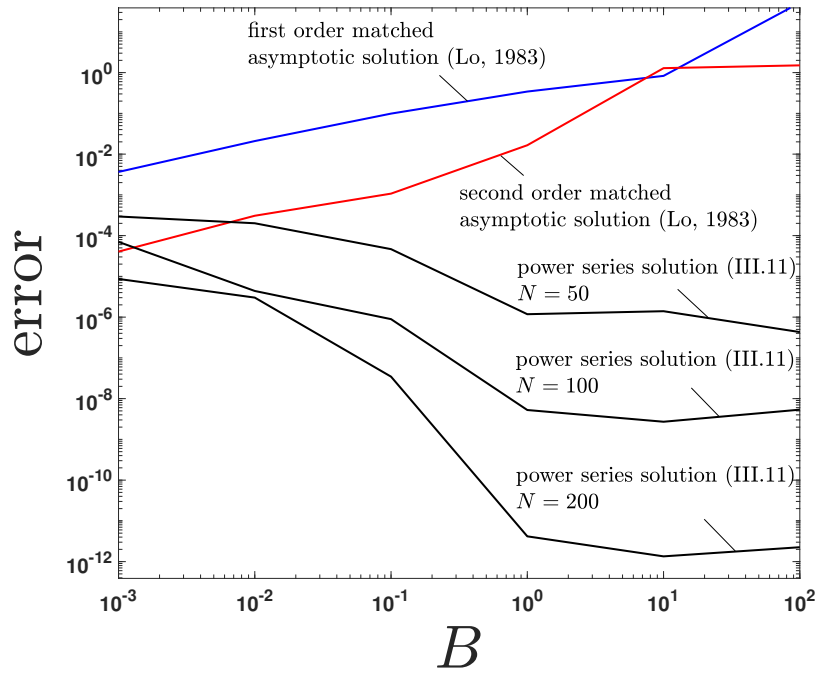


**Figure 14:** Absolute error between predictions of the height of the meniscus at the wall of the cylinder ($\tilde{r} = 0$) using the power series (III.11) and the numerical solution, compared with error from the first (B.58) and second (B.59) order matched asymptotic solutions of Lo [12] for $\theta = \pi/4$.

As shown in Figure 14, the accuracy of the asymptotic solution improves as $B$ approaches zero, as expected from asymptotic theory. That said, the series solution (III.11) is effective over a broad range of Bond numbers, and in fact performs with high accuracy even in the range where asymptotic analysis is justified; that is, provided a sufficient number of terms in the series are included.

In the case of small Bond numbers where Lo's solution has sufficient accuracy, one could choose to use the value of $a_0$, the height of the liquid meniscus at the wall, from the method of matched asymptotic solutions [12], shown in (B.58) and (B.59), and use the convergent series solution (III.11) to generate the full shape of the interface. The accuracy of the matched asymptotic solution might

be improved by considering a third order match, but as is evident from the work of Lo [12], the generation of higher order matches is arduous. Additionally, asymptotic series are subject to optimal truncation errors, so there is a limit to the improvement that may be achieved by adding such corrections. By contrast, the power series approach yields a relatively simple recursion that can be used for solutions of desired accuracy by simply including additional terms in the series.

## III.7 Summary: The Cylindrical Wall Problem

In this problem, the asymptotically motivated Euler transformation was utilized to transform a divergent power series solution to a convergent one, where the influence of singularities were mapped outside the physical domain. Furthermore, we have obtained—for the first time—an exact solution for the shape of the meniscus formed outside a partially submerged vertical cylinder in an infinite horizontal static pool. The efficacy of the power series solution has been systematically tested against numerical and previously-derived matched asymptotic solutions. Moreover, the complexity of the matched asymptotic solution precludes additional higher-order corrections from being generated practically. The power series solution, generated recursively, is attractive for its ease of use for all values of $B$, $\theta$, and over the entire physical domain.

# IV. The Sakiadis boundary layer

## PROBLEM

Portions of this chapter are taken directly from manuscripts that have been published in *IMA Journal of Applied Mathematics* [11] (also previously cited for the Flat Wall Problem in Chapter II) and *Journal of Physics of Fluids* [16]. Some notation and verbiage have been changed to enhance the readability of the thesis document as a whole.

Our research group has examined the Sakiadis boundary layer problem for Newtonian fluids (fluids with constant viscosity) in work prior to this thesis, and obtained a conjectured exact analytical solution [11]. Here, we extend the work to examine non-Newtonian fluids, where viscosity is no longer constant. Some of the details from the Newtonian Sakiadis Problem in [11] are relevant to the Non-Newtonian Sakiadis Problem, and are provided in Section IV.1. In Section IV.2, we explicitly examine the complications of non-constant fluid viscosity and arrive at analytical expressions for the resulting boundary layer flow.

The Sakiadis boundary layer[34] is a fundamental flow field in processes where laminar liquid films are coated onto moving substrates [14]. One of its key physical implications is in the area of high speed curtain coating, where the boundary layer length is essential to the mechanism of hydrodynamic assist that can suppress air entrainment [15]. In particular, its length determines where the wetting line is located with respect to the main body of the curtain flow. Depending on the relative speed of the substrate and curtain flow at its bottom, the wetting line can lie directly underneath the curtain or can be dragged forward (lower curtain flow and higher substrate speeds) or retarded backward (high curtain flow and lower substrate speed). This wetting line location determines whether the stagnation pressure from a tall liquid curtain is sufficient to suppress the

creation of an unstable air-bearing that leads to uneven and bubble-laden coatings. The highest coating speeds occur when the wetting line is located directly underneath the centerline of the curtain itself. The taller the liquid curtain, the faster the ultimate coating speed, provided that the wetting line location–again dictated by the Sakiadis boundary layer–is optimally controlled [15]. In addition to its relevance to coating, the Sakiadis boundary layer forms the basis for many studies including moving elastic sheets involving various modes of heat and mass transport[35–41]; in the past 5 years, the original Sakiadis paper [34] has been cited over 400 times which demonstrates its continued fundamental importance.

## IV.1 Newtonian Sakiadis boundary layer problem

### IV.1.1 Problem statement and formulation

The boundary layer surrounding a flat plate moving at a constant velocity through a viscous and Newtonian incompressible fluid was first examined in the literature by Sakiadis [34] who applied Blasius's similarity transform [42] to Prandtl's boundary layer equations. The result was a third order nonlinear ODE for $f(\eta)$, where $f$ and $\eta$ are similarity variables, related to physical variables in the boundary layer equation [34] through a similarity transform. Once boundary conditions were applied, the Newtonian Sakiadis Problem is written as

$$2f''' + ff'' = 0 \ , \ \ 0 \leq \eta < \infty \tag{IV.1a}$$

$$f = 0 \text{ at } \eta = 0, \tag{IV.1b}$$

$$\frac{df}{d\eta} = 1 \text{ at } \eta = 0, \tag{IV.1c}$$

$$\frac{df}{d\eta} = 0 \text{ as } \eta \to \infty. \tag{IV.1d}$$

### IV.1.2 A divergent power series solution

Although the main results of this section are found in previous work [1] (and references therein) for Newtonian fluid, we provide key results of that work here as they serve as essential background for our non-Newtonian analysis to follow. Following the approach taken for the Flat Wall and Cylindrical Wall Problems in respective Sections II.2 and III.2, we first directly obtain the power series solution to the nonlinear ODE (IV.1). The general solution form was first developed by Blasius [42] for flow over stationary wall, but here we adapt the solution for the moving wall boundary conditions in (IV.1), and obtain

$$f(\eta) = \sum_{n=0}^{\infty} a_n \eta^n \quad , \quad |\eta| < |\eta_s| \, , \tag{IV.2a}$$

where

$$a_{n+3} = \frac{-\sum_{j=0}^{n} (j+1)(j+2) a_{j+1} a_{n-j}}{2(n+1)(n+2)(n+3)} \quad , \quad n \geq 0, \tag{IV.2b}$$

with

$$a_0 = 0 \quad , \quad a_1 = 1 \text{ and } a_2 = \kappa/2. \tag{IV.2c}$$

In (IV.2a), $|\eta_s|$ is a finite radius of convergence, and in (IV.2c) the quantity $\kappa$, which its value is not yet known but can be determined later via the algorithm outlined in Section IV.1.5, is directly related to the wall shear stress in the boundary-layer flow, typically referred to as the "wall shear" parameter [43, 44], and is defined as

$$\kappa \equiv f''(0). \tag{IV.3}$$

Similar to the Flat Wall Problem and Cylindrical Wall Problem, the series (IV.2) diverges within the physical domain, as shown in figure 15a (dashed curves). Singularities that lie outside of the physical domain at a distance $\eta$ away from $\eta = 0$ are the cause this divergence. In [1], Barlow et al. showed that $\eta \approx 4.07217$, arising from singularities lying off the real-line in the left half-plane. This is shown by the vertical solid line in Figure 15a. Approximate resummations are available,

that bypass the original series' convergence barrier caused by these singularities for the Newtonian Sakiadis Problem [1, 11], and will be discussed in the next section.

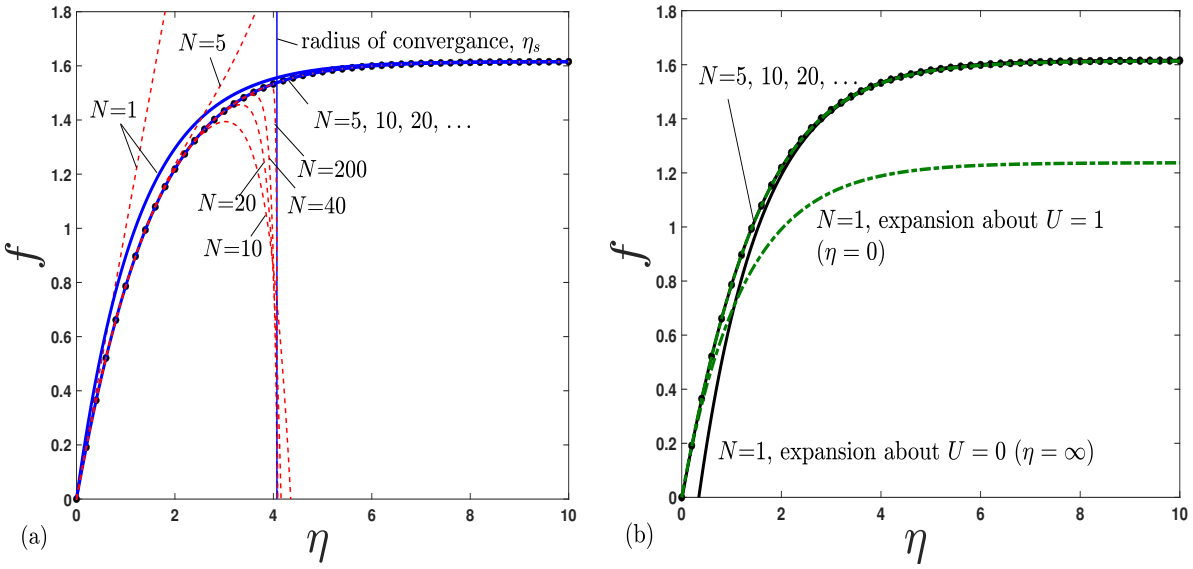


**Figure 15:** Analytic solutions of (IV.1) compared with the numerical solution (RK4 with $\Delta\eta = 10^{-5}$) (•'s). (a) $N$-term truncations of series (IV.2) (dashed curves) and approximant (IV.6) (solid curves). The vertical solid line indicates the radius of convergence $\eta_s$ of (IV.2). (b) $N$-term truncations of series (IV.14) (solid curves) and series (IV.16) (dashed curves).

### IV.1.3 Variable transform and a convergent power series solution

Similar to the approach taken in Sections II.3 and III.3, we consider the other side of the domain ($\eta \to \infty$) as a possible expansion point. Using the method of dominant balance [20], the $\eta \to \infty$ behavior for the Newtonian Sakiadis solution is given in [1] as

$$f \sim C + Ge^{-C\eta/2} + \frac{G^2}{4C}e^{-C\eta} + O\left(e^{-3C\eta/2}\right) \text{ as } \eta \to \infty, \tag{IV.4}$$

where $C$ and $G$ are asymptotic constants, yet to be determined, and by inspection

$$\lim_{\eta\to\infty} f(\eta) \equiv C. \tag{IV.5}$$

We note here that a similar exponential behavior is also observed in the Flat Wall Problem previously and provides a linkage between the two problems in approach and interpretation to follow. A particular sequence of approximants having the form of the asymptotic behavior (IV.4) is examined in [1] as

$$f_{A,N}(\eta) = C + \sum_{k=1}^{N} \bar{A}_k \left(e^{-C\eta/2}\right)^k, \tag{IV.6}$$

where the $\bar{A}_k \ldots \bar{A}_N$ coefficients are computed such that the expansion of (IV.6) about $\eta = 0$ exactly matches the Taylor series solution (IV.2b) to order $N$. Taylor expanding each term of (IV.6) to order $N$, switching the order of summation, and setting the result equal to (IV.2) leads to a $N \times N$ Vandermonde system, whose explicit inversion formula is known [45]. For example, at $N = 2$, we have

$$\begin{bmatrix} 1 & 1 \\ 1 & 2 \end{bmatrix} \begin{bmatrix} \bar{A}_1 \\ \bar{A}_2 \end{bmatrix} = \begin{bmatrix} 0!\, a_0 - C \\ 1!\, (-2/C)\, a_1 \end{bmatrix}, \tag{IV.7}$$

and for $N = 3$ we have

$$\begin{bmatrix} 1 & 1 & 1 \\ 1 & 2 & 3 \\ 1 & 4 & 9 \end{bmatrix} \begin{bmatrix} \bar{A}_1 \\ \bar{A}_2 \\ \bar{A}_3 \end{bmatrix} = \begin{bmatrix} 0!\, a_0 - C \\ 1!\, (-2/C)\, a_1 \\ 2!\, (-2/C)^2\, a_2 \end{bmatrix}, \tag{IV.8}$$

and so on. Note that, after inverting the matrices above, $\bar{A}_1$ and $\bar{A}_2$ attain different values in (IV.7) than in (IV.8). The relevance of this issue is discussed in what follows. Also, although the Vandermonde matrix has an explicit inversion formula, high precision arithmetic (i.e., beyond double) must be used for large $N$ to avoid round-off error.

All $\bar{A}_n$ coefficients change their value as $N$ changes, and thus (IV.6) does not have the properties of a formal power series solution to (IV.1). Nevertheless, $f_{\bar{A},N}$ converges to the numerical solution of $f$ over the physical domain as $N$ is increased; this is shown in Figure 15a (solid curves). Note that, although not remarked on in [1], each $\bar{A}_n$ coefficient in (IV.6) converges to a specific value as $N$ is increased. As explained in the Cylindrical Wall Problem, a necessary condition for an

expansion to converge is that it does not introduce new singularities into the problem that impose a radius smaller than the physical domain of interest. The expansion (IV.6) for the Newtonian Sakiadis problem does not have this issue, thus converges as shown in Figure 15a (solid curves). Additionally, (IV.6) was used in [1] to compute $\kappa$, as well as the asymptotic constants in (IV.4) ($C$ and $G$) to within 12 digits of accuracy (beyond previously reported numerical results) before hitting a round-off barrier.

Motivated by the asymptotic expansion (IV.4) and encouraged by the convergence of IV.6, we define the variable transformations

$$U(\eta) = e^{-C\eta/2}, \tag{IV.9a}$$

$$f(\eta) = R(U(\eta)), \tag{IV.9b}$$

with the goal of finding the Taylor coefficients of the function $R$ such that $R \circ U$ satisfies the ODE (IV.1). Substituting (IV.9a) and (IV.9b) into (IV.1a), applying the chain rule, and rearranging terms, leads to the transformed ODE

$$\frac{R}{C}\left(UR'' + R'\right) = U^2R''' + 3UR'' + R', \tag{IV.10}$$

where the primes denote the derivative with respect to $U$. The boundary conditions (IV.1b) - (IV.1d) become

$$R(1) = 0 \ , \ R'(1) = \frac{-2}{C} \ , \ R''(1) = \frac{2}{C} + \frac{4\kappa}{C^2}. \tag{IV.11}$$

In the usual way, we assume a solution to (IV.10) of the form

$$R(U) = \sum_{n=0}^{\infty} \tilde{A}_n U^n, \tag{IV.12}$$

which is readily differentiated term-by-term to compute $R'$, $R''$, and $R'''$. After employing Cauchy's product rule [17] (see Appendix A.2) to handle the nonlinear term on the left-hand side of (IV.10), the ODE becomes

$$\frac{U}{C}\sum_{n=0}^{\infty}\left[\sum_{k=0}^{n}(k+1)(k+2)\tilde{A}_{k+2}\tilde{A}_{n-k}\right]U^n+\frac{1}{C}\sum_{n=0}^{\infty}\left[\sum_{k=0}^{n}(k+1)\tilde{A}_{k+1}\tilde{A}_{n-k}\right]U^n$$
$$=U^2\sum_{n=0}^{\infty}(n+1)(n+2)(n+3)\tilde{A}_{n+3}U^n+3U\sum_{n=0}^{\infty}(n+1)(n+2)\tilde{A}_{n+2}U^n$$
$$+\sum_{n=0}^{\infty}(n+1)\tilde{A}_{n+1}U^n. \quad \text{(IV.13)}$$

Equating constant terms on both sides of (IV.13) leads to

$$\tilde{A}_0 = C. \quad \text{(IV.14a)}$$

Equating $U^1$ terms on both sides of (IV.13) leads to $\tilde{A}_1 = \tilde{A}_1$ and so we follow the convention of (IV.6) and (IV.4) such that

$$\tilde{A}_1 = G. \quad \text{(IV.14b)}$$

Equating $U^n$ terms for $n \geq 1$ on both sides of (IV.13) leads to

$$\sum_{k=0}^{n-1}(k+1)(k+2)\tilde{A}_{k+1}\tilde{A}_{n-k-1}+\sum_{k=0}^{n}(k+1)\tilde{A}_{k+1}\tilde{A}_{n-k}=C(n+1)^3\tilde{A}_{n+1},$$

which may be simplified (by appropriate shifts to the $k$ indices) as

$$\sum_{k=1}^{n+1}k^2\tilde{A}_k\tilde{A}_{n-k+1}=C(n+1)^3\tilde{A}_{n+1}.$$

Solving the above expression for $\tilde{A}_{n+1}$ and using (IV.14a) leads to the recursion

$$\tilde{A}_{n+1}=\frac{1}{Cn(n+1)^2}\sum_{k=1}^{n}k^2\tilde{A}_k\tilde{A}_{n-k+1}\ , \quad n\geq 1. \quad \text{(IV.14c)}$$

Note that for $n = 1$, (IV.14c) leads to

$$\tilde{A}_2=\frac{G^2}{4C},$$

which matches the asymptotic expansion (IV.4). The transformed solution to (IV.1), written in terms of the original variables is then

$$f(\eta)=\sum_{n=0}^{\infty}\tilde{A}_n\left(e^{-C\eta/2}\right)^n. \quad \text{(IV.14d)}$$

As we can see, (IV.14) is a Taylor series solution to (IV.1) in terms of the gauge function $e^{-C\eta/2}$. Although the implementation of (IV.14) requires knowledge of $C$ and $G$, we show in Section IV.1.5 that these may be computed (to any desired precision) directly from (IV.14) via the conditions (IV.11). Using values of $C$ and $G$ obtained in Section IV.1.5, convergence of (IV.14) is shown as solid curves in Figure 15b.

We now provide an explanation of why (IV.14) (and by extension (IV.6)) converge to the numerical solution of (IV.1). The singularities that cause the original series (IV.2) to diverge are now mapped via the gauge function (IV.9a) such that their influence lies beyond the physical domain; this is shown in Figure 16 where the complex $\eta$ and $U$ planes are compared. Here, we track the movement of the two singularities $\eta_{s,\pm}$ (shown by $*$'s in the figure) closest to $\eta = 0$, whose locations are predicted by the Padé analysis of [1]. In the $\eta$ plane of Figure 16, the circle of convergence for (IV.2) is drawn based on these two singularities. Note that this circle intersects the positive real line at the same location as the radius of convergence of series (IV.2) drawn in Figure 15a, as is expected from Taylor's theorem, which only guarantees convergence of Taylor series within such circles [46]. In the $U$ plane of Figure 16, the circle of convergence for (IV.14) is drawn, centered at $U = 0$ and with mapped radius $|e^{-(C\eta_{s,\pm})/2}|$; note that this circle now extends beyond the physical domain itself[2], which explains why (IV.14) converges over the entire physical domain.

[2]To paraphrase Buzz Lightyear: "To $\eta = \infty$ and beyond"

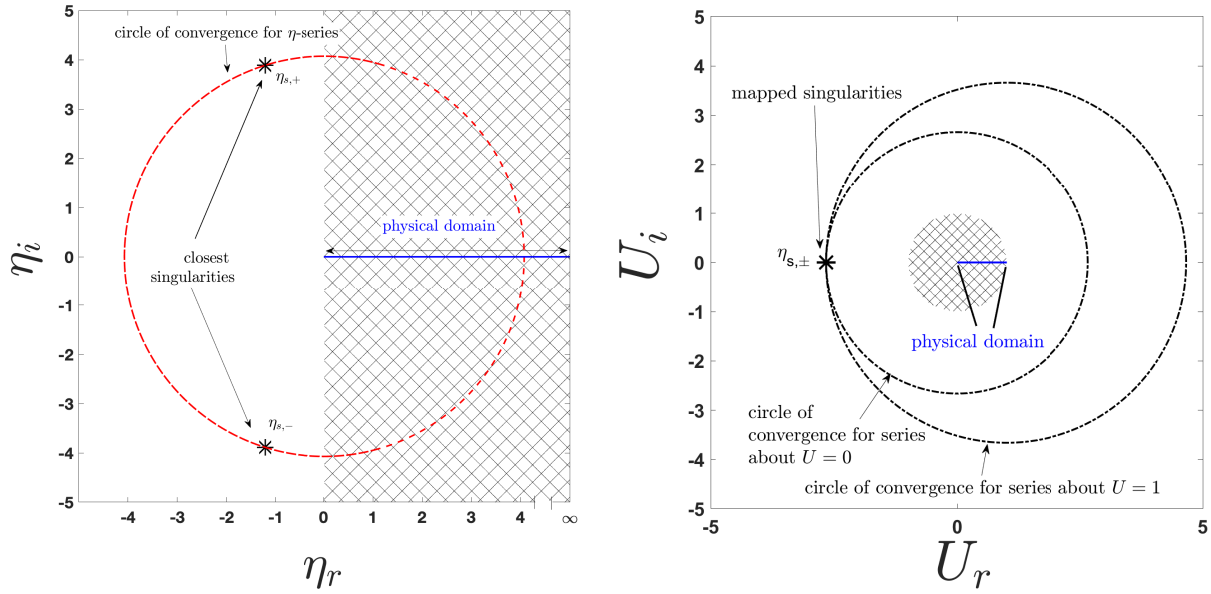


**Figure 16:** The effect of the gauge function transformation (IV.9) on $\eta$-singularities ($*$) of the Sakiadis function, showing their placement in the 2nd and 3rd quadrants of the complex $\eta$ plane (left) and their image on the negative real $U$ line (right). The interior of the dashed circle shown in the $\eta$ plane delineates the region of convergence of series (IV.2). The interiors of the smaller and larger dashed circles shown in the $U$ plane respectively delineate the regions of convergence of (IV.14) and (IV.16).

On the mapped $U$-plane shown in Figure 16, note that, in addition to drawing the circle of convergence corresponding to expansion (IV.14), a larger circle corresponding to the expansion about $U = 1$ is also drawn, which is larger because the mapped singularities are farther away. This expansion point corresponds to $\eta = 0$ in the original domain. Using the same procedures employed above to obtain the series about $U = 0$, the series about $U = 1$ is defined as

$$R(U) = \sum_{n=0}^{\infty} \hat{A}_n (U-1)^n \tag{IV.15}$$

where the coefficients are given as

$$\hat{A}_{n+3} = -\frac{2n+3}{n+3}\hat{A}_{n+2} - \frac{(n+1)^2}{(n+2)(n+3)}\hat{A}_{n+1} + \frac{\sum_{k=0}^{n-2}(k+1)(k+2)\hat{A}_{k+2}\hat{A}_{n-k-1} + \sum_{k=0}^{n-1}(k+1)\left[(k+2)\hat{A}_{k+2} + \hat{A}_{k+1}\right]\hat{A}_{n-k}}{C(n+1)(n+2)(n+3)}, \; n \geq 0 \tag{IV.16a}$$

$$\hat{A}_0 = 0 \;\; , \;\; \hat{A}_1 = -2/C \;\; , \;\; \hat{A}_2 = \frac{2\kappa}{C^2} + \frac{1}{C}, \tag{IV.16b}$$

and, writing (IV.15) in terms of the original variables, we have

$$f(\eta) = \sum_{n=0}^{\infty} \hat{A}_n \left(e^{-C\eta/2} - 1\right)^n, \tag{IV.16c}$$

which may be considered a series solution to (IV.1) written in terms of the gauge function $\left(e^{-C\eta/2} - 1\right)$. Using values of $C$ and $G$ obtained in Section IV.1.5, convergence of (IV.16) is shown as dashed curves in Figure 15b.

### IV.1.4 Convergent power series solution results

Although it is difficult to identify an advantage in using (IV.16) over (IV.14), as each naturally perform better near their expansion point as they converge (see Figure 15b), a "best choice" can be chosen by examining the rapidity of convergence. This can be determined by considering the infinity norm of the error (over $U \in [0,1]$) versus truncation $N$, shown in Figure 17. In the figure, one can see that, for a fixed number of terms $N$, the expansion about $U = 1$ (given by (IV.16)) is more accurate than that about $U = 0$ (given by (IV.14)); this means it takes less terms with (IV.16) to achieve a desired accuracy. For comparison, the approximant (IV.6) is also shown in Figure 17 and outperforms both (IV.14) and (IV.16). The cost in using (IV.6) is computational, since either inverting an increasingly ill-conditioned Vandermonde matrix or using a Vandermonde inversion algorithm requires precision well-beyond double to avoid round-off error.

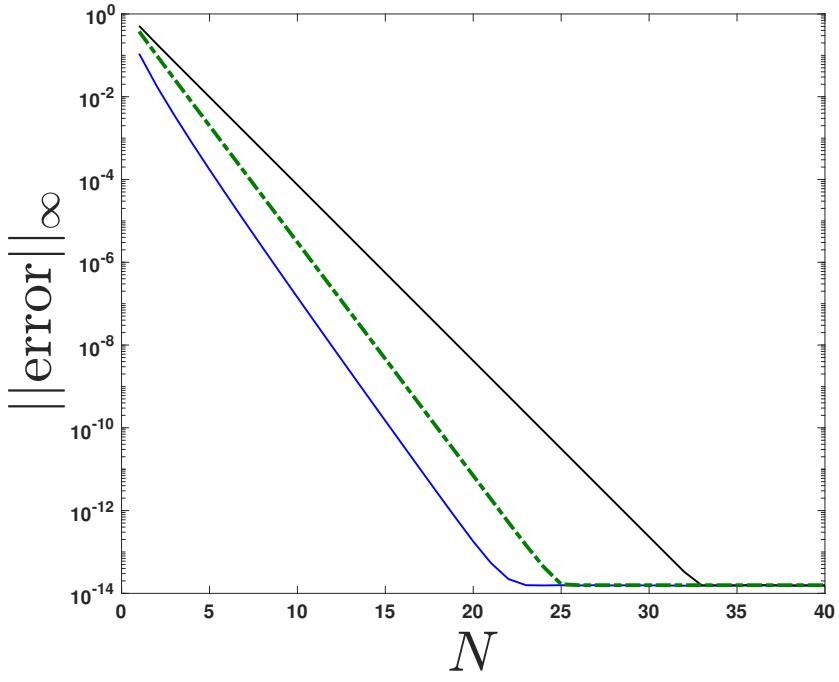


**Figure 17:** The infinity norm of the difference between convergent analytical solutions and the numerical solution to (IV.1), taken over the domain $U \in [0, 1]$ and plotted versus series truncation $N$. The legend is the same as in Figure 15, showing (IV.6) series (lowermost solid curve), series (IV.16) (middle dashed curve), and series (IV.14) (uppermost solid curve). The trends shown here are the same for the norm of the error of $f'$ and $f''$ using (IV.6), (IV.16), and (IV.14).

### IV.1.5 Computation of C, G, and $\kappa$

Previous estimates for $C$, $G$, and $\kappa$ have been found by quadrature, shooting, and approximant (IV.6) [1, 43, 47]. Here, we improve upon those estimates and provide formulae for obtaining them to any desired precision, by considering the application of conditions (IV.11) to the convergent

solution (IV.14), i.e.,

$$R(1) = \sum_{n=0}^{\infty} \tilde{A}_n = 0 \tag{IV.17}$$

$$R'(1) = \sum_{n=1}^{\infty} n\tilde{A}_n = \frac{-2}{C} \tag{IV.18}$$

$$R''(1) = \sum_{n=2}^{\infty} n(n-1)\tilde{A}_n = \frac{2}{C} + \frac{4\kappa}{C^2}. \tag{IV.19}$$

Noting that (IV.17) and (IV.18) are functions of $C$ and $G$ only (see (IV.14)), we have 2 equations and 2 unknowns and one may employ any desired solver (here we use Newton's method). After finding $C$ and $G$, one may then use (IV.19) to explicitly compute $\kappa$. In preparation for Newton's method, we rewrite (IV.17) and (IV.18) as

$$\phi_0(C, G) = \sum_{n=0}^{\infty} \tilde{A}_n = 0 \tag{IV.20}$$

$$\phi_1(C, G) = \frac{2}{C} + \sum_{n=1}^{\infty} n\tilde{A}_n = 0, \tag{IV.21}$$

such that the $\nu^{\text{th}}$ Newton iterate becomes

$$\begin{bmatrix} C_{\nu+1} \\ G_{\nu+1} \end{bmatrix} = \begin{bmatrix} C_\nu \\ G_\nu \end{bmatrix} - \begin{bmatrix} \left(\frac{\partial \phi_0}{\partial C}\right)_\nu & \left(\frac{\partial \phi_0}{\partial G}\right)_\nu \\ \left(\frac{\partial \phi_1}{\partial C}\right)_\nu & \left(\frac{\partial \phi_1}{\partial G}\right)_\nu \end{bmatrix}^{-1} \begin{bmatrix} \phi_{0,\nu} \\ \phi_{1,\nu} \end{bmatrix}. \tag{IV.22a}$$

The partial derivatives in (IV.22a) may be computed compactly by recognizing the pattern in the series (IV.14) as

$$R = C + GU + \frac{1}{4}\frac{G^2}{C}U^2 + \frac{5}{72}\frac{G^3}{C^2}U^3 + \cdots + \underbrace{a'_n G^n C^{1-n}}_{\tilde{A}_n} U^n + \ldots,$$

where $a'_n$ is $\tilde{A}_n$ evaluated at $C = G = 1$ (i.e., the coefficient with $C$ and $G$ removed)[3]. Using the dependence shown above, the partial derivatives needed for (IV.22a) are found[4] by first partially

[3]Although here we claim this form of $C$ and $G$ dependence on $\tilde{A}_n$ by inspection, this can be verified by making the substitutions $U = C\tilde{U}/G$ and $R = C\tilde{R}$ into (IV.10) and noting the $C$ and $G$ dependence vanishes.

[4]In cases where the parameter dependence is more complicated, this can always be done recursively by directly partially differentiating the recurrence relation. Such a procedure was employed in Chapter III for the Cylindrical Wall Problem.

differentiating each coefficient with respect to $G$ or $C$, noting that $a'_n$ is a constant, and multiplying and dividing by $G$ or $C$ to make the expression in terms of $\tilde{A}_n$. Thus we obtain

$$\frac{\partial \phi_0}{\partial C} = \frac{1}{C}\sum_{n=0}^{\infty}(1-n)\tilde{A}_n \qquad \frac{\partial \phi_0}{\partial G} = \frac{1}{G}\sum_{n=0}^{\infty} n\tilde{A}_n$$
$$\frac{\partial \phi_1}{\partial C} = \frac{-2}{C^2} + \frac{1}{C}\sum_{n=1}^{\infty} n(1-n)\tilde{A}_n \qquad \frac{\partial \phi_1}{\partial G} = \frac{1}{G}\sum_{n=1}^{\infty} n^2\tilde{A}_n. \tag{IV.22b}$$

Using the method outlined above, the following improved estimates are obtained beyond double precision using only a few Newton iterations (if previous estimates are used as the initial guess) in (IV.22) and a truncation of 50 terms in the series of (IV.22b):

$$C = 1.616125446804603717\ldots$$

$$G = -2.1313459240475714821\ldots$$

Using the above values of $C$ and $G$, we add the left and right side of (IV.18) and (IV.19), extract $\tilde{A}_1 = G$ from (IV.18), and compute $\kappa$ as

$$\kappa = \frac{C^2}{4}\left[G + \sum_{n=2}^{\infty} n^2\tilde{A}_n\right], \tag{IV.23}$$

where, taking 50 terms in (IV.23), we obtain

$$\kappa = -0.443748313368861\ldots$$

#### IV.1.6 Summary: The Newtonian Sakiadis Problem

The above shows that we can construct convergent power series solutions to the Newtonian Sakiadis boundary layer problem by choosing an independent variable motivated by the form of the asymptotic expansion at infinity. Similar to the Flat Wall Problem, an exponential transformation maps the convergence-limiting singularities out of the physical domain. In contrast with the Newtonian Sakiadis Problem, the Flat Wall Problem has an exact solution that allows us to anticipate the location of convergence-limiting singularity *a priori*. Still, the Newtonian

Sakiadis Problem shows that precise knowledge of this singularity is not required to obtain a convergent expansion. That said, for both the Newtonian Sakiadis Problem and Flat Wall Problem, the exponential gauge functions used handle singularities similarly to achieve demonstrably convergent series solutions. We next consider to extend these learnings to the non-Newtonian extension of Sakiadis problem.

## IV.2 Non-Newtonian Sakiadis boundary layer problem

### IV.2.1 Problem statement and formulation

Figure 18 shows the configuration of the Sakiadis boundary layer problem with the $x$-$y$ coordinate system as indicated; the fluid flow is assumed to be invariant with the direction oriented out of the figure. Here, a flat wall is moving with velocity, $u_w$, through an otherwise stationary generalized Newtonian incompressible fluid of density, $\rho$, and shear-dependent viscosity, $\mu$.

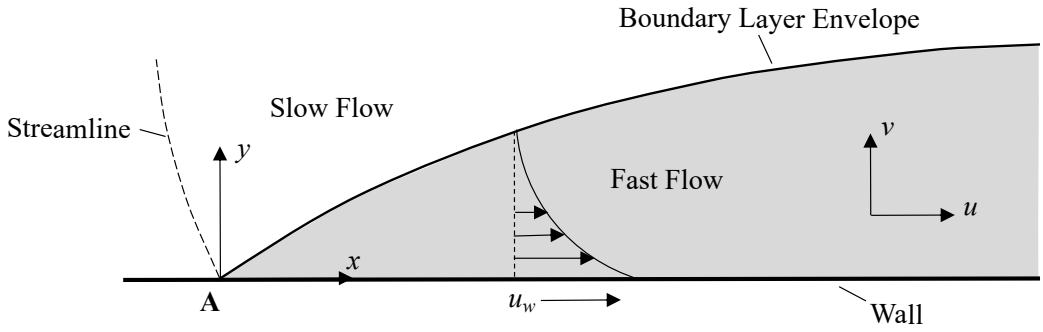


**Figure 18:** Schematic of the Sakiadis boundary layer flow. Slowly moving or otherwise stationary fluid with characteristic velocity scale $S$ is in contact with a fast moving wall having speed of $u_w$ as indicated, where $S << u_w$. As a result, the velocity $u \to 0$ as $y \to \infty$ in the boundary layer approximation to the flow equations. The boundary layer envelope is defined in this paper as the locus of points for which $u/u_w = 0.1$. In the original papers of Sakiadis [34] and Fox et al. [48], fluid enters the domain at point **A** through a slit, where the streamline is redrawn to be vertical and coincident with a wall. In coating applications, the streamline often aligns with an interface where point **A** is a moving contact line [14].

The governing equations embody conservation of mass and momentum through the two dimensional incompressible steady state continuity and Navier-Stokes equations. At high substrate speeds, velocity in the $x$-direction, $u$, is much larger than that in the $y$-direction, $v$, and velocity gradients in the $y$-direction dominate viscous forces in the boundary layer. These assumptions, which result in a small slope of fluid points, lead directly to Prandtl's boundary layer equations—a nonlinear partial differential equation (PDE) system—that apply to the Sakiadis flow. For fluids having a viscosity that satisfies the Ostwald-de Waele power law dependence, the Sakiadis boundary layer equations are expressed as [48]

$$\frac{\partial u}{\partial x} + \frac{\partial v}{\partial y} = 0, \tag{IV.24a}$$

$$u\frac{\partial u}{\partial x} + v\frac{\partial u}{\partial y} = \frac{1}{\rho}\frac{\partial \tau_{xy}}{\partial y}, \tag{IV.24b}$$

$$\tau_{xy} = \mu\left(\frac{\partial u}{\partial y}\right)\ ,\ \mu = K\left(-\frac{\partial u}{\partial y}\right)^{\alpha-1}, \tag{IV.24c}$$

$$u = u_w,\ v = 0 \text{ at } y = 0\ ;\ u \to 0 \text{ as } y \to \infty. \tag{IV.24d}$$

In (IV.24c), $\tau_{xy}$ is the shear stress in the fluid, $K > 0$ is the consistency coefficient, $\alpha$ is the power law exponent, and $\mu$ is the strain-rate dependent viscosity. Note that the rate of strain in the boundary layer approximation, $\partial u/\partial y$, is negative in the flow domain; thus, the magnitude of the rate of strain invokes a negative sign as indicated in the viscosity expression in (IV.24c). Through the use of the stream function, $\psi$, that satisfies the continuity equation (IV.24a) (i.e., $u = \partial\psi/\partial y$ and $v = -\partial\psi/\partial x$), Fox et al. [48] define similarity variables given as

$$\eta = y\left(\frac{\rho u_w^{2-\alpha}}{Kx}\right)^{1/(\alpha+1)}, \tag{IV.25a}$$

$$\psi = \left(\frac{y\ u_w}{\eta}\right) f(\eta), \tag{IV.25b}$$

and thus $u$ and $v$ are expressed as

$$u = u_w\frac{df}{d\eta}\ ,\ \ v = \frac{1}{1+\alpha}\left(\frac{Ku_w^{2\alpha-1}}{\rho x\alpha}\right)^{\frac{1}{\alpha+1}}\left(\eta\frac{df}{d\eta} - f\right). \tag{IV.26}$$

Upon substitution of (IV.25) into the system (IV.24) and after rearrangement, Fox et al. [48] obtain the non-Newtonian Sakiadis boundary layer problem given as

$$\alpha(\alpha+1)\frac{d^3f}{d\eta^3} - f(-\frac{d^2f}{d\eta^2})^{(2-\alpha)} = 0, \quad 0 \le \eta < \infty, \tag{IV.27a}$$

$$f = 0 \text{ at } \eta = 0, \tag{IV.27b}$$

$$\frac{df}{d\eta} = 1 \text{ at } \eta = 0, \tag{IV.27c}$$

$$\frac{df}{d\eta} = 0 \text{ as } \eta \to \infty. \tag{IV.27d}$$

Note that $\alpha = 1$ in (IV.27a) corresponds to a Newtonian fluid and thus reduced to (IV.1a) as a special case.

### IV.2.2 A divergent power series solution

A power series solution to the ODE (IV.27) can be obtained through standard means using JCP Miller's formula [18] and Cauchy's product rule [17] (see Appendixes A.1 and A.2, respectively) to re-order nonlinear terms in powers of $\eta$; the series expansion is

$$f = \sum_{n=0}^{\infty} a_n \eta^n, \quad |\eta| < \eta_s(\alpha), \tag{IV.28a}$$

$$a_{n+3} = \frac{\sum_{j=0}^{n} b_j \, a_{n-j}}{\alpha(\alpha+1)(n+3)(n+2)(n+1)}, \quad n \geq 0, \tag{IV.28b}$$

$$b_{n>0} = \frac{1}{2n a_2} \sum_{j=1}^{n} (3j - \alpha j - n)(j+2)(j+1) a_{j+2} b_{n-j} \quad , \quad b_0 = (-2a_2)^{2-\alpha}, \tag{IV.28c}$$

$$a_0 = 0 \quad , \quad a_1 = 1 \quad , \quad \text{and } a_2 = \kappa/2, \tag{IV.28d}$$

where $\eta_s(\alpha)$ is a finite radius of convergence. In (IV.28d), the quantity $\kappa$ is the "wall shear" parameter in the boundary-layer problem [43, 44], and is defined in (IV.3) (see Section IV.1.2). The quantity $\kappa$ (IV.3) in Non-Newtonian Sakiadis Problem is a function of $\alpha$, and is not known a priori; it is typically determined numerically. Alternatively, $\kappa$ can be calculated algorithmically as shown in Section IV.2.3.3, as an extension of the technique developed for the Newtonian Sakiadis Problem (see Section IV.1.5).

Figure 19 provides a comparison between the power series solution (IV.28) and the numerical solution to (IV.27) for $\alpha = 0.8$. The numerical solution is obtained using a shooting method (see Appendix C.1) to recast system (IV.27) as a boundary value problem on a finite domain length $L$, where the condition (IV.27d) is replaced with $df/d\eta = 0$ at $\eta = L$; the length $L$ is chosen such that doubling its size leads to difference in the predictions of $\kappa$ and $C = f(L)$ of $O(10^{-15})$ and $O(10^{-10})$ when $\alpha = 0.8$. The constants $\kappa$ and $C$ are defined in (IV.3) and (IV.5), respectively. As shown in the Figure 19, the power series solution (IV.28) diverges within the physical domain. The rightmost vertical line marked by arrow $A$ shows the radius of convergence of the power series

solution (IV.28) given by $\eta_s(0.8) \approx 3.09$ , which is confirmed via a numerical root test [5], as shown in Figure 20.

[5]Some of the coefficients $a_n$ in (IV.28) are zero; hence, we use root test instead of ratio test.

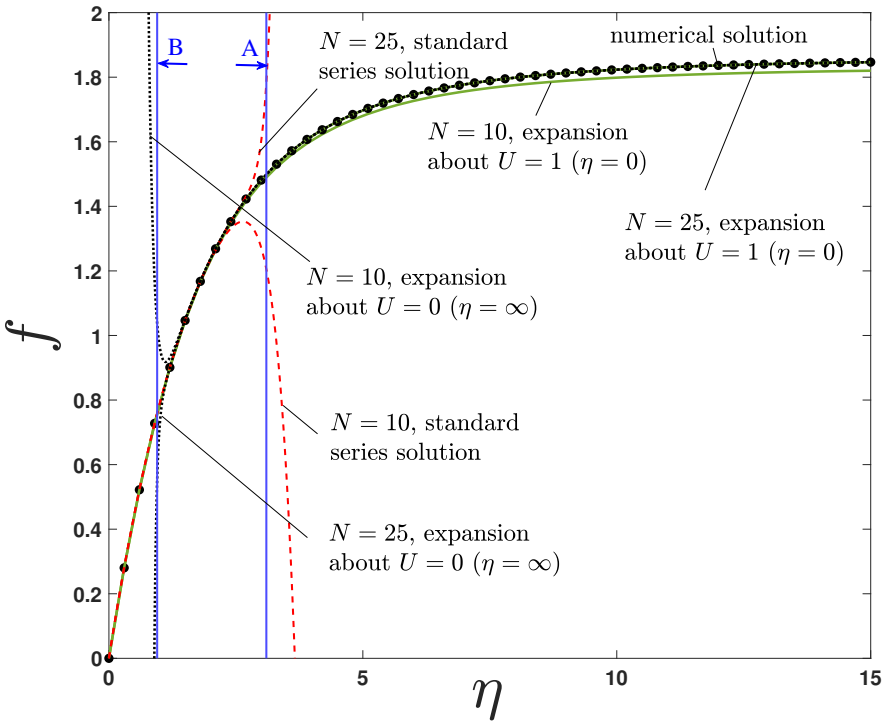


**Figure 19:** The solution to (IV.27) is shown for $\alpha = 0.8$. The numerical solution (Appendix C.1) with $L = 11000$ (black dots) is compared against the $N$-term truncations of the power series solution (IV.28) (dashed curves), transformed series solution (expansion about $\eta = \infty$) (IV.35) (dotted curves), and the transformed series solution (expansion about $\eta = 0$) (IV.37) (solid curves) for $N = 10$ and $N = 25$. In regions of the plot where a given dashed or dotted curve is not clearly seen, the curves agree with the numerical results. The rightmost vertical line (marked by arrow A) shows the radius of convergence $\eta_s \approx 3.09$ of the standard series solution (IV.28), and the leftmost vertical line (marked by arrow B) shows the radius of convergence $\eta_s \approx 0.95$ of the transformed series solution (IV.35). For $\alpha = 0.8$, the numerically obtained values of the constants $\kappa$, $C$, and $E$ (defined in SectionIV.2.3) used in producing the figure are given in Appendix C.2.2.

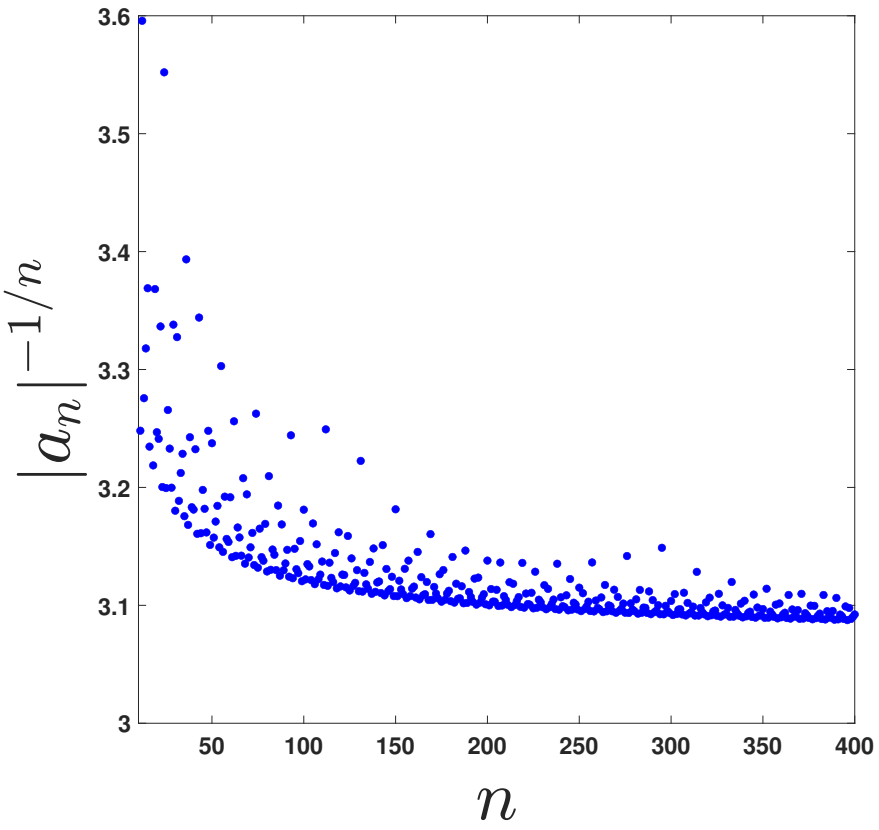


**Figure 20:** Root test for (IV.28) is shown for $\alpha = 0.8$, indicating a radius of convergence ($y$-axis) of $\eta_s \approx 3.09$. This is consistent with the divergent behavior observed in Figure 19.

### IV.2.3 Asymptotically motivated gauge function and expansions

#### IV.2.3.1 Asymptotic behavior as $\eta \to \infty$

Similar to the approach taken for Newtonian fluids [11] in Section IV.1.3, we use the method of dominant balance [20] to determine the asymptotic behavior of $f$ as $\eta \to \infty$. This behavior motivates the use of a gauge function that ultimately leads to a convergent series expansion. To proceed, we write the solution of (IV.27a) as

$$f \sim C + h(\eta), \text{ with } h \to 0 \text{ as } \eta \to \infty, \tag{IV.29a}$$

where $C$ is the asymptotic constant described in (IV.5), and $h(\eta)$ is a function to be determined. The form (IV.29a) is substituted in (IV.27a) to obtain

$$\alpha(\alpha+1)h''' \sim (C+h)(-h'')^{(2-\alpha)} \text{ as } \eta \to \infty, \tag{IV.29b}$$

where the primes denote derivatives of $h$ with respect to $\eta$. Equation (IV.29b) may be simplified by noting that $h$ is subdominant to $C$ as $\eta \to \infty$, and thus

$$\alpha(\alpha+1)h''' \sim C(-h'')^{(2-\alpha)} \text{ as } \eta \to \infty. \tag{IV.29c}$$

The above equation can be integrated once to obtain

$$h'' \sim -\left[E + \frac{C(1-\alpha)}{\alpha(\alpha+1)}\eta\right]^{\frac{1}{\alpha-1}} \text{ as } \eta \to \infty, \tag{IV.29d}$$

where $E$ is the constant of integration to be determined. Integrating (IV.29d) twice, and applying the boundary condition (IV.27d), the solution of (IV.29d) is

$$h \sim \frac{\alpha(\alpha+1)^2 E^{\frac{2\alpha-1}{\alpha-1}}}{-C^2(2\alpha-1)}\left[1 + \frac{C(1-\alpha)}{\alpha(\alpha+1)E}\eta\right]^{\frac{2\alpha-1}{\alpha-1}} , \ 0.5 < \alpha < 1 \text{ , as } \eta \to \infty, \tag{IV.29e}$$

and thus from (IV.29e), we obtain

$$f \sim C + \frac{\alpha(\alpha+1)^2 E^{\frac{2\alpha-1}{\alpha-1}}}{-C^2(2\alpha-1)}\left[1 + \frac{C(1-\alpha)}{\alpha(\alpha+1)E}\eta\right]^{\frac{2\alpha-1}{\alpha-1}} , \ 0.5 < \alpha < 1 \text{ , as } \eta \to \infty. \tag{IV.29f}$$

By inspection, we see that (IV.29f) approaches $C$ as $\eta \to \infty$ only when $0.5 < \alpha < 1$, and thus condition (IV.27d) can only be satisfied in this range. Consequently, system (IV.27) is only valid for $0.5 < \alpha \leq 1$ ($\alpha = 1$ for Newtonian fluids). Note that Fox et al. [48] incorrectly indicate that the solution to system (IV.27) exists when $0 < \alpha < 0.5$. Additionally, although such solutions may be obtained to the finite-domain approximation to system (IV.27) where (IV.27d) is replaced with $f'(L) = 0$, these solutions do not converge to an infinite domain solution as $L \to \infty$; note that Pop et al. [49] incorrectly claim that the solution exists for $\alpha > 1$.

#### IV.2.3.2 Construction of a convergent power series solution

To overcome the convergence limitation of the power series solution (IV.28), we follow the approach used for Newtonian Sakiadis Problem (see Section IV.1.3). Here, we propose the following variable

transformation, inspired by the asymptotic expansion (IV.29f), whose utility is validated in what follows. We write

$$U(\eta) = [1 + \mathcal{A}\eta]^{\lambda}, \tag{IV.30a}$$

$$f(\eta) = F(U(\eta)), \tag{IV.30b}$$

$$\mathcal{A} = \frac{C(1-\alpha)}{\alpha(\alpha+1)E} \quad , \quad \lambda = \frac{2\alpha - 1}{\alpha - 1}. \tag{IV.30c}$$

The transformation (IV.30) maps $\eta \in [0, \infty)$ to $U \in (0, 1]$ when $0.5 < \alpha < 1$.

It is worth noting that the non-Newtonian transformation in (IV.30a), reduces to the Newtonian transformation given by (IV.9), as $\alpha \to 1$, since

$$\lim_{\alpha \to 1} [1 + \mathcal{A}\eta]^{\lambda} = e^{-C\eta/2E}, \tag{IV.31}$$

when $E = 1$; we have indeed verified numerically that $E \to 1$ as $\alpha \to 1$ (see Table 2 in Appendix C.2.1). Substituting (IV.30) into (IV.27a), applying the chain rule, and rearranging terms, we obtain the transformed ODE

$$k_1 U^{\left(3-\frac{3}{\lambda}\right)} F''' + k_2 U^{\left(2-\frac{3}{\lambda}\right)} F'' + k_3 U^{\left(1-\frac{3}{\lambda}\right)} F' - \left\{ k_4 U^{\left(2-\frac{2}{\lambda}\right)} F'' + k_5 U^{\left(1-\frac{2}{\lambda}\right)} F' \right\}^{2-\alpha} F = 0,$$

where the primes denote derivatives of $F$ with respect to $U$. After multiplying the above by $U^{\left(\frac{3}{\lambda}-1\right)}$, and rearranging the ODE such that the highest derivative is on the left side of the equation, we obtain

$$k_1 U^2 F''' = -k_2 U F'' - k_3 F' + \left\{ k_4 U F'' + k_5 F' \right\}^{2-\alpha} F, \tag{IV.32a}$$

where

$$k_1 = \alpha(\alpha+1)\mathcal{A}^3\lambda^3, \tag{IV.32b}$$

$$k_2 = 3\alpha(\alpha+1)\mathcal{A}^3\lambda^2(\lambda-1), \tag{IV.32c}$$

$$k_3 = 3\alpha(\alpha+1)\mathcal{A}^3\lambda(\lambda-1)(\lambda-2), \tag{IV.32d}$$

$$k_4 = -\mathcal{A}^2\lambda^2, \tag{IV.32e}$$

$$k_5 = -\mathcal{A}^2\lambda(\lambda-1), \tag{IV.32f}$$

and the expressions for $\mathcal{A}$ and $\lambda$ are defined in (IV.30c). The boundary conditions at $\eta = 0$ from (IV.27b) and (IV.27c), corresponding to $U = 1$, become

$$F(1) = 0, \tag{IV.32g}$$

$$F'(1) = \frac{1}{\mathcal{A}\lambda}, \tag{IV.32h}$$

$$F''(1) = \frac{\kappa}{\mathcal{A}^2\lambda^2} - \frac{\lambda - 1}{\mathcal{A}\lambda^2}, \tag{IV.32i}$$

where the boundary condition (IV.3) is used to obtain $F''(1)$ in (IV.32i).

We next assume a solution to (IV.32a) of the form

$$F(U) = \sum_{n=0}^{\infty} A_n U^n, \ |U| < U_s(\alpha) \ , \ E > 0, \tag{IV.33}$$

where $U_s(\alpha)$ is the radius of convergence. The $E > 0$ restriction allows for the use of (IV.29) without introducing branch point singularities into the $U$ domain of interest. Series (IV.33) is readily differentiated term-by-term to compute $F'$, $F''$, and $F'''$. After employing JCP Miller's formula [18] and Cauchy's product rule [17] (see Appendixes A.1 and A.2, respectively) to re-order the nonlinear terms in (IV.32a), the ODE in (IV.32a) becomes

$$\sum_{n=2}^{\infty} k_1(n+1)n(n-1)A_{n+1}U^n = (-k_3A_1 + A_0d_0) + (-2k_2A_2 - 2k_3A_2 + A_0d_1 + A_1d_0)U +$$
$$\sum_{n=2}^{\infty} \left( -k_2(n+1)nA_{n+1} - K_3(n+1) + A_0\tilde{d}_n + \frac{(2-\alpha)A_0d_0}{c_0}(n+1)(k_4n + k5)A_{n+1} + \tilde{e}_n \right) U^n, \tag{IV.34}$$

where

$$\tilde{d}_n = \frac{1}{nc_0}\sum_{j=1}^{n-1}(3j - \alpha j - n)c_jd_{n-j} \ \ , \ \ \tilde{e}_n = \sum_{j=1}^{n} A_jd_{n-j}, \tag{IV.35a}$$

$$d_{n>0} = \frac{1}{nc_0}\sum_{j=1}^{n}(3j - \alpha j - n)c_jd_{n-j} \ \ , \ \ d_0 = (c_0)^{(2-\alpha)}, \tag{IV.35b}$$

$$c_{n>0} = (n+1)A_{n+1}(k_4n + k_5) \ \ , \ \ c_0 = k_5A_1. \tag{IV.35c}$$

Using the asymptotic solution (IV.29f), we enforce

$$A_0 = C. \tag{IV.35d}$$

Equating constant terms on both sides of (IV.34) leads to

$$A_1 = \left[\frac{k_3}{A_0(k_5)^{2-\alpha}}\right]^{\frac{1}{1-\alpha}}, \tag{IV.35e}$$

and equating $U^1$ terms on both sides of (IV.34) leads to

$$A_2 = \frac{A_1 d_0}{2k_2 + 2k_3 - \frac{2(2-\alpha)A_0 d_0}{c_0}(n+1)(k_4 n + k5)}. \tag{IV.35f}$$

We equate like-terms in (IV.34) to obtain the coefficients $A_{n+1}$, and for $n \geq 2$, we obtain the recurrence relation

$$A_{n+1} = \frac{A_0 \tilde{d}_n + \tilde{e}_n}{K_1(n+1)n(n-1) + k_2(n+1)n + k_3(n+1) - \frac{(2-\alpha)A_0 d_0}{c_0}(n+1)(k_4 n + k5)}, \; n \geq 2, \tag{IV.35g}$$

where $\tilde{d}_n$ and $\tilde{e}_n$ are defined in (IV.35a). Transforming back to $f(\eta)$ space via (IV.30), our expansion about $U = 0$ (i.e. $\eta = \infty$) is

$$f(\eta) = \sum_{n=1}^{\infty} A_n \left[1 + \mathcal{A}\eta\right]^{\lambda n}. \tag{IV.35h}$$

Here we explicitly see that variable transformation $U$ in (IV.30) naturally invokes the appropriate and nontrivial gauge function $[1 + \mathcal{A}\eta]^{\lambda}$. Although our ultimate goal is to have a self-contained solution that is not dependent on numerically determined parameters, at this stage we use the numerical values of $\kappa$, $C$, and $E$ in (IV.35) (see Table 3 in Appendix C.2.2) to assess the efficacy of (IV.35). To determine the numerical value of $E$, we solve (IV.29d) for $E$ as

$$E = (-h'')^{\alpha-1} - \frac{C(1-\alpha)}{\alpha(\alpha+1)}\eta \;\text{ as } \eta \to \infty, \tag{IV.36}$$

where the $\eta \to \infty$ condition is approximated in a numerical solution (of domain length $L$) by replacing $\eta$ with $L$, $C$ with $h(L)$, and $h''$ with $h''(L)$. Figure 19 shows that the transformed series solution (IV.35) (dotted curves) matches the numerical solution as $\eta \to \infty$, and the standard power series solution (IV.28) (dashed curves) matches the numerical solution as $\eta \to 0$, as expected. It is apparent here that the power series solution (IV.35) diverges as $\eta \to 0$. Since the coefficients

of (IV.35) alternate in sign, the closest singularity lies along the negative real $U$ axis [25], i.e. outside the physical domain. The vertical solid line (marked by arrow B) in Figure 19 shows the radius of convergence of the series solution (IV.35). This radius is confirmed via a numerical ratio test in the form of a Domb-Skyes plot [25], shown in Figure 20 as a plot of the relevant coefficient ratio vs. $1/n$. As the curve is linear in $1/n$ for large $n$, the radius of convergence is identified as the $y$-intercept.

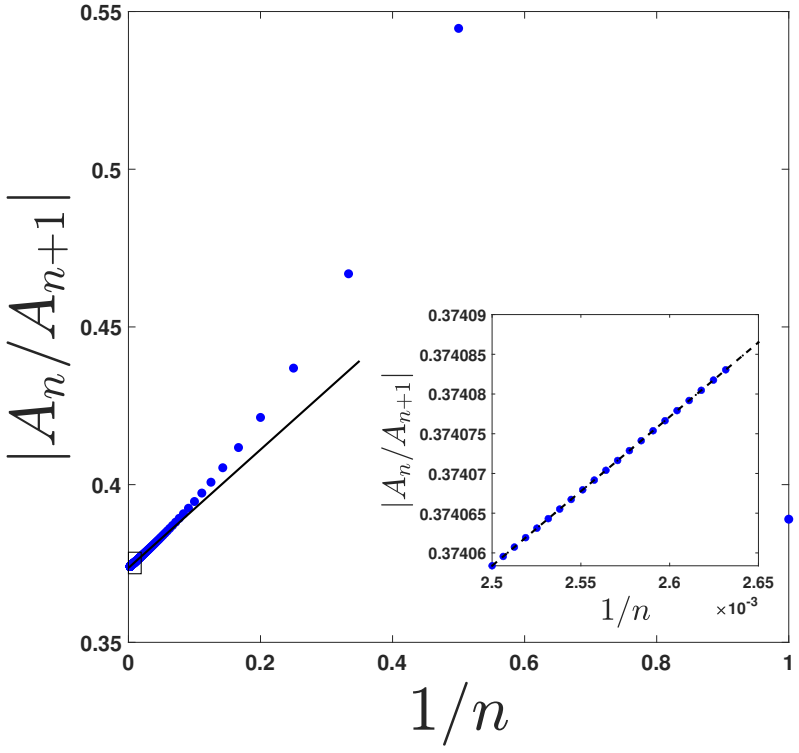


**Figure 21:** Domb-Sykes plot for (IV.35) with $\alpha = 0.8$, Here, the intercept for $1/n = 0$ yields the numerical radius of convergence ($y$-axis) $U_s \approx 0.37$, in agreement with a radius of convergence in the original domain $\eta_s \approx 0.95$ through (IV.30a). This is consistent with the divergent behavior observed in Figure 19.

In Section IV.1.3, we showed that the radius of convergence for the Newtonian Sakiadis Problem can be increased by changing the expansion point of the power series solution to the transformed

ODE [11]. Inspired from that work, we change the expansion point in the power series solution to (IV.32) to $U = 1$, corresponding to $\eta = 0$. Using the same procedures employed above to obtain the series about $U = 0$, the series about $U = 1$ is defined as

$$F(U) = \sum_{n=0}^{\infty} \hat{A}_n (U-1)^n, \; E > 0, \tag{IV.37a}$$

where

$$\hat{A}_0 = 0, \tag{IV.37b}$$

$$\hat{A}_1 = \frac{1}{\mathcal{A}\lambda}, \tag{IV.37c}$$

$$\hat{A}_2 = \frac{1}{2}\left(\frac{\kappa}{\mathcal{A}^2\lambda^2} - \frac{\lambda - 1}{\mathcal{A}\lambda^2}\right), \tag{IV.37d}$$

$$\hat{A}_3 = \frac{1}{6k_1}\left(-2k_2\hat{A}2 - k_3\hat{A}_1\right), \tag{IV.37e}$$

$$\hat{A}_4 = \frac{1}{24k_1}\left(-2k_2\hat{A}2 - 6k_2\hat{A}_3 - 2k_3\hat{A}_2 + \hat{A}_1\hat{d}_0 - 12k_1\hat{A}_3\right). \tag{IV.37f}$$

Following the same approach as was employed earlier, we obtain

$$\hat{A}_{n+3} = \frac{\{-k_2(n+1)n - k_3(n+1) - k_1(n+1)n(n-1)\}\,\hat{A}_{n+1}}{k_1(n+3)(n+2)(n+1)} + \frac{\{-k_2(n+2)(n+1) - 2k_1(n+2)(n+1)n\}\,\hat{A}_{n+2} + \hat{e}_n}{k_1(n+3)(n+2)(n+1)}, \; n \geq 2, \tag{IV.37g}$$

with

$$\hat{d}_n = \frac{1}{n\hat{c}_0}\sum_{j=1}^{n}(3j - \alpha j - n)\hat{c}_j\hat{d}_{n-j} \;\;,\;\; \hat{d}_0 = (\hat{c}_0)^{(2-\alpha)} \tag{IV.37h}$$

$$\hat{e}_n = \sum_{j=0}^{n}\hat{A}_j\hat{d}_{n-j} \tag{IV.37i}$$

$$\hat{c}_{n>0} = (k_4 n + k_5)(n+1)\hat{A}_{n+1} + k_4(n+2)(n+1)\hat{A}_{n+2} \;\;,\;\; \hat{c}_0 = 2k_4\hat{A}_2 + k_5\hat{A}_1. \tag{IV.37j}$$

The constants $k_1$ - $k_5$ are defined in (IV.32b) - (IV.32f).

Figure 19 shows that the transformed series solution (IV.37) (solid curves) matches the numerical solution as $\eta \to \infty$, as well as $\eta \to 0$. Thus, moving the location of the expansion point from $U = 0$ to $U = 1$ enables a convergent expansion over the whole domain. It should be noted here

that this is distinctly different from the Newtonian case [11], where *both* expansions about $U = 0$ and $U = 1$ converge–although the latter expansion converges faster (see Sections IV.1.3 and IV.1.4). Figure 22a shows the absolute error (the absolute difference) between $N$-term truncations of the convergent series solution (IV.37) and the numerical solution for $\alpha = 0.8$. The numerical values of the constants used to generate this figure are shown in Appendix C.2. Here, we choose to stop at $N = 200$ in construction of Figure 22 because the absolute error is close to machine precision. The dashed curve in Figure 23 shows the infinity norm (maximum absolute error) between the $N$-term truncation of the series solution (IV.37) and the numerical solution taken over $\eta \in [0, L]$ with $L = 11000$ for $\alpha = 0.8$, using the values of constants generated by the numerical solution (see Appendix C.2 for more details). The plateau reached in this figure occurs when further refinements to the power series lead to errors smaller than that of the numerical solution.

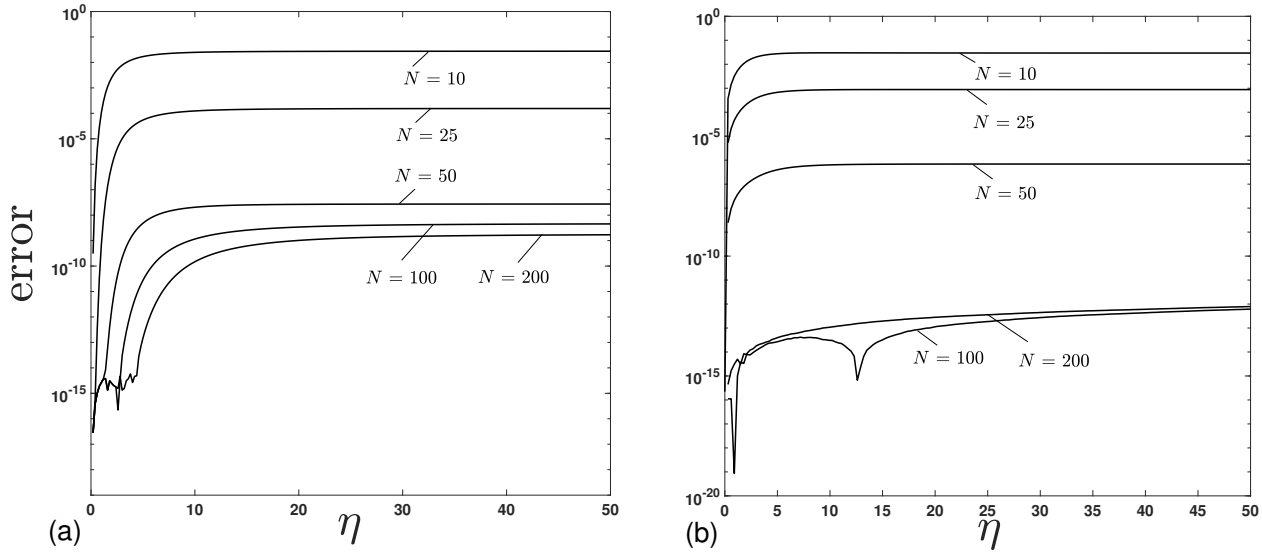


**Figure 22:** Absolute error (the absolute value of the difference) between $N$-term truncations of the convergent series solution (IV.37) and the numerical solution (over the domain $\eta \in [0, L]$ with $L = 11000$) for $\alpha = 0.8$, plotted versus $\eta$, using $\kappa$, $C$, and $E$ values (a) generated by the numerical solution, and (b) predicted by equations system (IV.38), discussed in Section IV.2.3.3.

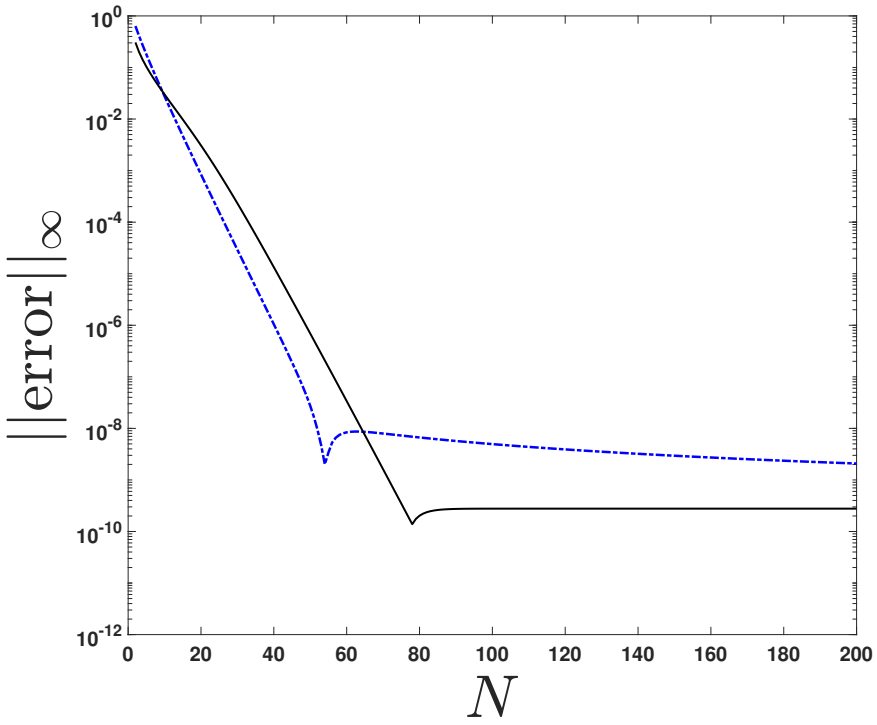


**Figure 23:** The infinity norm (maximum absolute error) between $N$-terms truncations of (IV.37) and the numerical solution (occurring over $\eta \in [0, L]$ with $L = 11000$) for $\alpha = 0.8$, plotted versus $N$. The dashed and solid curves correspond to when numerical and algorithmically predicted values (using equations system (IV.38) discussed in Section IV.2.3.3) of $\kappa$, $C$, and $E$ are used, respectively. Convergence of the numerical and algorithmically predicted values of the constants are reported in respective Tables 3 and 4 of Appendix C.2.

#### IV.2.3.3 Prediction of unknown parameters

Thus far, results have been presented where the numerically-obtained values of the constants $\kappa$, $C$, and $E$ have been used. With the aim of making the series solution (IV.37) independent of the numerical solution, we adapt an algorithm used by Barlow et al. [1] (also used for Newtonian Sakiadis Problem [11] in Section IV.1.5) to predict the values of the constants $\kappa$, $C$, and $E$. In that

study, it is sufficient to construct a system of equations for the unknowns by choosing the last $\mathcal{N}$ coefficients of the series solution to be zero, where $\mathcal{N}$ is the number of unknowns ($\mathcal{N} = 3$ in this problem: $\kappa$, $C$, and $E$). For a convergent series, it is most certainly the case that the last coefficient approaches zero as $N \to \infty$, so this assumption is self consistent in the limit. Additionally, from the perspective of the number of equations and unknowns, we need three equations to find $\kappa$, $C$, and $E$. The assumption of series convergence implicit in the equations to solve is validated by convergence of the algorithm itself for increasingly large numbers of series terms. However, in this non-Newtonian extension we find that the three equations ($\hat{A}_N = 0$, $\hat{A}_{N-1} = 0$, and $\hat{A}_{N-2} = 0$) are linearly dependent, as evident by the determinant of the 3x3 Jacobian constructed by derivatives with respect to the three unknowns. For that reason, we alter the algorithm such that we use one of those equations ($\hat{A}_N = 0$) (IV.38c). For the remaining two equations we adapt the algorithm used in Newtonian Sakiadis Problem [11] in Section IV.1.5 where conditions are imposed from the side of the domain that is opposite to that of the series' expansion point. The system of equations used here are:

$$\left[\sum_{n=0}^{N} \hat{A}_n(-1)^n\right] - C = 0, \tag{IV.38a}$$

$$\left[\sum_{n=0}^{N} n\hat{A}_n(-1)^{n-1}\right] - A_1 = 0, \tag{IV.38b}$$

$$\hat{A}_N = 0, \tag{IV.38c}$$

where $C$, $A_1$, and $\hat{A}_N$ are defined in (IV.5), (IV.35e), and (IV.37g), respectively. Note that (IV.38a) and (IV.38b) correspond to the boundary conditions $F(U = 0) = C$ and $F'(U = 0) = A_1$. Newton's Method is used to solve the system of equations (IV.38), and the details are provided in Appendix C.3.

Figures 22b and 23 (solid curve) show typical results of the solution of equations system (IV.38), with a tolerance of $10^{-15}$ used in the implementation of Newton's method. Figure 22b shows the absolute error vs $\eta$ compared with the numerical solution when $\kappa$, $C$, and $E$ are predicted

algorithmically for $\alpha = 0.8$. The solid curve in Figure 23 shows the maximum absolute error vs $N$ compared with the numerical solution when $\kappa$, $C$, and $E$ are predicted using the solution of equations system (IV.38). As seen by inspection, the accuracy of the solution, $f(\eta)$, increases with the number of terms used in the series. It is important to note that we do not explicitly enforce that $f(\eta \to \infty) \to C$ (for all $N$) at $U = 0$ (corresponding to $\eta \to \infty$) in (IV.37a), as we do for the expansion in (IV.33) (refer to (IV.35d)). Consequently, for $N = 100$ and 200, this allows for the curves in Figure 22b to ultimately attain lower error values than those shown in Figure 22a.

The key issue with using the series solution (IV.37) is its need to access the value of the asymptotic constant $E$. Although not shown here, we have examined a variety of other permissible $\alpha$ values, and we find that the numerical $E$ ultimately becomes negative for $\alpha < 0.74$, thus invalidating the use of the gauge function (IV.30) due to a branch point singularity that arises in the physical $\eta$ domain; in this range of $\alpha$, equations system (IV.38) fails to predict converged values for $\kappa$, $C$, and $E$. That said, the asymptotic form with $E$ being negative is perfectly valid for large enough $\eta$, which is the region in which the asymptotic form itself is valid.

#### IV.2.4 Asymptotically motivated approximant

Since a convergent power series solution has only been obtained for $0.74 < \alpha < 1$, we consider an alternative approach to obtain an analytical form over the full range of $0.5 < \alpha < 1$. Note that the form we will obtain can be used as an alternative to the convergent series over the full range of $\alpha$, although some numerical results are needed to do so. One way of overcoming convergence barriers in divergent series solutions is to analytically continue them via Padé approximants [50]. To this end, we utilize an asymptotically motivated approximant [1] in the form of a modified Padé approximant as

$$f_A = C - \left[ \frac{\sum_{n=0}^{M+1} P_n \eta^n}{\sum_{n=0}^{M} Q_n \eta^n} \right]^{\lambda} . \tag{IV.39a}$$

In (IV.39a), $C$ and $\lambda$ are given by (IV.5) and (IV.30c), respectively. To solve for the coefficients $P_n$ and $Q_n$ in (IV.39a), we write (IV.39a) in the form

$$\left[C - \sum_{n=0}^{\infty} a_n \eta^n\right]^{1/\lambda} = \frac{\sum_{n=0}^{M+1} P_n \eta^n}{\sum_{n=0}^{M} Q_n \eta^n}, \tag{IV.39b}$$

where the coefficients $a_n$ are given in (IV.28a). Using JCP Miller's formula (see Appendix A.1) on the left hand side of (IV.39b), a standard Padé solver may be employed to solve for the coefficients $P_n$ and $Q_n$ on the right-hand side of (IV.39b). Note that for $\eta \to \infty$, $f_A \sim C - (P_{M+1}/Q_M)^{\lambda}\eta^{\lambda}$, which is consistent with the asymptotic form (IV.29f) for $\eta \gg E$. To implement the approximant, we use the numerically predicted values of $\kappa$ and $C$, reported in Table 1. This is precisely the approach taken by Belden et al. [51] in the asymptotic approximant solution to the Falkner Skan equation. More details about the numerical prediction for various domain lengths $L$ for $\alpha = 0.8$ are provided in Appendix C.2. As seen in Table 1, the numerical solution of the boundary value problem reveals a high sensitivity of parameter values to domain length, and this sensitivity increases as $\alpha$ decreases. Figures 24 and 25 show the absolute error between $M$-term truncations of approximant (IV.39) and the numerical solution for $\alpha = 0.8$ and $\alpha = 0.6$, respectively.

**Table 1:** Numerical values of the constants $\kappa$ and $C$ for the non-Newtonian Sakiadis Problem. The values are computed using the shooting method algorithm explained in Appendix C.1 with $\eta = \infty$ replaced with a finite surrogate $L$ given in the table. The values of $\kappa$ and $C$ are accurate to within the decimal places reported here, based on convergence by successively increasing $L$.

| $\alpha$ | $L$ | $\kappa$ | $C$ |
|---|---|---|---|
| 0.99 | 100 | -0.4434518189261262 | 1.6250769221853265 |
| 0.9 | 2000 | -0.4413601253597191 | 1.717915813011322 |
| 0.8 | 11000 | -0.440672715940425 | 1.860152537 |
| 0.7 | 11000 | -0.442664523 | 2.08739 |
| 0.6 | 11000 | -0.44906693 | 2.56 |
| 0.55 | 40000 | -0.454851 | 3.1 |

There are a few defective approximants [6] that arise between the indicated truncations of the approximant in Figures 24 and 25, in which the denominator in (IV.39b) becomes zero for positive $\eta$ values; it is standard practice to ignore these when assessing the solution [50]. We note that the smallest error is obtained at $M = 26$ and $M = 15$ for the cases of $\alpha = 0.8$ and 0.6, respectively. For any larger value of $M$, the error oscillates between curves that are similar to $M = 25$ and 27 in Figure 24 and $M = 12$ and 26 in Figure 25. In both cases, we accept the solution as converged, as its precision (defined here as amplitude of these oscillations) is consistent with that of the inputs, particularly $C$ (see Table 1). Figure 26 shows the infinity norm (maximum absolute error) vs $\alpha$ for

[6] It is possible that poles of a Padé approximant arise within the physical domain of a problem for particular degrees of denominator and numerator. If the exact solution is expected to be finite within the physical domain, these Padés are deemed *defective*. For this exact reason, we did not use $M = 25$ in Figure 25 as it led to a defective approximant for the case of $\alpha = 0.6$.

the permissible range of $\alpha$ values when $M = 20$, using the numerical values of the constants $\kappa$ and $C$.

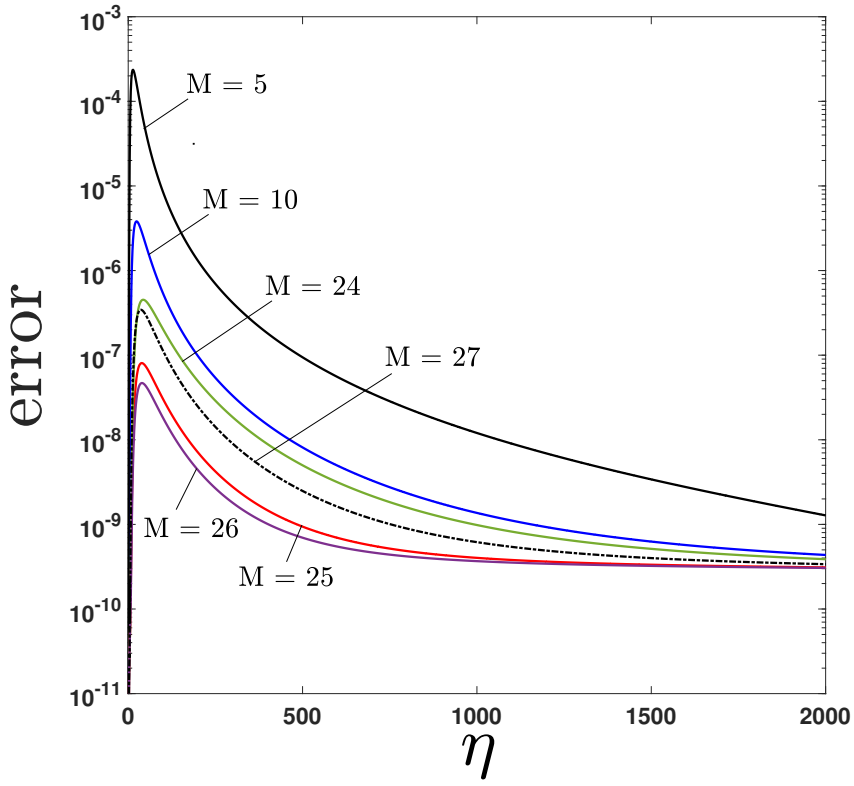


**Figure 24:** Absolute error between $M$-term truncations of the approximant (IV.39) and the numerical solution (occurring over $\eta \in [0, L]$ with $L = 11000$) for $\alpha = 0.8$, plotted versus $\eta$, using $\kappa$ and $C$ generated by the numerical solution. Error decreases until $M = 26$, after which it oscillates between curves that are similar to $M = 25$ and 27.

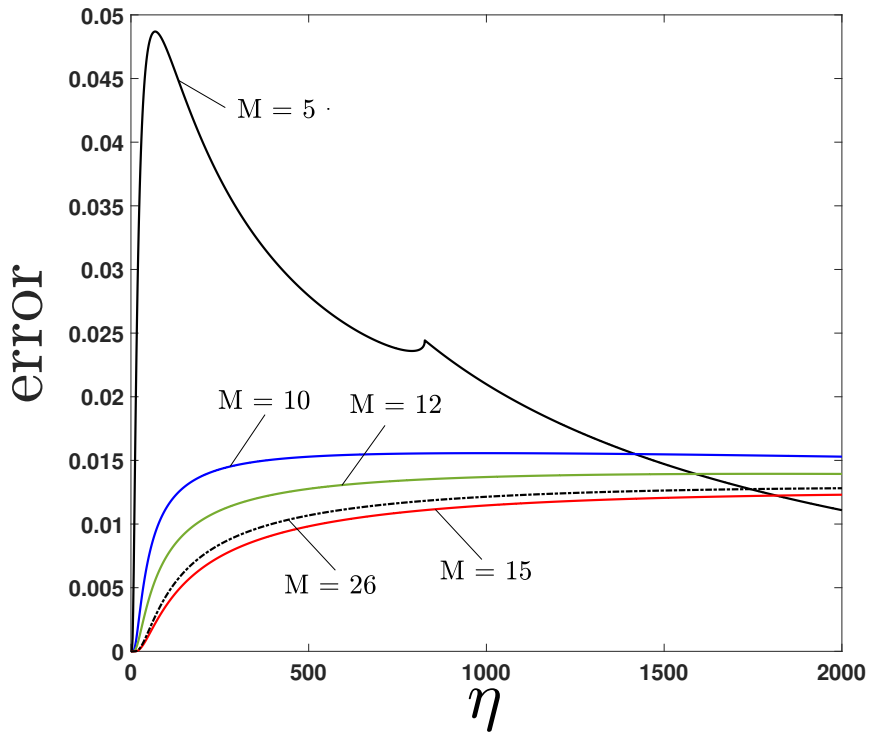


**Figure 25:** Absolute error between $M$-terms truncations of the approximant (IV.39) and the numerical solution (occurring over $\eta \in [0, L]$ with $L = 11000$) for $\alpha = 0.6$, plotted versus $\eta$, using $\kappa$ and $C$ generated by the numerical solution. Error decreases until $M = 15$, after which it oscillates between curves that are similar to $M = 12$ and 26.

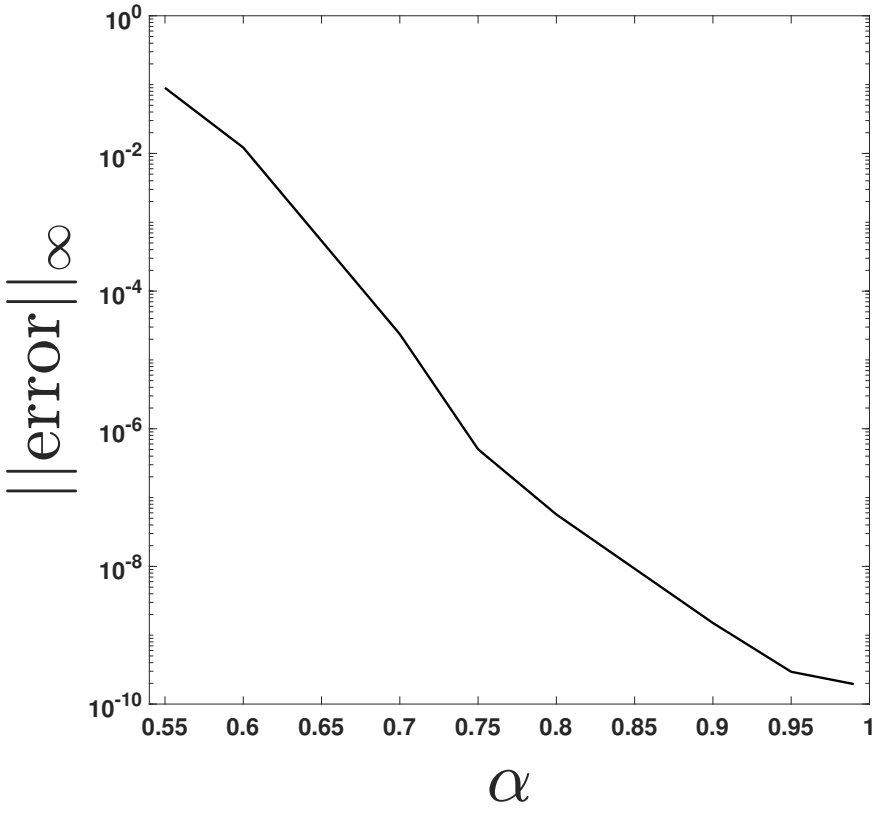


**Figure 26:** Maximum absolute error between approximant (IV.39) (with $M = 20$) and the numerical solution (occurring over $\eta \in [0, L]$) plotted versus $\alpha$, using $\kappa$ and $C$ generated by the numerical solution. The values of $C$ and $\kappa$ are shown in Table 1.

### IV.2.5 Post-processing: Analytically obtained streamlines

Now that we have accurate analytical solutions to (IV.27), we may insert $f$, given by either (IV.35) (for $0.74 \leq \alpha \leq 1$)[7] or (IV.39) (for $0.5 < \alpha < 1$), and its derivative $f'(\eta)$ (which may obtained analytically) into (IV.26) to obtain the $u$ velocity field, which is shown in the right-hand plot in Figure 27. The paths of fluid points, i.e., the streamlines of constant $\psi$, may be extracted easily from the analytical solution. To do so, we explicitly solve for the $x$ and $y$ coordinates of a given

[7]For $\alpha = 1$, one can use the Newtonian result (IV.14) in place of (IV.35); see Section IV.1.3 [11].

streamline $\psi =$ constant by rearranging the equations in (IV.25) to yield:

$$y = \frac{\psi\eta}{u_w f(\eta)}, \quad x = \frac{\rho}{K u_w^{2\alpha-1}} \left( \frac{\psi}{f(\eta)} \right)^{\alpha+1}. \tag{IV.40}$$

Equation (IV.40) provides a parametric representation of the streamlines in terms of $\eta$ and $f(\eta)$, the latter given analytically by (IV.35) or (IV.39). Figure 27 provides a typical streamline plot extracted in this way. In the figure, a dashed curve plots the boundary layer thickness $y = \eta \left( K\ x\ u_w^{\alpha-2}/\rho \right)^{1/(\alpha+1)}$, defined here as the locus of points where the fluid velocity is reduced to 10% of the wall velocity; according to (IV.25a), this occurs when $u/u_w = df/d\eta = 0.1$. From the topmost plot of Figure 27, this occurs when $\eta = 4.04$. The benefit of the analytical solution is clearly indicated here, as streamline plots can be generated accurately to any desired resolution with low computational cost.

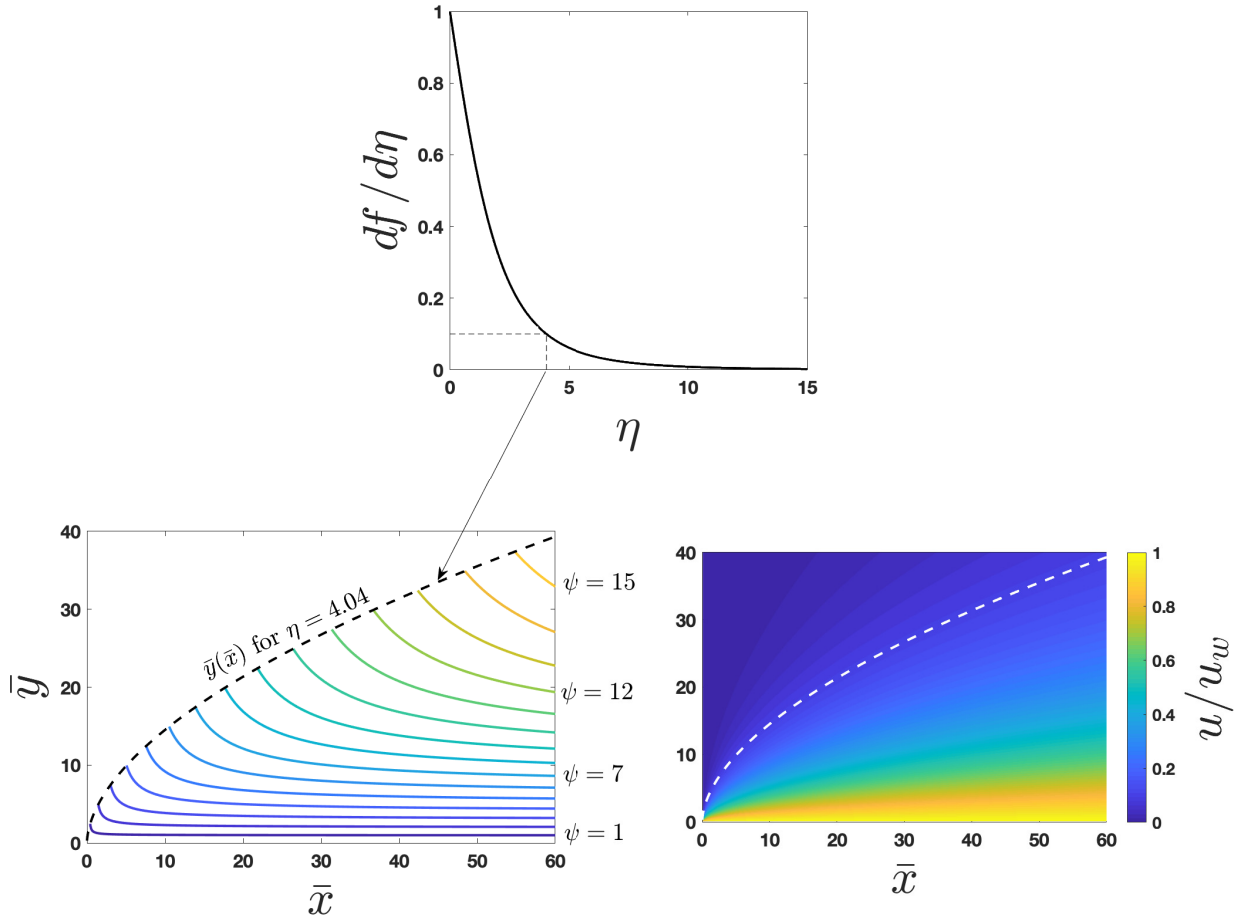


**Figure 27:** (top) $df/d\eta$ obtained analytically from (IV.35) for $\alpha = 0.8$ (using $C$, $\kappa$, and $E$ values from Table 4 with $N = 400$, using system of equations (IV.38)), with gridlines indicating that $df/d\eta = u/u_w = 0.1$ at $\eta \approx 4.04$. (left) Contours of constant $\psi$ obtained analytically from (IV.35) (using 27 terms) and (IV.25b), displayed in increments of $\Delta\psi = 1$ in the $\bar{y} \equiv u_w y$ vs. $\bar{x} \equiv K u_w^{2\alpha-1} x/\rho$ plane. The dashed curve is the envelope of the boundary layer (chosen here to be the locus of points at which $u/u_w = 0.1$), and restricts the display of the streamlines for velocities where $u/u_w > 0.1$. (right) The $u$ velocity field obtained analytically from (IV.35) (using 27 terms) and (IV.26).

### IV.2.6 Summary: The Non-Newtonian Sakiadis Problem

In this chapter, we extended the approach used for the Newtonian Sakiadis boundary layer problem and provided a convergent power series solution, valid for $0.74 \leq \alpha \leq 1$ ($\alpha = 1$ for the case of Newtonian fluids), using the asymptotic expansion as $\eta \to \infty$ to determine a gauge function for the series. In the non-Newtonian Sakiadis boundary layer problem, the asymptotically motivated series fails when the gauge function is unable to completely transverse the physical domain due to a branch point singularity that arises in the asymptotic form. We note that although we developed an asymptotic approximant to model cases where $0.5 < \alpha < 0.74$, the approximant is capable of representing the solution for all $\alpha$ values in the range $0.5 < \alpha < 1$. Once obtained, the analytical solutions enable computationally-efficient post-processing to extract streamlines to any desired resolution.

# V. Conclusions

In the three problems examined in this dissertation, the long distance asymptotic behaviour of their solutions provided insights about the structure of the gauge function and/or the method of re-summing and analytically continuing diverging series solutions. In the Flat Wall and Sakiadis boundary layer problems, the asymptotic solution, obtained by the method of dominant balance [20], provided the structure of the gauge function. On the other hand, in the Cylindrical Wall Problem, the asymptotic solution provided the structure of the pre-factor only, which helped to increase the rate of convergence.

As perhaps might be expected, the use of asymptotically motivated gauge functions is not foolproof—it does not always lead to convergent series expansions. However, in such cases, we have found that a further examination of the radius of convergence using mappings motivated from asymptotic behaviors often is a necessary step towards achieving a convergent series representation. In the Non-Newtonian Sakiadis Problem, using a gauge function directly deduced from asymptotic behaviors is not enough—it is also necessary to change the expansion location to assure that the radius of convergence encompasses the entire domain. And, as also seen in the Non-Newtonian Sakiadis Problem, sometimes a gauge function itself becomes ill-defined over the domain, and alternative approximant approaches are needed to obtain a useful solution.

In this dissertation, we solve for an unknown parameter or multiple parameters in a problem in a way that is analogous to shooting methods in the solution of ODEs. In particular, power series methods require that problems be posed as initial value problems. This often leads to unknown initial parameters at one end of the domain which need to be determined to meet boundary conditions at the other end of the domain. In the Cylindrical Wall Problem, where there was only one unknown, the meniscus height at the cylinder wall, denoted by $a_0$, we set

the last $\bar{A}_n$ coefficient to zero ($\bar{A}_N = 0$); this approach has been used previously by Balow et al [1]. In the Newtonian Sakiadis Problem, we used the boundary conditions on the side of the domain opposite that of the expansion point ($R$, $R'$, and $R''$ at $U = 1$, which is equivalent to $\eta = 0$) to develop a system of three equations and solve for the three unknown parameters. In the Non-Newtonian Sakiadis Problem, we had to combine the approaches used in the previous two problems; we set the last $\hat{A}_n$ coefficient to zero ($\hat{A}_N = 0$) for one of the equations, and used the boundary conditions at $\eta \to \infty$ for the remaining two equations. Details about this approach are provided in Section IV.2.3.3 and Appendix C.3.

Overall, this work has expanded our ability to solve non-linear ODEs by establishing appropriate gauge functions which are motivated by long-distance asymptotic solutions. Through this work, we have formalized a methodology to solve non-linear ODEs through variable transformation which naturally leads to expansions in terms of a nontrivial gauge function. Moreover, we have established an algorithm to transform a BVP to an IVP and to determine unknown constants by imposing unused conditions—this is analogous to a numerical shooting method. The result is a complete solution to a BVP that is self-contained and not reliant on numerically determined inputs. The approach used in this thesis supports a growing body of literature [1–7] developed by our research group that demonstrates that power series solutions are a viable method to obtain analytical solutions to nonlinear ODEs.

# A. Appendix: Useful formulae for manipulating series

## A.1 Raising a series to a power

The following relation is JCP Miller's formula for raising a series to a power [18]:

$$\left(\sum_{n=0}^{\infty} a_n x^n\right)^{\gamma} = \sum_{n=0}^{\infty} b_n x^n, \tag{A.1a}$$

where

$$b_{n>0} = \frac{1}{n\ a_0} \sum_{j=1}^{n} (j\gamma - n + j) a_j b_{n-j}\ ,\ b_0 = (a_0)^{\gamma}\ ,\ a_0 \neq 0. \tag{A.1b}$$

## A.2 Product of two series

The following relation is the well-known Cauchy product of two series [17]:

$$\sum_{n=0}^{\infty} a_n x^n \sum_{n=0}^{\infty} b_n x^n = \sum_{n=0}^{\infty} \left(\sum_{j=0}^{n} a_j b_{n-j}\right) x^n. \tag{A.2}$$

## A.3 Generalized product rule

The generalized product (Leibniz's) rule applied to two functions is given as [52]

$$\frac{d^n\,(uv)}{dy^n} = \sum_{k=0}^{n} \binom{n}{k} \frac{d^{n-k}u}{dy^{n-k}}\ \frac{d^k v}{dy^k} \tag{A.3}$$

and is important in determining the coefficients of an Eulerized series as described in Appendix B.1.

## A.4 Chain rule

The chain rule applied to a composite function $F(y(\eta)) = f(\eta)$ is given, for first and second derivatives, as

$$\frac{df}{d\eta} = \frac{dF}{dy}\frac{dy}{d\eta}, \tag{A.4a}$$

$$\frac{d^2f}{d\eta^2} = \frac{d^2F}{dy^2}\left(\frac{dy}{d\eta}\right)^2 + \frac{dF}{dy}\frac{d^2y}{d\eta^2}. \tag{A.4b}$$

The inversion of (A.4) is given by

$$\frac{dF}{dy} = \frac{df}{d\eta}\left(\frac{dy}{d\eta}\right)^{-1}, \tag{A.5a}$$

$$\frac{d^2F}{dy^2} = \frac{d^2f}{d\eta^2}\left(\frac{dy}{d\eta}\right)^{-2} - \frac{df}{d\eta}\frac{d^2y}{d\eta^2}\left(\frac{dy}{d\eta}\right)^{-3}, \tag{A.5b}$$

which will be useful in expressing the Bessel series in terms of the Euler transformed variable (i.e., the gauge function) in Appendix B.5.

# B. Appendix: The meniscus formed on the outside of a circular cylinder

## B.1 Euler transformation

Given a power series

$$f = \sum_{n=0}^{\infty} a_n x^n, \tag{B.1}$$

the Euler Sum is defined as follows

$$f = \sum_{n=0}^{\infty} b_n \left( \frac{x}{x+S} \right)^n, \tag{B.2a}$$

where

$$b_{n>0} = \sum_{m=1}^{n} \binom{n-1}{m-1} a_m S^m, \; b_0 = a_0. \tag{B.2b}$$

Note that (B.2a) is a power series in terms of the gauge function

$$y \equiv x/(x+S), \tag{B.3}$$

such that the physical domain $x \in [0, \infty)$ maps to the transformed physical domain $y \in [0, 1]$. The derivation of (B.2b) is provided below.

First, equating the right-hand-sides of (B.1) and (B.2a) and using definition (B.3) to write in terms of $y$, we have

$$\sum_{m=0}^{\infty} a_m \left( \frac{yS}{1-y} \right)^m = \sum_{m=0}^{\infty} b_m y^m, \tag{B.4}$$

where a deliberate switch has been made to using the index $m$ instead of $n$ so that we may extract $b_n$ at a specific value within the above (i.e., at $m = n$) as

$$b_n = \frac{1}{n!} \left\{ \frac{d^n}{dy^n} \left[ \sum_{m=0}^{\infty} a_m \left( \frac{yS}{1-y} \right)^m \right] \right\}_{y=0}. \tag{B.5}$$

Note that the above expression comes from applying the definition of a coefficient of a Taylor expansion about $y = 0$, which is precisely what the right-hand side of (B.4) is. Our task remains to show that the infinite series given by (B.5) may be rewritten as the finite series (B.2b). Interchanging the differentiation and summation operators and rewriting the inside as a product, (B.5) becomes

$$b_n = \frac{1}{n!} \left\{ \sum_{m=0}^{\infty} a_m S^m \frac{d^n}{dy^n} \left[ y^m \left(1-y\right)^{-m} \right] \right\}_{y=0}. \tag{B.6}$$

In order to apply the generalized product rule to the $\left[ y^m \left(1-y\right)^{-m} \right]$ term above, we first recognize that individual generalized derivatives of the two terms are

$$\frac{d^j (y^m)}{dy^j} = \left[ \prod_{\ell=0}^{j-1} (m-\ell) \right] y^{m-j} \tag{B.7a}$$

and

$$\frac{d^j \left[ (1-y)^{-m} \right]}{dy^j} = \left[ \prod_{\ell=0}^{j-1} (m+\ell) \right] (1-y)^{-m-j}. \tag{B.7b}$$

Substituting (B.7) into the generalized product rule (A.3) to evaluate the derivative in (B.6), we obtain the expression

$$b_n = \frac{1}{n!} \left\{ \sum_{m=0}^{\infty} a_m S^m \sum_{k=0}^{n} \left[ \binom{n}{k} \left[ \prod_{\ell=0}^{n-k-1} (m-\ell) \right] y^{m-n+k} \left[ \prod_{\ell=0}^{k-1} (m+\ell) \right] (1-y)^{-m-k} \right] \right\}_{y=0}.$$

Finally, we evaluate the above expression at $y = 0$ and note that the only nonzero contributions will come from $y^0$ terms in the inner sum, which correspond with an index of $k = n - m$. Since $k$ is a positive index, this tells us that $m$ cannot be greater than $n$, thus placing an upper limit on the outer $m$-sum. Setting $y = 0$, only retaining the $k = n - m$ term in the inner sum, and truncating

the outer sum to $n$ terms, leads to

$$\begin{aligned} b_n &= \frac{1}{n!}\sum_{m=0}^{n} a_m S^m \binom{n}{n-m} \qquad \prod_{\ell=0}^{m-1}(m-\ell) \qquad \prod_{\ell=0}^{n-m-1}(m+\ell) \\ &= \frac{1}{n!}\sum_{m=0}^{n} a_m S^m \frac{n!}{m!\,(n-m)!} \qquad m! \qquad \frac{(n-1)!}{(m-1)!} \\ &= \sum_{m=0}^{n} a_m S^m \frac{(n-1)!}{(m-1)!\,(n-m)!} \\ &= \sum_{m=0}^{n} \binom{n-1}{m-1} a_m S^m, \end{aligned}$$

which is equivalent to (B.2b).

## B.2 Estimation of the radius of convergence in an Euler transformation

Typically, for nonlinear ODEs, the precise value of the radius of convergence of the power series solution is unknown, but can be estimated (via root test, ratio test, etc.) to within some tolerance. In such cases, we may estimate the true radius of convergence, $x_s$, with an approximation, $S$, as

$$S \equiv \epsilon x_s, \tag{B.8}$$

where $\epsilon \in (0, 2)$. We are afforded this flexibility from Taylor's theorem, which tells us that, through the mapping from $x$ to $y$ given by (B.3), a Taylor expansion about $y = 0$ will converge over the full physical domain $y \in [0, 1]$ as long as singularities lie outside of the circle $|y| = 1$ in the complex $y$ plane. In other words, assuming the closest singularity is due to $x = -x_s$, the following must hold for convergence of the corresponding Euler series:

$$|y\,(x = -x_s)| > 1. \tag{B.9}$$

We know this to be true in the standard Euler series since then the left side of the inequality above becomes $\pm\infty$, from the standard Euler gauge function (B.3). However, if we do not know the exact value of $x_s$ and substitute the Euler transformation

$$y \equiv x/(x + \epsilon x_s), \tag{B.10}$$

into (B.9), we obtain

$$\left|\frac{1}{1-\epsilon}\right| > 1,$$

which tells us that $\epsilon \in (0,2)$ is a valid range to assure convergence of the transformed series. This means that one may use any arbitrarily small value for $S > 0$ in (B.2), as long as it is less than twice the value of the (unknown) exact $x_s$ (the modulus of the actual closest singularity). That said, as $\epsilon \to 1$, the convergence rate of the Eulerized series is expected to improve, since—in this limit—the influence of the singularity is pushed further away from the mapped physical domain.

## B.3 Interface solution for small slope

Equation (III.10) provides the leading order $\tilde{r} \to \infty$ asymptotic behavior of the interface solution given as:

$$\overline{h}(\tilde{r}) \sim DK_0\left(\sqrt{B}\,(\tilde{r}+1)\right), \tag{B.11}$$

where $D$ is an unknown constant and $K_0(z)$ is the modified Bessel function of zeroth order. Note that this solution is valid for $d\overline{h}/d\tilde{r} \ll 1$ since $\overline{h} \to 0$ as $\tilde{r} \to \infty$ according to (III.2d). In a configuration for which $d\overline{h}/d\tilde{r} \ll 1$ for all $\tilde{r} \in (0,\infty)$, (B.11) provides an excellent approximation to the interface solution with the constant, $D$, determined as follows.

The boundary condition (III.2c) is rewritten here for convenience as:

$$\frac{d\overline{h}}{d\tilde{r}} = -\cot\theta \text{ at } \tilde{r} = 0. \tag{B.12}$$

Noting that:

$$\frac{dK_0(z)}{dz} = -K_1(z),$$

where $K_1(z)$ is the modified Bessel function of first order, we differentiate (B.11) to obtain:

$$\frac{d\overline{h}}{d\tilde{r}} \sim -D\sqrt{B}K_0\left(\sqrt{B}\,(\tilde{r}+1)\right) \text{ for } d\overline{h}/d\tilde{r} \ll 1. \tag{B.13}$$

Provided that $\cot\theta \ll 1$, (B.13) is valid for all $\tilde{r} \in (0,\infty)$, and thus the constraint (B.12) may be applied to determine $D$ as:

$$D = \frac{\cot\theta}{\sqrt{B}K_1\left(\sqrt{B}\right)}. \tag{B.14}$$

Finally, we substitute (B.14) into (B.11) to yield:

$$\overline{h}(\tilde{r}) \sim \frac{\cot\theta}{\sqrt{B}K_1\left(\sqrt{B}\right)} K_0\left(\sqrt{B}\,(\tilde{r}+1)\right) \text{ for } \cot\theta \ll 1, \text{ where } \tilde{r} \in (0,\infty)\,. \tag{B.15a}$$

In accordance with the restriction that $\cot\theta \ll 1$, (B.15a) is valid for nearly horizontal interfaces for which values of $\theta$ lie near $\pi/2$, regardless of the value of the Bond number, $B$. The height of the interface, then at the cylindrical wall ($\tilde{r} = 0$), is thus given as:

$$\overline{h}(0) \sim \frac{\cot\theta}{\sqrt{B}} \frac{K_0\left(\sqrt{B}\right)}{K_1\left(\sqrt{B}\right)}, \text{ for } \cot\theta \ll 1. \tag{B.15b}$$

The result (B.15) serves as a useful analytical check on numerical and power series predictions for nearly horizontal interfaces.

## B.4 Computation of the Euler coefficients in (III.8) via the transformed differential equation (III.7a)

After making the variable transformation (III.4) in our governing ODE (III.2b), we obtain the transformed ODE (III.7a), rewritten here in a slightly different form as

$$G'' = \frac{S^2}{(1-U)^4}\left\{\frac{2(1-U)^3}{S^2}G' + \frac{\left(\dfrac{US}{1-U}+1\right)\left(\dfrac{(1-U)^4}{S^2}G'^2+1\right)^{3/2}BG - \dfrac{(1-U)^6}{S^3}G'^3 - \dfrac{(1-U)^2}{S}G'}{\dfrac{US}{1-U}+1}\right\}. \tag{B.16}$$

Our goal is to obtain a power series solution of (B.16) in the form (III.8a), rewritten here for convenience as

$$G(U) = \sum_{n=0}^{\infty} \hat{A}_n U^n. \tag{B.17}$$

To do so, we note that, by direct differentiation, the first $n$ terms of the Taylor series of $G'$ depend only on the first $n+1$ terms of $G$. By Cauchy's product rule and JCP Miller's Formula, the same is also true of powers and products of these terms. As such, the RHS of (B.16) will have an $n$-th Taylor coefficient that can be expressed as a recursive expression involving the first $n+1$ Taylor coefficients of $G$. Meanwhile, the LHS will give the $n+2$ Taylor coefficient of $G$ (up to a factor of $(n+1)(n+2)$), allowing one to recursive compute $\hat{A}_{n+2}$ from the previous Taylor coefficients $\{\hat{A}_0, \hat{A}_1, ..., \hat{A}_{n+1}\}$. More explicitly, we note that by the binomial theorem we have

$$\frac{S^2}{(1-U)^4} = S^2 \sum_{n=0}^{\infty} \binom{n+3}{3} U^n. \tag{B.18}$$

Hence by Cauchy's product rule and direct differentiation if we write

$$\frac{2(1-U)^3}{S^2}G' + \frac{\left(\frac{US}{1-U}+1\right)\left(\frac{(1-U)^4}{S^2}G'^2+1\right)^{3/2}BG - \frac{(1-U)^6}{S^3}G'^3 - \frac{(1-U)^2}{S}G'}{\frac{US}{1-U}+1} = \sum_{n=0}^{\infty} w_n U^n, \tag{B.19}$$

then the $w_n$ will have a recursive expression in terms of $\hat{A}_n$ only up to $\hat{A}_{n+1}$, and equation (B.16) becomes

$$\sum_{n=0}^{\infty}(n+1)(n+2)\hat{A}_{n+2} = S^2 \sum_{n=0}^{\infty}\left[\sum_{k=0}^{n}\binom{k+3}{3}w_{n-k}\right]U^n, \tag{B.20}$$

$$\hat{A}_{n+2} = \frac{S^2}{(n+1)(n+2)}\sum_{k=0}^{n}\binom{k+3}{3}w_{n-k}. \tag{B.21}$$

Continuing to work backwards, we can write by Cauchy's product rule that

$$w_n = f_n + \sum_{k=0}^{n}(q_k - t_k - u_k)r_{n-k} \tag{B.22}$$

where

$$\frac{2(1-U)^3}{S^2}G' = \sum_{n=0}^{\infty} f_n U^n \tag{B.23}$$

$$\left(\frac{US}{1-U}+1\right)\left(\frac{(1-U)^4}{S^2}G'^2+1\right)^{3/2} BG = \sum_{n=0}^{\infty} q_n U^n \tag{B.24}$$

$$\frac{(1-U)^6}{S^3}G'^3 = \sum_{n=0}^{\infty} t_n U^n \tag{B.25}$$

$$\frac{(1-U)^2}{S}G' = \sum_{n=0}^{\infty} u_n U^n \tag{B.26}$$

$$\left(\frac{US}{1-U}+1\right)^{-1} = \sum_{n=0}^{\infty} r_n U^n. \tag{B.27}$$

We notice first that by term-by-term differentiation, Cauchy's product rule, and the binomial formula we have the following formulae for $f_n$ and $u_n$:

$$f_n = \frac{2}{S^2}\sum_{k=0}^{n}(-1)^k\binom{3}{k}(n-k+1)\hat{A}_{n-k+1}, \tag{B.28}$$

$$u_n = \frac{1}{S}\sum_{k=0}^{n}(-1)^k\binom{2}{k}(n-k+1)\hat{A}_{n-k+1}. \tag{B.29}$$

Furthermore, by the formula for a geometric series, we have directly that

$$\left(\frac{US}{1-U}+1\right)^{-1} = \frac{(1-U)}{1-(1-S)U} \tag{B.30}$$

$$r_n = (1-S)^n - (1-\delta_{n,0})(1-S)^{n-1}. \tag{B.31}$$

where the Kronecker notation is used such that $\delta_{n,0}$ is 0 when $n \neq 0$ and 1 when $n = 0$. The computation of $t_n$ in (B.25) could be obtained directly using JCP Miller's formula on $G'^3$ followed by Cauchy's product rule; instead, we first build the formula for the term involving $G'^2$ in (B.19), and then extract the result for $t_n$ from that. That is, we define

$$\frac{(1-U)^4}{S^2}G'^2 = \sum_{n=0}^{\infty} d_n U^n, \tag{B.32}$$

and by Cauchy's product rule have

$$d_n = \sum_{k=0}^{n} u_k u_{n-k}. \tag{B.33}$$

The expression for $t_n$ can be obtained by taking the Cauchy product of (B.32) and (B.26) to yield

$$t_n = \sum_{k=0}^{n} d_k u_{n-k}. \tag{B.34}$$

From here it remains only for us to compute $q_n$. We begin by writing

$$\frac{(1-U)^4}{S^2} G'^2 + 1 = \sum_{n=0}^{\infty} \bar{d}_n U^n, \tag{B.35}$$

then we have

$$\bar{d}_n = d_n + \delta_{n,0}. \tag{B.36}$$

Proceeding in the same fashion if we write

$$\left( \frac{(1-U)^4}{S^2} G'^2 + 1 \right)^{3/2} = \sum_{n=0}^{\infty} p_n U^n, \tag{B.37}$$

then by JCP Miller's formula we have

$$p_0 = \bar{d}_0^{3/2} \qquad p_{n>1} = \frac{1}{n\bar{d}_0} \sum_{k=1}^{n} \left( \frac{5}{2}k - n \right) \bar{d}_k p_{n-k}. \tag{B.38}$$

Writing via geometric series that

$$\frac{US}{1-U} + 1 = \sum_{n=0}^{\infty} \bar{\ell}_n U^n$$

$$\bar{\ell}_n = S + \delta_{n,0}(1-S),$$

then, if we write

$$\left( \frac{US}{1-U} + 1 \right) G = \sum_{n=0}^{\infty} \ell_n U^n, \tag{B.39}$$

Cauchy's product rule gives

$$\ell_n = \sum_{k=0}^{n} \bar{\ell}_k \hat{A}_{n-k}. \tag{B.40}$$

One final application of Cauchy's product rule completes the recurrence by writing

$$q_n = B \sum_{k=0}^{n} \ell_k p_{n-k}. \tag{B.41}$$

In summary, the preceding coefficients $f_n$, $q_n$, $t_n$, $u_n$, $\ell_n$, $d_n$, $r_n$, and $p_n$ are all utilized in the power series solution (III.8) in the main text.

## B.5 Computation of the Euler coefficients in (III.11) after inclusion of the modified Bessel function prefactor

Here, we re-sum to accelerate the convergence of the power series solution, making direct use of the previously derived series (III.8) written in terms of the Euler transformed variable. The re-summation is enabled because the Euler coefficients in (III.8) are computationally stable. This is in direct contrast to the original attempt to use the divergent series coefficients (III.3) to construct the Euler coefficients using (III.6)–which leads to computational errors. Here, we rewrite for reference (III.8a) as

$$G(U) = \sum_{n=0}^{\infty} \hat{A}_n U^n, \tag{B.42a}$$

where the coefficients $\hat{A}_n$ are given by (III.8) and

$$U(\tilde{r}) = \frac{\tilde{r}}{\tilde{r}+S}. \tag{B.42b}$$

We accelerate convergence of this summation by the inclusion of the leading asymptotic behavior in terms of the modified Bessel function of the second kind of zeroth order in accordance with (III.10) and (III.11a), written for reference here as

$$\bar{h}(\tilde{r}) = K_0\left(\sqrt{B}(\tilde{r}+1)\right) \sum_{n=0}^{\infty} \bar{A}_n \left(\frac{\tilde{r}}{\tilde{r}+S}\right)^n. \tag{B.43}$$

By direct rearrangement of (B.42b), we have $\tilde{r} = \frac{SU}{1-U}$ , and noting that $h(r) = h(r(U)) = G(U)$, we have

$$G(U) = K_0\left(\sqrt{B}\left(\frac{US}{1-U}+1\right)\right) \sum_{n=0}^{\infty} \bar{A}_n U^n, \tag{B.44a}$$

or equivalently:

$$G(U)\left[K_0\left(\sqrt{B}\left(\frac{US}{1-U}+1\right)\right)\right]^{-1} = \sum_{n=0}^{\infty} \bar{A}_n U^n. \tag{B.44b}$$

Since $G(U)$ is known in terms of $\hat{A}_n$ from (B.42), we can obtained a relationship between $\bar{A}_n$ (the expansion with the prefactor) and $\hat{A}_n$ (the original Euler expansion) as follows. We first define the

argument of the Bessel function solution in (B.44) as

$$y(U) \equiv \sqrt{B}\left(\frac{US}{1-U}+1\right), \tag{B.45}$$

and express the modified Bessel function portion of (B.44) as

$$K_0(y) = K_0\left(y(U)\right) = f(U) = \sum_{n=0}^{\infty} \bar{\zeta}_n U^n. \tag{B.46}$$

Using this expansion form, we employ JCP Miller's formula (A.1) to yield:

$$\left[K_0\left(\sqrt{B}\left(\frac{US}{1-U}+1\right)\right)\right]^{-1} = \sum_{n=0}^{\infty} \zeta_n U^n, \tag{B.47a}$$

$$\zeta_n = \frac{-1}{\bar{\zeta}_0}\sum_{k=1}^{n} \bar{\zeta}_k \zeta_{n-k} \qquad \zeta_0 = \bar{\zeta}_0^{-1}. \tag{B.47b}$$

Subsequently, by inserting (B.47a) into (B.44b) and using Cauchy's product rule (A.2), we obtain

$$\bar{A}_n = \sum_{k=0}^{n} \zeta_k \hat{A}_{n-k}. \tag{B.48}$$

The result (B.48) provides the necessary coefficients for the resummation–at this point, however, we have not yet determined the coefficients $\bar{\zeta}_n$ in (B.46), which we now obtain.

To proceed, we begin with the modified Bessel function governing equation (III.9) in the main text, rewritten in terms of $y$ as

$$\frac{d^2K_0}{dy^2} + \frac{1}{y}\frac{dK_0}{dy} - K_0 = 0. \tag{B.49}$$

Our goal is to determine the Taylor expansion of $K_0(y(U))$ about $U = 0$, which is precisely the expression (B.46) that we require. Employing the chain rule formulae given by (A.5) (letting $F = K_0$), substituting this result into (B.49), and solving for $\frac{d^2f}{dU^2}$ leads to the expression

$$\frac{d^2f}{dU^2} = \left(\frac{\frac{d^2y}{dU^2}}{\frac{dy}{dU}} - \frac{\frac{dy}{dU}}{y}\right)\frac{df}{dU} + \left(\frac{dy}{dU}\right)^2 f. \tag{B.50}$$

From here we will want to find the power series solution to (B.50) in the form (B.46). For the particular $y$ given by (B.45), we have the algebraic identities

$$\frac{\frac{dy}{dU}}{y} = \frac{1}{1-U} - \frac{1-S}{1-(1-S)U}, \tag{B.51}$$

$$\frac{\frac{d^2y}{dU^2}}{\frac{dy}{dU}} = \frac{2}{1-U}, \tag{B.52}$$

$$\left(\frac{dy}{dU}\right)^2 = \frac{BS^2}{(1-U)^4}. \tag{B.53}$$

Using the Binomial theorem, all of these expressions can be Taylor expanded explicitly as

$$\frac{\frac{dy}{dU}}{y} = \frac{1}{1-U} - \frac{1-S}{1-(1-S)U} = \sum_{n=0}^{\infty} \rho_n U^n = \sum_{n=0}^{\infty} (1-(1-S)^{n+1})U^n,\ \rho_n = 1-(1-S)^{n+1}, \tag{B.54a}$$

$$\frac{\frac{d^2y}{dU^2}}{\frac{dy}{dU}} = \frac{2}{1-U} = 2\sum_{n=0}^{\infty} U^n, \tag{B.54b}$$

$$\left(\frac{dy}{dU}\right)^2 = \frac{BS^2}{(1-U)^4} = BS^2 \sum_{n=0}^{\infty} \binom{n+3}{3} U^n. \tag{B.54c}$$

Furthermore, term-by-term differentiation of (B.46) gives

$$\frac{df}{dU} = \sum_{n=0}^{\infty} (n+1)\bar{\zeta}_{n+1} U^n, \tag{B.55a}$$

$$\frac{d^2f}{dU^2} = \sum_{n=0}^{\infty} (n+1)(n+2)\bar{\zeta}_{n+2} U^n. \tag{B.55b}$$

We substitute the expansion (B.46) and results (B.54)-(B.55) into the ODE (B.50), and after making use of Cauchy's product rule, we obtain

$$\sum_{n=0}^{\infty} (n+1)(n+2)\bar{\zeta}_{n+2} U^n = \sum_{n=0}^{\infty} \left[\sum_{k=0}^{n} (k+1)\bar{\zeta}_{k+1}(2-\rho_{n-k})\right] U^n + BS^2 \sum_{n=0}^{\infty} \left[\sum_{k=0}^{n} \binom{k+3}{3} \bar{\zeta}_{n-k}\right] U^n \tag{B.56}$$

Comparing like terms gives the recurrence relation

$$\bar{\zeta}_{n+2} = \frac{1}{(n+1)(n+2)} \sum_{k=0}^{n} \left\{ (k+1)\bar{\zeta}_{k+1}(2-\rho_{n-k}) + \binom{k+3}{3} \bar{\zeta}_{n-k} \right\}, \tag{B.57a}$$

where we have the initial conditions by direct substitution that

$$\bar{\zeta}_0 = K_0\left(\sqrt{B}\right) \quad \text{and} \quad \bar{\zeta}_1 = -S\sqrt{B}K_1\left(\sqrt{B}\right). \tag{B.57b}$$

The result (B.57) can be inserted into (B.47b) and (B.48) which completely defines $\bar{A}_n$ in (B.43) and (III.11a), and the resummation is thus complete.

## B.6 Matched asymptotic solution for interface at the cylinder wall

In this section, we re-visit the first and the second order matched asymptotic solutions implemented by [12] and convert their notation to ours. In doing so, we correct two typos in Eqns 3.18 and 3.21 of Lo's paper [12], shown respectively with wavy underlines in (B.59d) and (B.59e) below. Here we focus on Lo's predictions of the height of the meniscus along the cylinder to benchmark against the power series solution. Lo uses the superscripts (1) and (2) to represent the first and second order matched asymptotic approximations, respectively, and denotes the well-known Euler's constant as $\gamma = 0.5772$ (rounded to four decimal places). Lo defines the parameter $\epsilon = \frac{R}{l_c}$, where $R$ is the cylinder radius and $l_c = \sqrt{\frac{\sigma}{\rho g}}$ is the capillary length. In the notation used in our paper, this means that the Bond number and $\epsilon$ are related as $B = \epsilon^2$.

The lowest (first) order matched asymptotic solution for the height of the fluid along the wall, used in Figure 14, is

$$\bar{h}^{(1)}(\tilde{r} = 0) = \sin\phi \left\{ \ln \frac{4}{\epsilon(1+\cos\phi)} - \gamma \right\}, \tag{B.58a}$$

$$\phi = \frac{\pi}{2} - \theta. \tag{B.58b}$$

The second order matched solution (next order match) for the height of the interface along the cylindrical wall indicated in Figure 14 is

$$\bar{h}^{(2)}(\tilde{r} = 0) = \underbrace{z_1 \ln\epsilon + z_2}_{\bar{h}^{(1)} \text{ in } (B.58)} + z_3\epsilon^2 \ln^2\epsilon + z_4\epsilon^2 \ln\epsilon + z_5\epsilon^2. \tag{B.59a}$$

The constants used in (B.59a) are defined as

$$z_1 = -\sin\phi \;\;,\;\; z_2 = \sin\phi\,[\ln 4 - \ln(1+\cos\phi) - \gamma] \;\;,\;\; z_3 = \frac{1}{2}\sin\phi(1-\sin^2\phi), \tag{B.59b}$$

$$z_4 = \sin\phi \left\{ \cos^2\phi \left[ \gamma + \frac{1}{4} + \ln(\frac{1}{4}(1+\cos\phi)) + \right] + \frac{1}{4} - \cos\phi \right\}, \tag{B.59c}$$

$$
\begin{aligned}
z_5 = {} & \frac{1}{4}\sin\phi\cos\phi(\ln 4 - \gamma) - \frac{D}{\cos\phi} + \frac{1}{4}\sin\phi \\
& + D(1 - \ln 4 + \gamma) + \frac{1}{4}\sin^3\phi\left(\frac{1}{2} - \gamma^3 - \ln^2 2 + \gamma\ln 4 - \ln 2\right) \\
& + [\ln(1+\cos\phi)]\left[\frac{1}{4}\sin^3\phi\left(\ln 4 - \gamma + \frac{1}{\cos\phi}\right) + D - \frac{1}{4}\sin\phi\cos\phi\right] \\
& - \frac{1}{4}(\sin^3\phi)\ln^2(1+\cos\phi),
\end{aligned}
\tag{B.59d}
$$

where

$$
D = \frac{1}{4}\mathcal{C}(2-\mathcal{C}^2)\ln[1+\sqrt{1-\mathcal{C}^2}] - (1-\mathcal{C}^2)\frac{1}{2}\mathcal{C}(\ln 4 - \gamma) - \frac{1}{4}\mathcal{C}\sqrt{1-\mathcal{C}^2},
\tag{B.59e}
$$

and

$$
\mathcal{C} = \sin\phi.
\tag{B.59f}
$$

# C. Appendix: Non-Newtonian Sakiadis

## BOUNDARY LAYER PROBLEM

### C.1 Numerical Solution: Shooting method

The algorithm below is motivated from the work Cebeci et al. [53], developed for the Falkner-Skan boundary layer problem. Here, we extend their approach to the non-Newtonian Sakiadis problem given by (IV.27). With the goal of determining the value of $\kappa$ defined by (IV.3), we approximate the boundary value problem (IV.27) in $f(\eta)$ (defined on a semi-infinite domain) with the following initial value problem (IVP) in $f(\eta;\kappa)$ (defined on a finite domain):

$$\alpha(\alpha+1)f''' - (-f'')^{(2-\alpha)}f = 0, \;\; 0 \leq \eta \leq L \tag{C.1a}$$

with the initial conditions (taken from (IV.27b), (IV.27c), and (IV.3))

$$f(0;\kappa) = 0 \;\; , \;\; f'(0;\kappa) = 1 \;\; , \;\; f''(0;\kappa) = \kappa, \tag{C.1b}$$

where $f'$ denotes the derivative of $f$ with respect to $\eta$. In order to determine $\kappa$, we subject the IVP (C.1) to the constraint

$$f'(L;\kappa) = 0, \tag{C.2}$$

which incorporates condition (IV.27d) such that the solution to (C.1) limits to the solution of (IV.27) as $L \to \infty$. The determination of $\kappa$ and the numerical solution for $f$ itself from (C.1) (subject to (C.2)) is obtained by the method of shooting, as outlined below.

First, we replace (C.1a) with a system of three first-order ODEs. To do so, we let $\mathcal{U}(\eta;\kappa)$, $\mathcal{V}(\eta;\kappa)$, and $\mathcal{V}'(\eta;\kappa)$ represent $f'(\eta;\kappa)$, $f''(\eta;\kappa)$, and $f'''(\eta;\kappa)$, respectively. Thus, (C.1) can be written as the system

$$f' = \mathcal{U} \;\; , \;\; \mathcal{U}' = \mathcal{V} \;\; , \;\; \mathcal{V}' = \frac{(-\mathcal{V})^{(2-\alpha)}f}{\alpha(\alpha+1)}, \tag{C.3a}$$

with initial conditions

$$f(0;\kappa) = 0 \ , \ \mathcal{U}(0;\kappa) = 1 \ , \ \mathcal{V}(0;\kappa) = \kappa. \tag{C.3b}$$

The objective is to provide a solution to the IVP (C.3), such that the constraint (C.2) is satisfied. That is, we solve for the solution of (C.3) by seeking $\kappa$, such that

$$\mathcal{U}(L;\kappa) = 0, \tag{C.4}$$

where $L$ is successively increased, such that the $\kappa$ value for (C.1) approaches the $\kappa$ value for (IV.27).

In order to determine $\kappa$ in (C.3b), we use Newton's method [54] defined by

$$\kappa^{\gamma+1} = \kappa^{\gamma} - \frac{\mathcal{U}(L;\kappa^{\gamma})}{\frac{\partial}{\partial\kappa}(\mathcal{U}(L;\kappa^{\gamma}))} \ , \ \gamma = 0,\ 1,\ 2,\ ...,$$

with $\kappa^0$ being the initial estimate for $\kappa$, and $\gamma$ is the iteration number. In order to obtain the derivative of $\mathcal{U}$ with respect to $\kappa$, we take the derivative of (C.3) with respect to $\kappa$, which leads to the following additional IVP:

$$\frac{\partial f'}{\partial\kappa} = \frac{\partial\mathcal{U}}{\partial\kappa} \ , \ \frac{\partial\mathcal{U}'}{\partial\kappa} = \frac{\partial\mathcal{V}}{\partial\kappa} \ , \ \frac{\partial\mathcal{V}'}{\partial\kappa} = (\alpha-2)\frac{\partial\mathcal{V}}{\partial\kappa}\,\frac{(-\mathcal{V})^{(1-\alpha)}}{\alpha(\alpha+1)}f + \frac{(-\mathcal{V})^{(2-\alpha)}}{\alpha(\alpha+1)}\,\frac{\partial f}{\partial\kappa}, \tag{C.5a}$$

with conditions

$$\frac{\partial f}{\partial\kappa}(0;\kappa) = 0 \ , \ \frac{\partial\mathcal{U}}{\partial\kappa}(0;\kappa) = 0 \ , \ \frac{\partial\mathcal{V}}{\partial\kappa}(0;\kappa) = 1. \tag{C.5b}$$

For clarity, we assign new variables to the derivatives with respect to $\kappa$ as follows

$$\mathfrak{F}(\eta;\kappa) \equiv \frac{\partial f}{\partial\kappa}(\eta;\kappa), \ \ \mathfrak{U}(\eta;\kappa) \equiv \frac{\partial\mathcal{U}}{\partial\kappa}(\eta;\kappa), \ \ \mathfrak{V}(\eta;\kappa) \equiv \frac{\partial\mathcal{V}}{\partial\kappa}(\eta;\kappa),$$

commute the differentiation with respect to $\eta$ (denoted by primes) and differentiation with respect

to $\kappa$ in (C.5), and combine (C.3) and (C.5) into the single IVP evaluated at $\kappa = \kappa^\gamma$:

$$\frac{d}{d\eta}\begin{bmatrix} f \\ \mathcal{U} \\ \mathcal{V} \\ \mathfrak{F} \\ \mathfrak{U} \\ \mathfrak{V} \end{bmatrix} = \begin{bmatrix} \mathcal{U} \\ \mathcal{V} \\ \frac{(-\mathcal{V})^{(2-\alpha)} f}{\alpha(\alpha+1)} \\ \mathfrak{U} \\ \mathfrak{V} \\ (\alpha-2)\mathfrak{V}\frac{(-\mathcal{V})^{(1-\alpha)}}{\alpha(\alpha+1)} f + \frac{(-\mathcal{V})^{(2-\alpha)}}{\alpha(\alpha+1)}\mathfrak{F} \end{bmatrix}, \quad \begin{bmatrix} f \\ \mathcal{U} \\ \mathcal{V} \\ \mathfrak{F} \\ \mathfrak{U} \\ \mathfrak{V} \end{bmatrix}_{\eta=0} = \begin{bmatrix} 0 \\ 1 \\ \kappa^\gamma \\ 0 \\ 0 \\ 1 \end{bmatrix}. \tag{C.6}$$

From (C.6), both $\mathcal{U}(L;\kappa^\gamma)$ and $\mathfrak{U}(L;\kappa^\gamma)$ may be determined; then the guess $\kappa^\gamma$ may be progressed to the next iteration via

$$\kappa^{\gamma+1} = \kappa^\gamma - \frac{\mathcal{U}(L;\kappa^\gamma)}{\mathfrak{U}(L;\kappa^\gamma)} \quad , \quad \gamma = 0,\ 1,\ 2,\ ..., \tag{C.7}$$

to compute $\kappa^{\gamma+1}$. We use a fourth-order Runge-Kutta method, with $\Delta\eta = 0.001$ to solve (C.6). A convergence requirement of $|\kappa^{\gamma+1} - \kappa^\gamma| < 10^{-15}$ is enforced in the Newton iteration (C.7).

## C.2 Evaluations of $\kappa$, $C$, and $E$

### C.2.1 Numerical evaluation of $E$

In this section, we show that the constant $E \to 1$ as $\alpha \to 1$. These values are obtained numerically via a shooting method described in Appendix C.1 combined with the definition of $E$ defined in (IV.36).

**Table 2:** Numerical values of the constant $E$ defined in (IV.36). The values are computed using the shooting method algorithm explained in Appendix C.1 with $\eta = \infty$ replaced with a finite surrogate $L$ given in the table.

| $\alpha$ | $L$ | $E$ |
|---|---|---|
| 0.99 | 100 | 0.996357144778925 |
| 0.9 | 2000 | 0.921210805240775 |
| 0.8 | 11000 | 0.639133894794667 |
| 0.75 | 11000 | 0.249305949228073 |

### C.2.2 Evaluations of $\kappa$, $C$, and $E$ for $\alpha = 0.8$

In what follows, we provide constants used in the analytical solutions (IV.28), (IV.30), (IV.37), and (IV.39) for $\alpha = 0.8$. These are obtained in two ways–either numerically via a shooting method (Table 3 and Appendix C.1), or via a self-contained algorithm using the power series (Table 4 and Appendix (C.3)).

**Table 3:** Numerical values of the constants $\kappa$, $C$, and $E$ with $\alpha = 0.8$ for the non-Newtonian Sakiadis problem. The values are computed using the shooting method algorithm explained in Appendix C.1 with $\eta = \infty$ replaced with a finite surrogate $L$ given in the table. This numerical algorithm uses a Newton iteration with a tolerance of $10^{-15}$, wrapped around a $4^{\text{th}}$-order Runge-Kutta solver with a step size of $\triangle\eta = 0.001$.

| $L$ | $\kappa$ | $C$ | $E$ |
|---|---|---|---|
| 40 | -0.44069277587148 | 1.85680030949222 | 0.654388901675618 |
| 100 | -0.44067330624905 | 1.85989634054125 | 0.641907516688146 |
| 240 | -0.44067273476661 | 1.86013263767144 | 0.639639542413533 |
| 540 | -0.44067271669187 | 1.86015073982904 | 0.639235534657387 |
| 1000 | -0.44067271600486 | 1.86015225132246 | 0.639163575176951 |
| 2000 | -0.44067271594447 | 1.86015250138706 | 0.639141167249476 |
| 5000 | -0.44067271594052 | 1.86015253504567 | 0.639134860809690 |
| 11000 | -0.44067271594043 | 1.86015253716140 | 0.639133894794667 |

**Table 4:** Predicted values of the constants $\kappa$, $C$, and $E$ with $\alpha = 0.8$ for the non-Newtonian Sakiadis problem. The values are computed using the the solution of equations system (IV.38) explained in Section (IV.2.3.3) with the $N$ values given in the table. This algorithm uses a Newton iteration with a tolerance of $10^{-15}$.

| $N$ | $\kappa$ | $C$ | $E$ |
|---|---|---|---|
| 50 | -0.440672770686287 | 1.860151847487335 | 0.639137961392650 |
| 100 | -0.440672715934279 | 1.860152537361902 | 0.639133656731447 |
| 200 | -0.440672715934271 | 1.860152537362062 | 0.639133656729539 |
| 400 | -0.440672715934270 | 1.860152537362068 | 0.639133656729520 |

## C.3 Newton's method used to predict constants

The system of equations used in this algorithm are:

$$\mathcal{F}_1(\kappa, C, E) = \left[\sum_{n=0}^{N} \hat{A}_n(-1)^n\right] - C, \tag{C.8a}$$

$$\mathcal{F}_2(\kappa, C, E) = \left[\sum_{n=0}^{N} n\hat{A}_n(-1)^{n-1}\right] - A_1, \tag{C.8b}$$

$$\mathcal{F}_3(\kappa, C, E) = \hat{A}_N, \tag{C.8c}$$

where $C$, $A_1$, and $\hat{A}_N$ are defined in (IV.5), (IV.35e), and (IV.37g), respectively.

We take the derivatives of (C.8a)-(C.8c) with respect to $\kappa$, $C$, and $E$, and obtain the Jacobian matrix,

$$\mathbf{J} = \begin{bmatrix} \frac{\partial \mathcal{F}_1}{\partial C} & \frac{\partial \mathcal{F}_1}{\partial E} & \frac{\partial \mathcal{F}_1}{\partial \kappa} \\ \frac{\partial \mathcal{F}_2}{\partial C} & \frac{\partial \mathcal{F}_2}{\partial E} & \frac{\partial \mathcal{F}_2}{\partial \kappa} \\ \frac{\partial \mathcal{F}_3}{\partial C} & \frac{\partial \mathcal{F}_3}{\partial E} & \frac{\partial \mathcal{F}_3}{\partial \kappa} \end{bmatrix}, \tag{C.9}$$

which is used in Newton's Method

$$\begin{bmatrix} C^{j+1} \\ E^{j+1} \\ \kappa^{j+1} \end{bmatrix} = \begin{bmatrix} C^{j} \\ E^{j} \\ \kappa^{j} \end{bmatrix} - \mathbf{J}^{-1} \begin{bmatrix} \mathcal{F}_1(C^j, E^j, \kappa^j) \\ \mathcal{F}_2(C^j, E^j, \kappa^j) \\ \mathcal{F}_3(C^j, E^j, \kappa^j) \end{bmatrix}. \tag{C.10}$$

To construct the Jacobian matrix (C.9), we take the derivative of (C.8a - (C.8c), with respect to $C$, $E$, and $\kappa$, as follows:

$$\frac{\partial \mathcal{F}_1}{\partial C} = \left[\sum_{n=0}^{\infty} \frac{\partial \hat{A}_n}{\partial C}(-1)^n\right] - 1 \ , \ \frac{\partial \mathcal{F}_1}{\partial E} = \sum_{n=0}^{\infty} \frac{\partial \hat{A}_n}{\partial E}(-1)^n \ , \ \frac{\partial \mathcal{F}_1}{\partial \kappa} = \sum_{n=0}^{\infty} \frac{\partial \hat{A}_n}{\partial \kappa}(-1)^n, \tag{C.11a}$$

$$\frac{\partial \mathcal{F}_2}{\partial C} = \left[\sum_{n=0}^{\infty} n\frac{\partial \hat{A}_n}{\partial C}(-1)^{n-1}\right] - \frac{\partial A_1}{\partial C}, \tag{C.11b}$$

$$\frac{\partial \mathcal{F}_2}{\partial E} = \left[\sum_{n=0}^{\infty} n\frac{\partial \hat{A}_n}{\partial E}(-1)^{n-1}\right] - \frac{\partial A_1}{\partial E}, \tag{C.11c}$$

$$\frac{\partial \mathcal{F}_2}{\partial \kappa} = \left[\sum_{n=0}^{\infty} n\frac{\partial \hat{A}_n}{\partial \kappa}(-1)^{n-1}\right] - \frac{\partial A_1}{\partial \kappa}, \tag{C.11d}$$

$$\frac{\partial \mathcal{F}_3}{\partial C} = \frac{\partial \hat{A}_N}{\partial C} \ , \ \frac{\partial \mathcal{F}_3}{\partial E} = \frac{\partial \hat{A}_N}{\partial E} \ , \ \frac{\partial \mathcal{F}_3}{\partial \kappa} = \frac{\partial \hat{A}_N}{\partial \kappa}. \tag{C.11e}$$

We take the derivative of (IV.30c) with respect to the unknowns $C$, $E$, and $\kappa$. It is important to note that $\lambda$ is not function of any these three constants. Hence, we only take the derivative of $\mathcal{A}$ in (IV.30c) as follows:

$$\frac{\partial \mathcal{A}}{\partial C} = \frac{1-\alpha}{\alpha(\alpha+1)E} \ , \ \frac{\partial \mathcal{A}}{\partial E} = \frac{-C(1-\alpha)}{\alpha(\alpha+1)E^2} \ , \ \frac{\partial \mathcal{A}}{\partial \kappa} = 0. \tag{C.12}$$

We use the chain rule to take the derivatives of (IV.32b)-(IV.32f), as follows:

$$\frac{\partial k_1}{\partial C} = 3\alpha(\alpha+1)\lambda^3\mathcal{A}^2\frac{\partial \mathcal{A}}{\partial C} \ , \ \frac{\partial k_1}{\partial E} = 3\alpha(\alpha+1)\lambda^3\mathcal{A}^2\frac{\partial \mathcal{A}}{\partial E} \ , \ \frac{\partial k_1}{\partial \kappa} = 0, \tag{C.13a}$$

$$\frac{\partial k_2}{\partial C} = 9\alpha(\alpha+1)\lambda^2(\lambda-1)\mathcal{A}^2\frac{\partial \mathcal{A}}{\partial C} \ , \ \frac{\partial k_2}{\partial E} = 9\alpha(\alpha+1)\lambda^2(\lambda-1)\mathcal{A}^2\frac{\partial \mathcal{A}}{\partial E} \ , \ \frac{\partial k_2}{\partial \kappa} = 0, \tag{C.13b}$$

$$\frac{\partial k_3}{\partial C} = 3\alpha(\alpha+1)\lambda(\lambda-1)(\lambda-2)\mathcal{A}^2\frac{\partial \mathcal{A}}{\partial C}, \tag{C.13c}$$

$$\frac{\partial k_3}{\partial E} = 3\alpha(\alpha+1)\lambda(\lambda-1)(\lambda-2)\mathcal{A}^2\frac{\partial \mathcal{A}}{\partial E} \ , \ \frac{\partial k_3}{\partial \kappa} = 0, \tag{C.13d}$$

$$\frac{\partial k_4}{\partial C} = -2\lambda^2 \mathcal{A} \frac{\partial \mathcal{A}}{\partial C} \quad , \quad \frac{\partial k_4}{\partial E} = -2\lambda^2 \mathcal{A} \frac{\partial \mathcal{A}}{\partial E} \quad , \quad \frac{\partial k_4}{\partial \kappa} = 0, \tag{C.13e}$$

$$\frac{\partial k_5}{\partial C} = -2\lambda(\lambda-1) \mathcal{A} \frac{\partial \mathcal{A}}{\partial C} \quad , \quad \frac{\partial k_5}{\partial E} = -2\lambda(\lambda-1) \mathcal{A} \frac{\partial \mathcal{A}}{\partial E} \quad , \quad \frac{\partial k_5}{\partial \kappa} = 0. \tag{C.13f}$$

We take derivatives of $\hat{A}_0$ through $\hat{A}_4$ in (IV.37b)-(IV.37f), as follows

$$\frac{\partial \hat{A}_0}{\partial C} = 0 \quad , \quad \frac{\partial \hat{A}_0}{\partial E} = 0 \quad , \quad \frac{\partial \hat{A}_0}{\partial \kappa} = 0. \tag{C.14a}$$

$$\frac{\partial \hat{A}_1}{\partial C} = \frac{-1}{\lambda \mathcal{A}^2} \frac{\partial \mathcal{A}}{\partial C} \quad , \quad \frac{\partial \hat{A}_1}{\partial E} = \frac{-1}{\lambda \mathcal{A}^2} \frac{\partial \mathcal{A}}{\partial E} \quad , \quad \frac{\partial \hat{A}_1}{\partial \kappa} = 0, \tag{C.14b}$$

$$\frac{\partial \hat{A}_2}{\partial C} = \frac{1}{2\lambda^2} \left( \frac{-2\kappa}{a^3} + \frac{\lambda - 1}{\mathcal{A}^2} \right) \frac{\partial \mathcal{A}}{\partial C}, \tag{C.14c}$$

$$\frac{\partial \hat{A}_2}{\partial E} = \frac{1}{2\lambda^2} \left( \frac{-2\kappa}{a^3} + \frac{\lambda - 1}{\mathcal{A}^2} \right) \frac{\partial \mathcal{A}}{\partial E} \quad , \quad \frac{\partial \hat{A}_2}{\partial \kappa} = \frac{1}{2\lambda^2 \mathcal{A}^2}. \tag{C.14d}$$

$$\frac{\partial \hat{A}_3}{\partial C} = u_1 \frac{\partial v_1}{\partial C} + v_1 \frac{\partial u_1}{\partial C} \quad , \quad \frac{\partial \hat{A}_3}{\partial E} = u_1 \frac{\partial v_1}{\partial E} + v_1 \frac{\partial u_1}{\partial E} \quad , \quad \frac{\partial \hat{A}_3}{\partial \kappa} = u_1 \frac{\partial v_1}{\partial \kappa}, \tag{C.14e}$$

where

$$u_1 = \frac{1}{6k_1} \quad , \quad v_1 = -2k_2 \hat{A}_2 - k_3 \hat{A}_1, \tag{C.14f}$$

$$\frac{\partial u_1}{\partial C} = \frac{-1}{6(k_1)^2} \frac{\partial k_1}{\partial C} \quad , \quad \frac{\partial u_1}{\partial E} = \frac{-1}{6(k_1)^2} \frac{\partial k_1}{\partial E} \quad , \quad \frac{\partial u_1}{\partial \kappa} = 0, \tag{C.14g}$$

$$\frac{\partial v_1}{\partial C} = -2 \left( k_2 \frac{\partial \hat{A}_2}{\partial C} + \hat{A}_2 \frac{\partial k_2}{\partial C} \right) - \left( k_3 \frac{\partial \hat{A}_1}{\partial C} + \hat{A}_1 \frac{\partial k_3}{\partial C} \right), \tag{C.14h}$$

$$\frac{\partial v_1}{\partial E} = -2 \left( k_2 \frac{\partial \hat{A}_2}{\partial E} + \hat{A}_2 \frac{\partial k_2}{\partial E} \right) - \left( k_3 \frac{\partial \hat{A}_1}{\partial E} + \hat{A}_1 \frac{\partial k_3}{\partial E} \right), \tag{C.14i}$$

$$\frac{\partial v_1}{\partial \kappa} = -2k_2 \frac{\partial \hat{A}_2}{\partial \kappa}. \tag{C.14j}$$

$$\frac{\partial \hat{A}_4}{\partial C} = u_2 \frac{\partial v_2}{\partial C} + v_2 \frac{\partial u_2}{\partial C} \quad , \quad \frac{\partial \hat{A}_4}{\partial E} = u_2 \frac{\partial v_2}{\partial E} + v_2 \frac{\partial u_2}{\partial E} \quad , \quad \frac{\partial \hat{A}_4}{\partial \kappa} = u_2 \frac{\partial v_2}{\partial \kappa}, \tag{C.14k}$$

and

$$u_2 = \frac{1}{24k_1} \quad , \quad v_2 = -2k_2 \hat{A}_2 - 6k_2 \hat{A}_3 - 2k_3 \hat{A}_2 + \hat{A}_1 \hat{d}_0 - 12k_1 \hat{A}_3, \tag{C.14l}$$

$$\frac{\partial u_2}{\partial C} = \frac{-1}{24(k_1)^2} \frac{\partial k_1}{\partial C} \quad , \quad \frac{\partial u_2}{\partial E} = \frac{-1}{24(k_1)^2} \frac{\partial k_1}{\partial E} \quad , \quad \frac{\partial u_2}{\partial \kappa} = 0, \tag{C.14m}$$

$$\frac{\partial v_2}{\partial C} = -2 \left( k_2 \frac{\partial \hat{A}_2}{\partial C} + \hat{A}_2 \frac{\partial k_2}{\partial C} \right) - 6 \left( k_2 \frac{\partial \hat{A}_3}{\partial C} + \hat{A}_3 \frac{\partial k_2}{\partial C} \right) - 2 \left( k_3 \frac{\partial \hat{A}_2}{\partial C} + \hat{A}_2 \frac{\partial k_3}{\partial C} \right) + \hat{A}_1 \frac{\partial \hat{d}_0}{\partial C} + \hat{d}_0 \frac{\partial \hat{A}_1}{\partial C} - 12 \left( k_1 \frac{\partial \hat{A}_3}{\partial C} + \hat{A}_3 \frac{\partial k_1}{\partial C} \right), \tag{C.14n}$$

$$\frac{\partial v_2}{\partial E} = -2\left(k_2\frac{\partial \hat{A}_2}{\partial E} + \hat{A}_2\frac{\partial k_2}{\partial E}\right) - 6\left(k_2\frac{\partial \hat{A}_3}{\partial E} + \hat{A}_3\frac{\partial k_2}{\partial E}\right) - 2\left(k_3\frac{\partial \hat{A}_2}{\partial E} + \hat{A}_2\frac{\partial k_3}{\partial E}\right) + \hat{A}_1\frac{\partial \hat{d}_0}{\partial E} + \hat{d}_0\frac{\partial \hat{A}_1}{\partial E} - 12\left(k_1\frac{\partial \hat{A}_3}{\partial E} + \hat{A}_3\frac{\partial k_1}{\partial E}\right), \quad \text{(C.14o)}$$

$$\frac{\partial v_2}{\partial \kappa} = -2k_2\frac{\partial \hat{A}_2}{\partial \kappa} - 6k_2\frac{\partial \hat{A}_3}{\partial \kappa} - 2k_3\frac{\partial \hat{A}_2}{\partial \kappa} + \hat{A}_1\frac{\partial \hat{d}_0}{\partial \kappa} - 12k_1\frac{\partial \hat{A}_3}{\partial \kappa}, \quad \text{(C.14p)}$$

$$\frac{\partial \hat{d}_0}{\partial C} = (2-\alpha)(\hat{c}_0)^{1-\alpha}\frac{\partial \hat{c}_0}{\partial C}, \quad \text{(C.14q)}$$

$$\frac{\partial \hat{d}_0}{\partial E} = (2-\alpha)(\hat{c}_0)^{1-\alpha}\frac{\partial \hat{c}_0}{\partial E} \quad , \quad \frac{\partial \hat{d}_0}{\partial \kappa} = (2-\alpha)(\hat{c}_0)^{1-\alpha}\frac{\partial \hat{c}_0}{\partial \kappa}, \quad \text{(C.14r)}$$

$$\frac{\partial \hat{c}_0}{\partial C} = 2\left(k_4\frac{\partial \hat{A}_2}{\partial C} + \hat{A}_2\frac{\partial k_4}{\partial C}\right) + k_5\frac{\partial \hat{A}_1}{\partial C} + \hat{A}_1\frac{\partial k_5}{\partial C}, \quad \text{(C.14s)}$$

$$\frac{\partial \hat{c}_0}{\partial E} = 2\left(k_4\frac{\partial \hat{A}_2}{\partial E} + \hat{A}_2\frac{\partial k_4}{\partial E}\right) + k_5\frac{\partial \hat{A}_1}{\partial E} + \hat{A}_1\frac{\partial k_5}{\partial E} \quad , \quad \frac{\partial \hat{c}_0}{\partial \kappa} = 2k_4\frac{\partial \hat{A}_2}{\partial \kappa}. \quad \text{(C.14t)}$$

Next, we take derivative of (IV.37g) as follows

$$\frac{\partial \hat{A}_{n+3}}{\partial C} = \frac{v_3\frac{\partial u_3}{\partial C} - u_3\frac{\partial v_3}{\partial C}}{(v_3)^2} \quad , \quad \frac{\partial \hat{A}_{n+3}}{\partial E} = \frac{v_3\frac{\partial u_3}{\partial E} - u_3\frac{\partial v_3}{\partial E}}{(v_3)^2} \quad , \quad \frac{\partial \hat{A}_{n+3}}{\partial \kappa} = \frac{\frac{\partial u_3}{\partial \kappa}}{v_3}, \quad \text{(C.15a)}$$

where

$$u_3 = \{-k_2(n+1)n - k_3(n+1) - k_1(n+1)n(n-1)\}\,\hat{A}_{n+1} + \{-k_2(n+2)(n+1) - 2k_1(n+2)(n+1)n\}\,\hat{A}_{n+2} + \hat{e}_n, \quad \text{(C.15b)}$$

$$v_3 = k_1(n+3)(n+2)(n+1), \quad \text{(C.15c)}$$

$$\frac{\partial u_3}{\partial C} = \{-k_2(n+1)n - k_3(n+1) - k_1(n+1)n(n-1)\}\,\frac{\partial \hat{A}_{n+1}}{\partial C} + \hat{A}_{n+1}\left\{-\frac{\partial k_2}{\partial C}(n+1)n - \frac{\partial k_3}{\partial C}(n+1) - \frac{\partial k_1}{\partial C}(n+1)n(n-1)\right\} + \{-k_2(n+2)(n+1) - 2k_1(n+2)(n+1)n\}\,\frac{\partial \hat{A}_{n+2}}{\partial C} + \hat{A}_{n+2}\left\{-\frac{\partial k_2}{\partial C}(n+2)(n+1) - 2\frac{\partial k_1}{\partial C}(n+2)(n+1)n\right\} + \frac{\partial \hat{e}_n}{\partial C}, \quad \text{(C.15d)}$$

$$\frac{\partial u_3}{\partial E} = \{-k_2(n+1)n - k_3(n+1) - k_1(n+1)n(n-1)\}\frac{\partial \hat{A}_{n+1}}{\partial E} + \hat{A}_{n+1}\left\{-\frac{\partial k_2}{\partial E}(n+1)n - \frac{\partial k_3}{\partial E}(n+1) - \frac{\partial k_1}{\partial E}(n+1)n(n-1)\right\} + \{-k_2(n+2)(n+1) - 2k_1(n+2)(n+1)n\}\frac{\partial \hat{A}_{n+2}}{\partial E} + \hat{A}_{n+2}\left\{-\frac{\partial k_2}{\partial E}(n+2)(n+1) - 2\frac{\partial k_1}{\partial E}(n+2)(n+1)n\right\} + \frac{\partial \hat{e}_n}{\partial E}, \quad \text{(C.15e)}$$

$$\frac{\partial u_3}{\partial \kappa} = \{-k_2(n+1)n - k_3(n+1) - k_1(n+1)n(n-1)\}\frac{\partial \hat{A}_{n+1}}{\partial \kappa} + \{-k_2(n+2)(n+1) - 2k_1(n+2)(n+1)n\}\frac{\partial \hat{A}_{n+2}}{\partial \kappa} + \frac{\partial \hat{e}_n}{\partial \kappa}, \quad \text{(C.15f)}$$

$$\frac{\partial v_3}{\partial C} = (n+3)(n+2)(n+1)\frac{\partial k_1}{\partial C} \;\;,\;\; \frac{\partial v_3}{\partial E} = (n+3)(n+2)(n+1)\frac{\partial k_1}{\partial E} \;\;,\;\; \frac{\partial v_3}{\partial \kappa} = 0, \quad \text{(C.15g)}$$

$$\frac{\partial \hat{e}_n}{\partial C} = \sum_{j=0}^{n} \hat{A}_j \frac{\partial \hat{d}_{n-j}}{\partial C} + \hat{d}_{n-j}\frac{\partial \hat{A}_j}{\partial C}, \quad \text{(C.15h)}$$

$$\frac{\partial \hat{e}_n}{\partial E} = \sum_{j=0}^{n} \hat{A}_j \frac{\partial \hat{d}_{n-j}}{\partial E} + \hat{d}_{n-j}\frac{\partial \hat{A}_j}{\partial E}, \quad \text{(C.15i)}$$

$$\frac{\partial \hat{e}_n}{\partial \kappa} = \sum_{j=0}^{n} \hat{A}_j \frac{\partial \hat{d}_{n-j}}{\partial \kappa} + \hat{d}_{n-j}\frac{\partial \hat{A}_j}{\partial \kappa}, \quad \text{(C.15j)}$$

$$\frac{\partial \hat{d}_{n>0}}{\partial C} = \frac{-1}{n(\hat{c}_0)^2}\frac{\partial \hat{c}_0}{\partial C}\sum_{j=1}^{n}(3j-\alpha j-n)\hat{c}_j\hat{d}_{n-j} + \frac{1}{n\hat{c}_0}\sum_{j=1}^{n}(3j-\alpha j-n)\frac{\partial \hat{c}_j}{\partial C}\hat{d}_{n-j} + \frac{1}{n\hat{c}_0}\sum_{j=1}^{n}(3j-\alpha j-n)\hat{c}_j\frac{\partial \hat{d}_{n-j}}{\partial C}, \quad \text{(C.15k)}$$

$$\frac{\partial \hat{d}_{n>0}}{\partial E} = \frac{-1}{n(\hat{c}_0)^2}\frac{\partial \hat{c}_0}{\partial E}\sum_{j=1}^{n}(3j-\alpha j-n)\hat{c}_j\hat{d}_{n-j} + \frac{1}{n\hat{c}_0}\sum_{j=1}^{n}(3j-\alpha j-n)\frac{\partial \hat{c}_j}{\partial E}\hat{d}_{n-j} + \frac{1}{n\hat{c}_0}\sum_{j=1}^{n}(3j-\alpha j-n)\hat{c}_j\frac{\partial \hat{d}_{n-j}}{\partial E}, \quad \text{(C.15l)}$$

$$\frac{\partial \hat{d}_{n>0}}{\partial \kappa} = \frac{-1}{n(\hat{c}_0)^2}\frac{\partial \hat{c}_0}{\partial \kappa}\sum_{j=1}^{n}(3j-\alpha j-n)\hat{c}_j\hat{d}_{n-j} + \frac{1}{n\hat{c}_0}\sum_{j=1}^{n}(3j-\alpha j-n)\frac{\partial \hat{c}_j}{\partial \kappa}\hat{d}_{n-j} + \frac{1}{n\hat{c}_0}\sum_{j=1}^{n}(3j-\alpha j-n)\hat{c}_j\frac{\partial \hat{d}_{n-j}}{\partial \kappa}, \quad \text{(C.15m)}$$

$$\frac{\partial \hat{c}_{n>0}}{\partial C} = (k_4 n + k_5)(n+1)\frac{\partial \hat{A}_{n+1}}{\partial C} + \left(\frac{\partial k_4}{\partial C} n + \frac{\partial k_5}{\partial C}\right)(n+1)\hat{A}_{n+1} + k_4(n+2)(n+1)\frac{\partial \hat{A}_{n+2}}{\partial C} + \frac{\partial k_4}{\partial C}(n+2)(n+1)\hat{A}_{n+2}, \quad \text{(C.15n)}$$

$$\frac{\partial \hat{c}_{n>0}}{\partial E} = (k_4 n + k_5)(n+1)\frac{\partial \hat{A}_{n+1}}{\partial E} + \left(\frac{\partial k_4}{\partial E} n + \frac{\partial k_5}{\partial E}\right)(n+1)\hat{A}_{n+1} + k_4(n+2)(n+1)\frac{\partial \hat{A}_{n+2}}{\partial E} + \frac{\partial k_4}{\partial E}(n+2)(n+1)\hat{A}_{n+2}, \quad \text{(C.15o)}$$

$$\frac{\partial \hat{c}_{n>0}}{\partial \kappa} = (k_4 n + k_5)(n+1)\frac{\partial \hat{A}_{n+1}}{\partial \kappa} + \left(\frac{\partial k_4}{\partial \kappa} n + \frac{\partial k_5}{\partial \kappa}\right)(n+1)\hat{A}_{n+1} + k_4(n+2)(n+1)\frac{\partial \hat{A}_{n+2}}{\partial \kappa} + \frac{\partial k_4}{\partial \kappa}(n+2)(n+1)\hat{A}_{n+2}. \quad \text{(C.15p)}$$

Finally, we take derivative of (IV.35e) as follows

$$\frac{\partial A_1}{\partial C} = \frac{1}{1-\alpha}\left(\frac{u_4}{v_4}\right)^{\frac{\alpha}{1-\alpha}}\left(\frac{v_4 \frac{\partial u_4}{\partial C} - u_4 \frac{\partial v_4}{\partial C}}{(v_4)^2}\right), \quad \text{(C.16a)}$$

$$\frac{\partial A_1}{\partial E} = \frac{1}{1-\alpha}\left(\frac{u_4}{v_4}\right)^{\frac{\alpha}{1-\alpha}}\left(\frac{v_4 \frac{\partial u_4}{\partial E} - u_4 \frac{\partial v_4}{\partial E}}{(v_4)^2}\right) \quad , \quad \frac{\partial A_1}{\partial \kappa} = 0, \quad \text{(C.16b)}$$

where

$$u_5 = k_3 \quad , \quad v_5 = A_0 (k_5)^{2-\alpha}, \quad \text{(C.16c)}$$

$$\frac{\partial u_5}{\partial C} = \frac{\partial k_3}{\partial C} \quad , \quad \frac{\partial u_5}{\partial E} = \frac{\partial k_3}{\partial E} \quad , \quad \frac{\partial u_5}{\partial \kappa} = 0, \quad \text{(C.16d)}$$

$$\frac{\partial v_5}{\partial C} = A_0(2-\alpha)(k_5)^{1-\alpha}\frac{\partial k_5}{\partial C} + (k_5)^{2-\alpha} \quad , \quad \frac{\partial v_5}{\partial E} = A_0(2-\alpha)(k_5)^{1-\alpha}\frac{\partial k_5}{\partial E} \quad , \quad \frac{\partial v_5}{\partial \kappa} = 0. \quad \text{(C.16e)}$$

# References

[1] N. S. Barlow, C. R. Stanton, N Hill, S. J. Weinstein, and A. G. Cio. On the summation of divergent, truncated, and underspecified power series via asymptotic approximants. *Q. J. Mech. Appl. Math.*, 70(1):21–48, 2017.

[2] N. S. Barlow, S. J. Weinstein, and J. A. Faber. An asymptotically consistent approximant for the equatorial bending angle of light due to kerr black holes. *Class. Quant. Grav.*, 34(135017):1–16, 2017.

[3] R. J. Beachley, M. Mistysyn, J. A. Faber, S. J. Weinstein, and N. S. Barlow. Accurate closed-form trajectories of light around a kerr black hole using asymptotic approximants. *Class. Quant. Grav.*, 35(20):1–28, 2018.

[4] E. R Belden, Z. A. Dickman, S. J. Weinstein, A. D. Archibee, E. Burroughs, and N. S. Barlow. Asymptotic approximant for the Falkner-Skan boundary layer equation. *Q. J. Mech. Appl. Math.*, 73(1):36–50, 2020.

[5] N. S. Barlow and S. J. Weinstein. Accurate closed-form solution of the SIR epidemic model. *Physica D*, 408:132540:1–4, 2020.

[6] S. J. Weinstein, M. S. Holland, K. E. Rogers, and N. S. Barlow. Analytic solution of the SEIR epidemic model via asymptotic approximant. *Physica D*, 411:132633:1–6, 2020.

[7] E. Ramé, S. J. Weinstein, and N. S. Barlow. Free surface shapes in rigid body rotation: Exact solutions, asymptotics and approximants. *IMA J. Appl. Math.*, doi:10.1093/imamat/hxab038, 2021.

[8] P. M. Morse and H. Feshbach. *Methods of Theoretical Physics: Part I*. Mc-Graw Hill, 1953.

[9] G. K. Batchelor. *An Introduction to Fluid Dynamics*, chapter 1: The physical properties of fluids. Cambridge: Cambridge Univerisity Press, 1967.

[10] R. F. Probstein. *Physicochemical Hydrodynamics*, chapter 10.3: Coating Flows. Wiley, 2 edition, 2003.

[11] N. Naghshineh, W. C. Reinberger, N. S. Barlow, M. A. Samaha, and S. J. Weinstein. On the use of asymptotically motivated gauge functions to obtain convergent series solutions to nonlinear ODEs. *IMA Journal of Applied Mathematics*, 88(1):43–66, 02 2023.

[12] L. L. Lo. The meniscus on a needle - a lesson in matching. *J. Fluid Mech.*, 132:65–78, 1983.

[13] N. Naghshineh, W. C. Reinberger, N. S. Barlow, M. A. Samaha, and S. J. Weinstein. The shape of an axisymmetric meniscus in a static liquid pool: effective implementation of the euler transformation. https://doi.org/10.1093/imamat/hxad037, 2024.

[14] S. J. Weinstein and K. J. Ruschak. Coating flows. *Ann. Rev. Fluid Mech.*, 36:29–53, 2004.

[15] T. D. Blake, A. Clarke, and K. J. Ruschak. Hydrodynamic assist of dynamic wetting. *AIChE J.*, 40(2):229–242, 1994.

[16] N. Naghshineh, N. S. Barlow, M. A. Samaha, and S. J. Weinstein. Asymptotically consistent analytical solutions for the non-Newtonian Sakiadis boundary layer. *Physics of Fluids*, 35(053103):1–15, 2023.

[17] R. V. Churchill. *Complex Variables*, chapter VI: Power series. McGraw-Hill: New York, 1948.

[18] P. Henrici. Automatic computations with power series. *JACM*, 3:10–15, 1956.

[19] C. Domb and M. F. Sykes. On the susceptibility of a ferromagnetic above the curie point. *Proc. Roy. Soc. London A*, 240(1221):214–228, 1957.

[20] C. M. Bender and S. A. Orszag. *Advanced Mathematical Methods for Scientists and Engineers I: Asymptotic Methods and Perturbation Theory*. McGraw-Hill, 1978.

[21] A. Ferguson. On the shape of the capillary surface formed by the external contact of a liquid with a cylinder of large radius. *Philosophical Magazine and Journal of Science*, 24(6):837–844, 1912.

[22] D. D. White and J. A. Tallmadge. Static menisci on the outside of cylinders. *J. Fluid Mech.*, 23:325–335, 1965.

[23] C. Huh and L. E. Scriven. Shapes of axisymmetric fluid interfaces of unbounded extent. *J. of Colloid and Interface Science*, 30:323–337, 1968.

[24] D. F. James. The meniscus on the outside of a small circular cylinder. *J. Fluid Mech.*, 63:657–664, 1973.

[25] M. Van Dyke. *Perturbation Methods in Fluid Mechanics*. Parabolic, 1975.

[26] L. Binetti, I. Del Villar, K. P. Dissanayake, A. Stankiewicz, T. Sun, K. T. V. Grattan, and L. S. M. Alwis. Monitoring of the critical meniscus of very low liquid volumes using an optical fiber sensor. *IEEE Sensors Journal*, 20(20), 2020.

[27] Y. Tang and S. Cheng. The meniscus on the outside of a circular cylinder: From microscopic to macroscopic scales. *Journal of Colloid and Interface Science*, 533:401–408, 2019.

[28] R. E. Scraton. The practical use of the euler transformation. *BIT Numerical Mathematics*, 29:356–360, 1989.

[29] J. P. Boyd. The Blasius function in the complex plane. *Exper. Math.*, 8(4):381–394, 1999.

[30] T. A. Driscoll, N. Hale, and L. N. Trefethen, editors. *Chebfun Guide*. Pafnuty Publications, Oxford, 2014.

[31] E. J. Hinch. *Perturbation Methods*, chapter 8: Improved Convergence. Cambridge: Cambridge University Press, 1991.

[32] G. H. Hardy. *Divergent Series*. Oxford: Oxford University Press, 1949.

[33] R. Parnes. Complex zeros of the modified bessel function $k_n(z)$. *Mathematics of Computation*, 26(120):949–953, 1972.

[34] B. C. Sakiadis. Boundary-layer behavior on continuous solid surfaces: II the boundary layer on a continuous flat surface. *AlChE J.*, 7:221–225, 1961.

[35] N. Vishnu Ganesh, Qasem M. Al-Mdallal, K. Reena, and Sidra Aman. Blasius and sakiadis slip flow of $h_2o - c_2h_6o_2$ (50:50) based nanoliquid with different geometry of boehmite alumina nanoparticles. *Case Studies in Thermal Engineering*, 16, 2019.

[36] I. Azhar and A. Tasawar. A study on heat transfer enhancement of copper ($cu$)-ethylene glycol based nanoparticle on radial stretching sheet. *Alexandria Engineering Journal*, 71:13–20, 2023.

[37] A. Abbas, I. Ijaz, M. Ashraf, and H. Ahmad. Combined effects of variable density and thermal radiation on mhd sakiadis flow. *Case Studies in Thermal Engineering*, 28, 2021.

[38] W. K. Usafzai. Multiple exact solutions of second degree nanofluid slip flow and heat transport in porous medium. *Thermal Science and Engineering Progress*, 40, 2023.

[39] P. Mishra, D. Kumar, Y. D. Reddy, and B. S. Goud. Mhd williamson micropolar fluid flow pasting a non-linearly stretching sheet under the presence of non linear heat generation/ absorption. *Journal of the Indian Chemical Society*, 100(1), 2023.

[40] W. K. Usafzai and E. H. Aly. Multiple exact solutions for micropolar slip flow and heat transfer of a bidirectional moving plate. *Thermal Science and Engineering Progress*, 37, 2023.

[41] M. Khazayinejad and S. S. Nourazar. On the effect of spatial fractional heat conduction in mhd boundary layer flow using $gr - fe_3o_4 - h_2o$ hybrid nanofluid. *International Journal of Thermal Sciences*, 172, 2022.

[42] H. Blasius. Grenzschichten in flussigkeiten mit kleiner reibung. *Zeitschrift fur Mathematik und Physik*, 56:1–37, 1908.

[43] C. R. Bataller. Numerical comparisons of Blasius and Sakiadis flows. *MATEMATIKA*, 26(2):187–196, 2010.

[44] R. Fazio. The iterative transformation method for the Sakiadis problem. *Comp. Fluids*, 106:196–200, 2015.

[45] L. R. Turner. Inverse of the Vandermonde matrix with applications. Technical Note D-3547, NASA, 1966.

[46] G. N. Watson. *Complex Integration and Cauchy's Theorem*, chapter VII: Expansions in series. Cambridge University Press, 1914.

[47] S. A. Eftekhari and A. A. Jafari. Numerical solution of general boundary layer problems by the method of differential quadrature. *Scientia Iranica*, 20(4):1278–1301, 2013.

[48] V. G. Fox, T. L. E. Erickson, and L. T Fan. The laminar boundary layer on a moving continuous flat sheet immersed in a non-newtonian fluid. *AlChE Journal*, 15:327–333, 1969.

[49] I. Pop and R. S. R. G Gorla. Second-order boundary layer solution for a continuous moving surface in a non-newtonian fluid. *Int. J. Engng Sci.*, 4:313–322, 1990.

[50] G. A. Baker and P. Graves-Morris. *Padé Approximants*. Cambridge, 1996.

[51] E. R. Belden, Z. A. Dickman, S. J. Weinstein, A. D. Archibee, E. Burroughs, and N. S. Barlow. Asymptotic approximant for the falkner-skan boundary-layer equation. *Q. J. Mech. Appl. Math*, 73(1):36–50, 2020.

[52] I. S. Gradshteyn and I. M. Ryzhik. *Table of integrals, series, and products: seventh edition*. Academic Press, 2007.

[53] T. Cebeci and H. B. Keller. Shooting and parallel shooting methods for solving the Falkner-Skan boundary-layer equation. *J. Comp. Phys.*, 7:289–300, 1971.

[54] E. Isaacson and H. B. Keller. *Analysis of Numerical Methods*. John Wiley and Sons, New York, 1966.